MARTIN-LUTHER UNIVERSITÄT
HALLE-WITTENBERG

MASTER THESIS

CHARACTERIZATION OF 3D PRINTED PARTS FROM FIBER REINFORCED POLYAMIDE VIA FUSED FILAMENT FABRICATION PROCESS.

Aminur Rahman

Master's in Polymer Material Science
Faculty- Natural Science II

Fraunhofer
IMWS

Declaration

I hereby declare that I am the sole author of this Master's thesis "characterization of 3D printed parts from fiber-reinforced polyamide via fused filament fabrication process" and that I have not used any sources other than those listed in the references. I further declare that I have not submitted this thesis at any other institution in order to obtain a degree.

I am also aware that, unless agreed otherwise, this Master's thesis produced under supervision represents a group achievement and forms part of the overall research of the supervising institution. As a result, none of the co-authors (e.g. authors of the text, creative project staff, co-supervisors) may use passages from the thesis for commercial purposes or make them accessible to third parties without the (written) approval of all those involved due to reasons of copyright. Particular note must be taken of the Arbeitnehmererfindergesetz (German Employee Invention Act), according to which pre-publication of patent-related content is prohibited.

Halle, _____ _____

Aminur Rahman

Acknowledgment

I would like to express my gratuity to Dr. Ralf Schlimper for providing the opportunity to perform my Master thesis at Fraunhofer IMWS, Halle (Saale), Germany. A great thanks to my supervisor Dr. Ralf Schäuble for his utmost guidance, support and feedback throughout the entire period.

I am grateful to Friedrich Zerling in order to support and helping in experimental analysis and setup during this research project. I am also thankful to Nishanth Shenoy Kasargod Pattanshetty for helping me with the analysis of computed tomography scanning results. A special thanks to Nico Teuscher for guiding me to operate optical microscopy, André Henkel for computed tomography scans, and Ralf Schlegel for helping tensile test setup.

Moreover, I would also like to express gratuity to my internal supervisor Professor Dr. Peter Michel for being my mentor and his priceless advice.

Last but not least, I would like to thank my parents and friends for the inspiration and continuous mental support throughout the journey of my entire Master's study as well as the thesis work.

Abstract

Fused filament fabrication (FFF) is one of the most common methods of additive manufacturing or three-dimensional printing. The mechanical performance of this technique mostly relies on the bonding strength between the layers and micro defects play a vital role in the reduction of performance. X-ray computed tomography (XCT) and optical microscopy are good ways to investigate such micro defects. To observe the influence on the mechanical performance, in this study, the test specimens are manufactured using continuous filament of polyamide 6 and short glass fiber by varying process parameters likewise raster angles, fiber weight fraction, printing temperature, printing speed and heating strategies. The correlation of features such as porosity and fiber orientation respectively suggests having higher porosity towards 90^{o} raster angle and higher fiber orientation towards 0^{o} raster angle. The qualitative analysis such as tensile strength and elastic modulus indicates having better mechanical performance towards 0^{o} raster angle. It is also noticeable that heating strategies help to improve the bonding strength between the printed layers. The increased amount of fiber weight fraction contributes to increasing microvoids, strength, and stiffness inside the material and the specimen cut out from greater distance from the printing bed indicates to possess better tensile strength.

Table of Contents

List of Figures

List of Tables

CHAPTER 1

INTRODUCTION

1.1 Fiber Reinforced Composite

Composites are special kinds of engineering materials used for high-performance applications and can be defined as the assembly of two or more chemically different elements different on a macroscopic level [1] [2], with the combination of having improved qualities. The reinforcement part, especially fibers, bring about significant improvements in mechanical behavior to host with added benefits. A simple concept of composites is shown in *figure 1*.

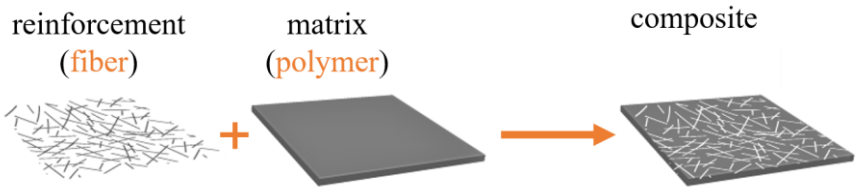

Fig 1. Schematic of the fiber-reinforced composite [3].

There are several benchmarks that can be considered to classify composite materials. According to the combination, composites can be divided into three main categories [2], such as particle reinforced composites, fiber-reinforced composites, and structural composites.

The present work highlights mainly on fiber-reinforced composites, which can be further divided into two types such as continuous fiber-reinforced and discontinuous fiber-reinforced. A brief classification of composites is shown in *figure 2*.

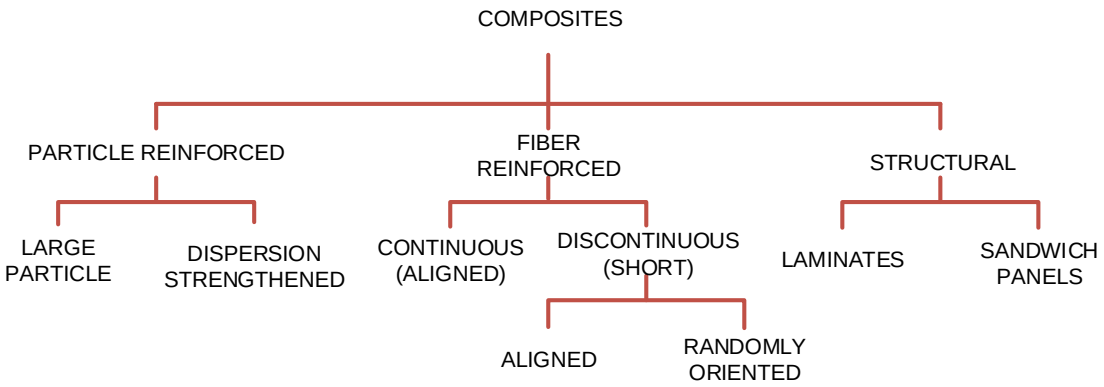

Fig 2. Classification of composites according to combination [2].

1.2 Fused Filament Fabrication

Fused filament fabrication (FFF) is a popular method of additive manufacturing. Thermoplastic materials are supplied in the melting chamber attached with a nozzle. The print head with a nozzle can move in three dimensional positions according to the directions given by the user in computer aided (CAD) software. With temperature application, polymeric material melts and is extruded through the nozzle and deposited on the base plate in layer-by-layer manners, *figure 4*.

Three dimensional printing systems are much more customizable, lots of variations are possible with the printer setup. And fused filament fabrication can be either *in situ fusion* or *extrusion of pre-impregnated fiber* [4] types. *In-situ fusion* is flexible and has wide variations. Both the polymer and filament are supplied differently from different suppliers, in *figure 3*. The biggest advantage is the customizable control over the fiber volume fraction, although printed parts have poor bonding at the fiber matrix interface [5]. In *extrusion of pre-impregnated fiber* technique, it is not possible to customize the printing setup so widely [4] like in-situ. Fibers are already impregnated inside of the polymer.

According to the application and the production cost different polymers and reinforcement can be commonly used in fused filament fabrication printing processes, such as ABS, Polyamide, Polypropylene, Polylactic-acid (PLA), etc. as matrix and glass fiber, carbon fiber, aramid, wood, etc. as reinforcement.

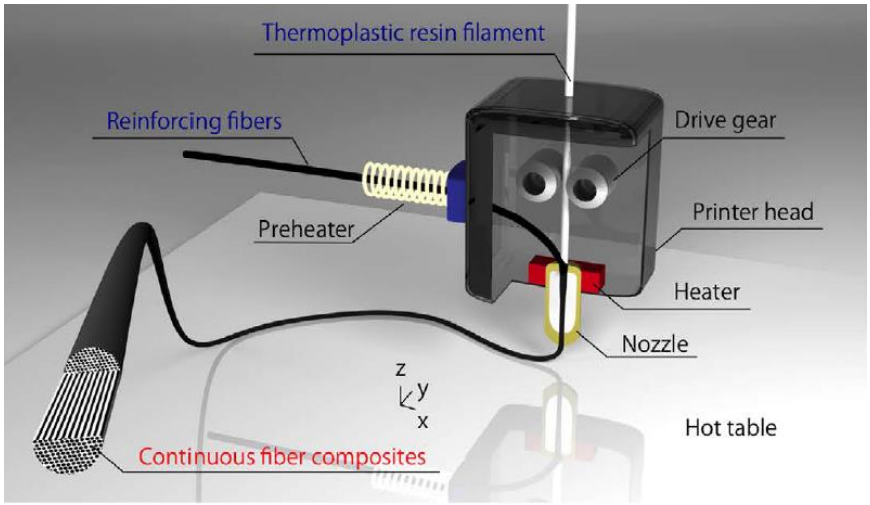

Fig 3. *Illustration of in-situ fusion FFF* [5].

1.2.1 Parameters Affecting FFF

Mechanical performance of printed samples can be affected by different printing parameters [6]. Material feed rates, printing temperature, nozzle shape, print bed temperature, viscosity of the flow and printing speed, layer thickness, etc. are the most important parameters. A visual representation of key parameters is shown in *figure 4*.

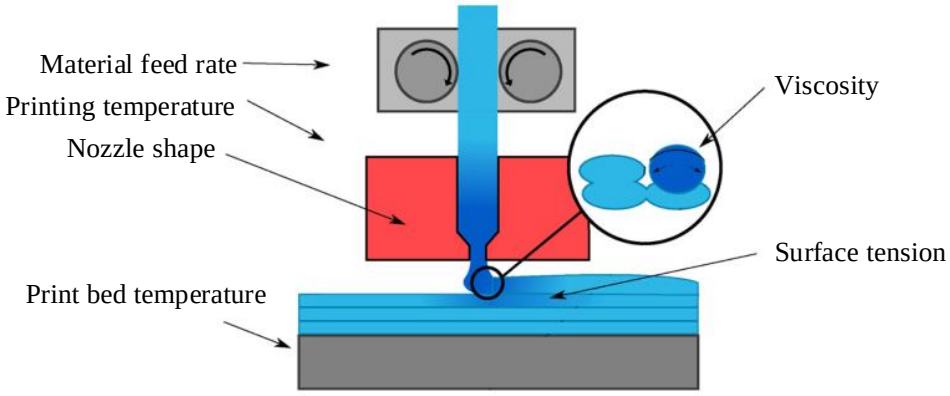

Fig 4. *Key parameters of 3D printing* [6].

In the fused filament fabrication thermoplastic is pushed through a set of roller mechanisms, in *figure 5*(A). To prevent unwanted slippage during feeding and create proper friction, a grooved or toothed surface gear can be present to grab the filament and feed [7]. The amount of melt in the melting zone has a direct dependency on the heating rate and material feeding rate [8]. With the increase of temperature, the viscosity of the melt decreases and helps to flow through the printer nozzle. Though high melting temperature is good for improving adhesion between the layers, too high temperature can instigate the polymer chain degradation [8].

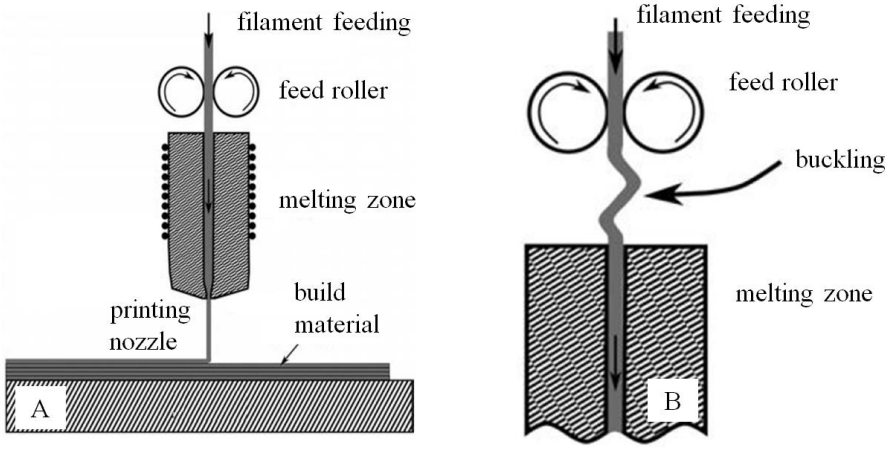

Fig 5. (A) *Roller mechanism*, (B) *Buckling phenomena* [9].

Sometimes, inside the melting zone, a pressure drop situation can happen because of the feeding rate and melting temperature [9]. It can lead to buckling in the feeding materials

between feed rollers and the melting zone [9]. To avoid this pressure drop in the melting zone should not exceed the critical pressure value achieved from Euler's buckling approximation. Mathematically Euler's approximation [10] can be expressed by:

$$P_{critical} = \frac{\pi^2 E d_f^2}{16 L_f^2} \qquad \text{---------- (1)}$$

Here, E is the filament´s elastic modulus, d_f is filament diameter, L_f is the filament length from the rollers to the entrance of the liquefier.

Melting zone and nozzle geometry have a direct impact on the melt flow behavior. Early days people used the horizontal cylindrical tube, curved 90^o before connecting between the nozzle and melting zone [11]. It is also believed that nozzle angle is one of the main players for the clogging effect inside nozzle [10]. At present people use a straight cylindrical tube with a shortened conical connection mostly with 120^o [10] to reduce pressure drop phenomena. It is believed pressure drop reduces with the increase of nozzle angle [11] [12].

Polymer melt experiences stress inside the nozzle as part of deformation energy [13]. When polymer melt leaves the printer's nozzle, it is no longer forced by the walls of the melting zone and stress starts to relax and occur radial expansion [13] which is known as die swelling.

The distance between the end of the nozzle or printing head and deposited road or layer has an impact on the distortion of the shape. When the nozzle is contacted with the road or layer, the surface will be flat and when the nozzle is a little bit above, road will be distorted because of die swelling [9], shown in *figure 6*.

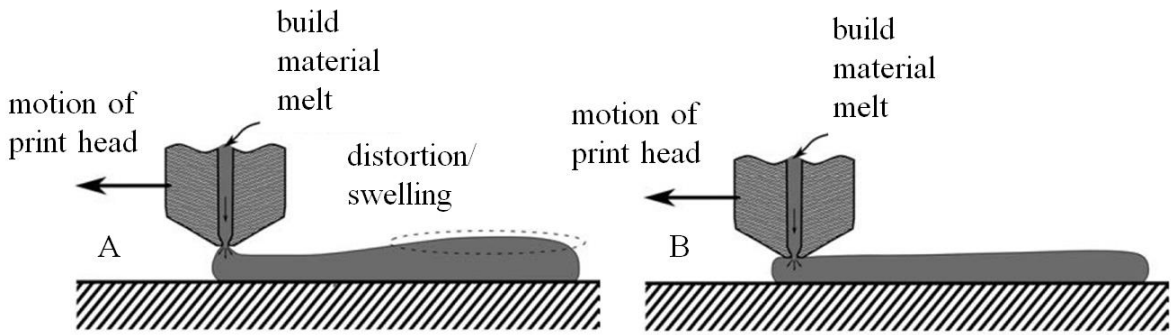

Fig 6. *Swelling effect* (A) *printing head is a little bit above,* (B) *printing head is touching the road* [9].

Uneven deposition, in *figure 7*, occurs depending on the material feed rate [7] [12]. When the feeding rate is lower and the printing head moves faster, it produces under-deposition effect. And a combination of lower feeding rate with slower printing head movement produces over-deposition. These variations have influence over the bead width [7].

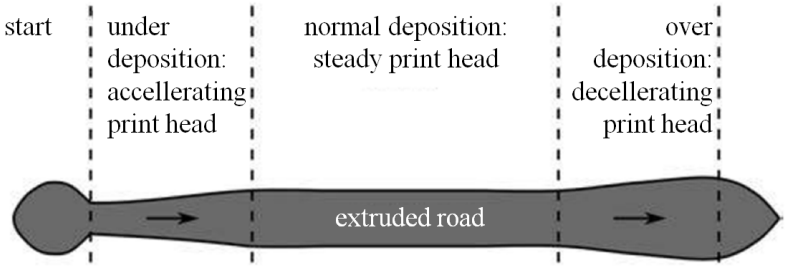

Fig 7. *Comparison of under, normal and over deposition* [7] [12].

The strength of the fused filament fabrication part depends on the bonding strength between the neighboring beads. Bond strength is also a function of adhesion and cohesion forces [9]. It is proven that thermoplastic materials road or layers bonding happens through thermally driven viscous flow mechanism, i.e. sintering process [14]. Glass transition temperature, T_g, is the key controlling parameter for the sintering process. When melt leaves the melting zone, temperature is way above T_g. On the other hand, build environment is far below T_g. The heat from the incoming melt comes from melting zone helps to increase the temperature of the road or previous layer to go above T_g. As a result, thermal conductivity and heat capacity of materials play a vital role [9].

Bonding of the fused filament fabrication process can happen by necking or neck formation, where viscous flow and molecular diffusion are key parameters, in *figure 8*. The previous study suggests that the initial interfacial molecular contact is achieved by wetting. Molecules undergo pre-offered configuration and achieve adsorption equilibrium [9]. Then molecules diffuse within each other in the area of interface and form an interfacial zone. Within this interfacial zone, molecules react with each other to form primary chemical bonds. Under certain critical conditions randomization can occur because of extensive inter-diffusion [15].

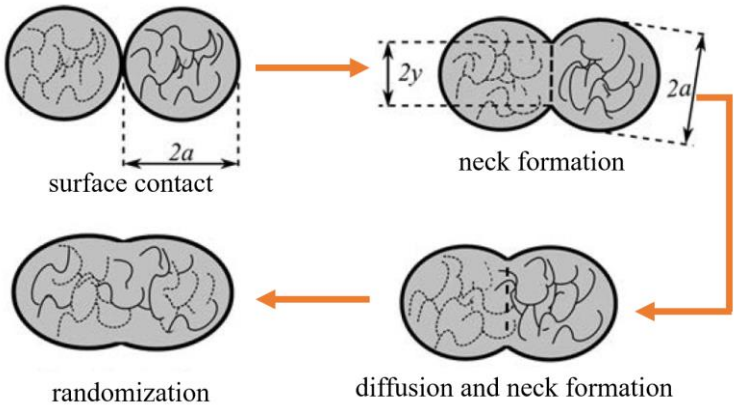

Fig 8. *Bond formation of FFF printing process* [9].

1.2.2 Comparison between FFF and Injection Moulding

The mechanical performance of the fused filament fabrication parts largely depends on the interlayer's bonding strength, which is also a week spot at the same time. According to the study [16], parts produced by injection molding has higher tensile strength than fused filament fabrication.

The study tried to compare varieties of the test specimens produced by altering layer thickness and orientation angle of rasters using fused filament fabrication process with the injection-molded specimen. As a material blend of polycarbonate and acrylonitrile butadiene styrene was used. Three different – 0^o, 90^o and concentric layout of layers – orientation angle of raster and two different – 0.127 mm and 0.330 mm – layer thickness were used. According to the tensile test result, in *figure 9*, injection-molded specimen possesses the highest tensile strength compared to printed specimens. Tensile strength increased with the increase of layer thickness and raster angles, and the underlying reason can be better homogeneity, better bonding, and reduction of unfilled space between layers. In general it is possible to achieve as close as tensile strength compared to the injection molded parts by reducing the unfilled spaces between the layers of printed parts.

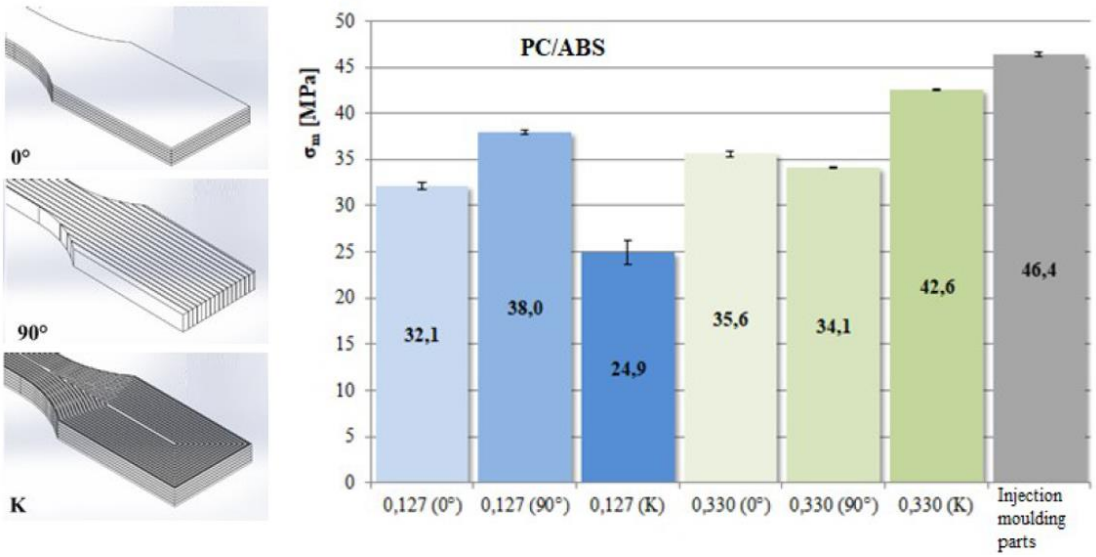

Fig 9. Tensile strength comparison of injection moulding and printed parts [16].

1.2.3 Influence of Fiber Length

Fiber length plays a vital role in the fiber-reinforced composites. Theoretically, critical fiber length is dependent on the fiber diameter, fiber strength in tension and the fiber matrix bond strength or shear strength of fiber matrix interface [2]. Mathematically it can be expressed as follows:

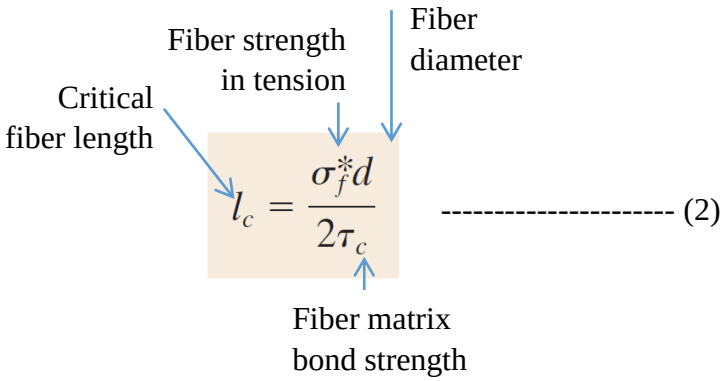

According to the literature [2] it is possible to happen three different events with the variation of critical fiber length. When the fiber length is equal to the critical length, maximum fiber load is possible to obtain at the axial center of the fiber. When the length of the fiber length is below critical fiber length, the fiber matrix bond may fail before fiber reach to the potential strength and the maximum fiber stress may never reach the ultimate fiber strength. And when the fiber length is greater than the critical fiber length, the maximum fiber stress may reach to the ultimate fiber strength over much of its length and over the distance of $l_c/2$ the fiber remains ineffective. The schematic of overall stress behavior with the fiber length is presented in *figure 10*.

Another study [17] suggests, mechanical performance does not solely depend on the fiber length but also has a connection with fiber dispersion. According to the study, mechanical properties after certain threshold can reduce as shown in *figure 11*. This phenomenon occurs because of the poor fiber dispersion and higher disorder, which are prominent for longer fiber lengths.

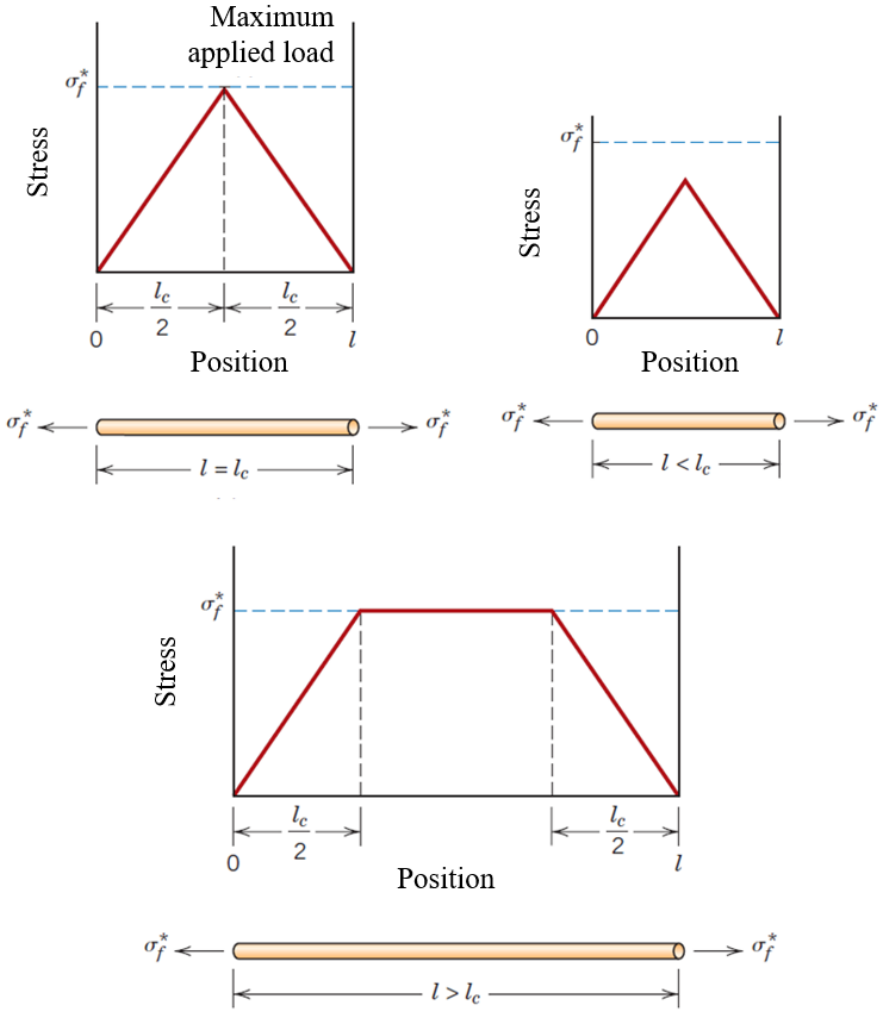

Fig 10. *Comparison between fiber length and critical fiber length* [2].

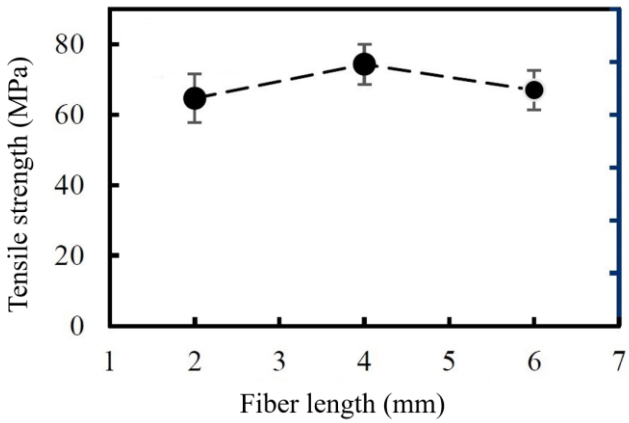

Fig 11. *Mechanical properties against fiber length* [17].

1.2.4 Relation of Fiber Percentage and Porosity

According to the study [18], fiber-reinforced composites printed by fused filament fabrication process have three different types of porosity which are shown in the scanning electron microscopy image in *figure 12*. The first one is a gas bubble, produced during the fabrication of feedback filament by extrusion. Second, interbead voids generated by the voids between different layers. The last one is fiber pull out, holes are generated by the pulled out fibers.

The overall porosity (P) can be expressed as:

$$P = \frac{V_t - V_a}{V_t} \qquad ----------(3)$$

Here, V_t is theoretical volume of the specimen after the FFF fabrication, V_a is the actual volume of the specimen.

To obtain the V_t, it was cut in smaller segments to avoid the fiber pull out voids from the calculation and weighed. The mass was then multiplied with the measured density of each segments to get the volume. The actual volume is possible to achieve by the following formula:

$$V_a = \frac{M \times \text{polymer wt.\%}}{\text{density of pure polymer}} + \frac{M \times \text{fiber wt.\%}}{\text{density of pure fiber}} \qquad ------(4)$$

Here, M is the actual mass of the specimen.

A further study [18] found that the overall porosity initially decreased with the addition of fibers, but when the weight percentage of fibers cross the threshold values porosity increases again.

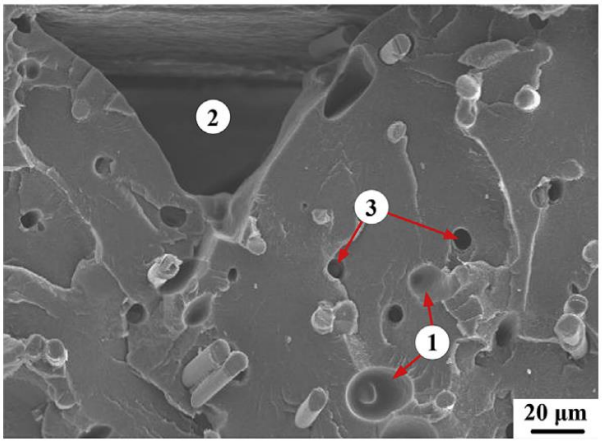

Fig 12. *Different types of porosity in FFF* [18].

CHAPTER 2

EXPERIMENTAL PROCEDURE & THEORETICAL BACKGROUND

This chapter is related to different experimental methods, theoretical background of these methods, and sample preparation of the tensile test, optical microscopy, density analysis, and burn test. Also setup procedure for the tensile test, optical microscopy, and x-ray computed tomography is discussed.

2.1 Sample Preparation

The samples were prepared by fused filament fabrication method in box shaped design at Brightlands Materials Center, Netherlands. Afterward, these boxes were milled at Fraunhofer IMWS, Halle according to the ISO 527-2 [19] type 1BA standard for tensile testing. The dimension and different parameters of type 1BA specimens are shown in *figure 13, figure 14* and *table 1*.

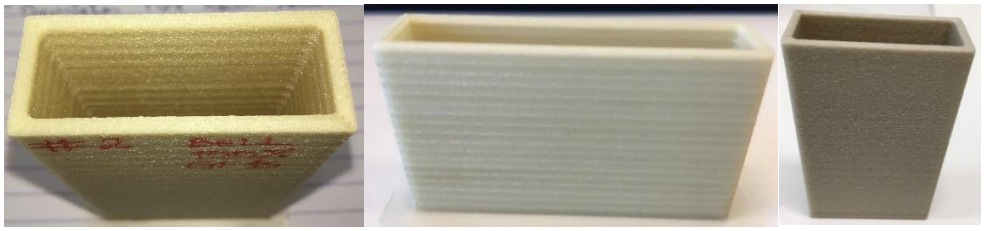

Fig 13. *Boxes produced by Brightlands.*

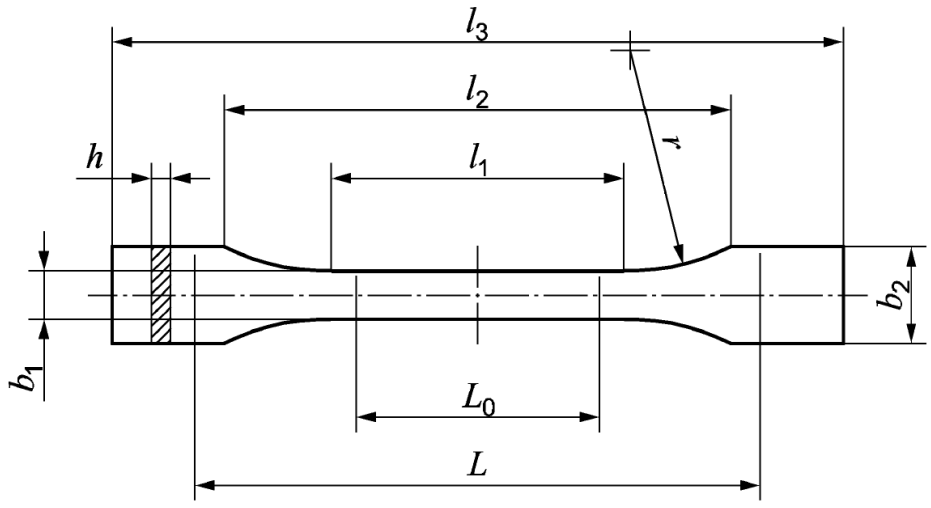

Fig 14. *Specimen according to ISO 527-2 type 1BA standard* [19].

Table 1. *Parameters for the test specimen of ISO 527-2 type 1BA* [19]:

Specimen Parameters		Dimension
l_3	Total length	≥ 75 mm
l_1	Length of narrow parallel part	30 ± 0.5 mm
l_2	Length of wide parallel sides	58 ± 2 mm
r	Radius	≥ 30 mm
b_2	Width at the ends	10 ± 0.5 mm
b_1	Width of the narrow part	5 ± 0.5 mm
h	Thickness	≥ 2 mm
L_o	Measuring length	10 ± 0.2 mm
L	Initial distance at the terminals	60 ± 2 mm

2.2 Specimen's Nomenclature

The details of the printing parameters with nomenclature are given in *table 2*. The illustration and specific details of the cut out tensile test specimen and orientation are presented in *figure 15* and *figure 16*. The raster angle decides the direction between the printing tracks and the application of the tensile load during tensile testing. The percentages of glass fibers within the composite are with respect to the weights. To maintain the heating temperature special types of heating technology were tested, which is confidential to Brightlands, Netherlands.

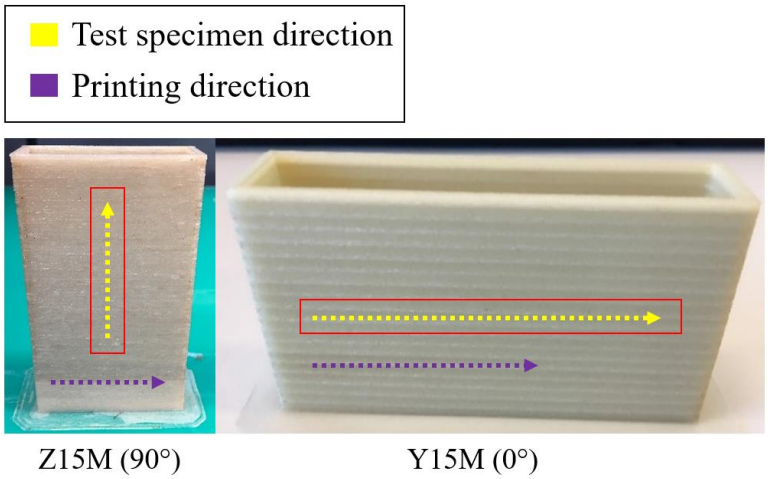

Fig 15. *Test specimen orientation.*

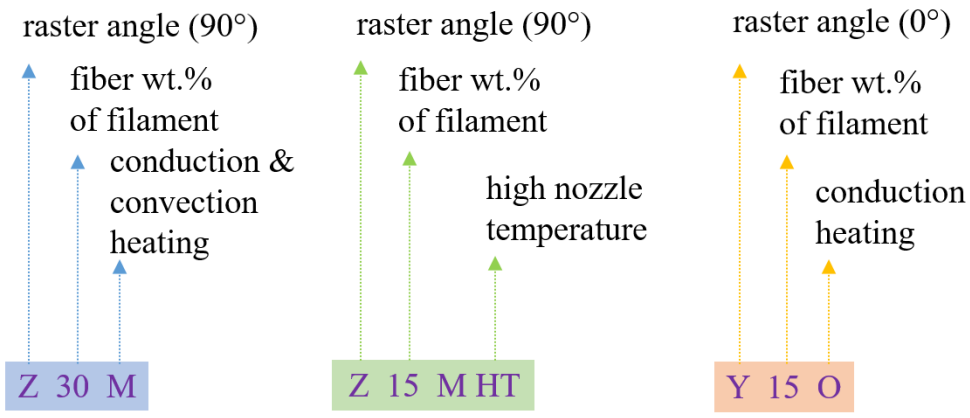

Fig 16. *Nomenclature of the test specimen.*

Table 2. *Parameters of the test specimen*

Name	Material	Nozzle Temp. (°C)	Extrusion Multiplier	Speed (mm/min)	Raster Angle	Heating
Z30M	PA6+ 30%GF	285	1.00	1200	90°	Conduction & Convection
Z30MHT		310	0.96	300		
Z30O		285		1200		Conduction
Z15M	PA6+ 15%GF	285	0.90	1200		Conduction & Convection
Z15MHT		310	0.90	300		
Z15O		285	0.90	1200		Conduction
Y30M	PA6+ 30%GF	285	0.96	1200	0°	Conduction & Convection
Y30O			0.96			Conduction
Y15M	PA6+ 15%GF		0.95			Conduction & Convection
Y15O			0.95			Conduction

In fused filament fabrication process it is possible to generate more pressure on the previous layers because of the material's own weight. A temperature gradient may also generate during the printing and after printing process inside the material because of the absence of a uniform cooling system. To explore these feasibilities samples were printed as box shape instead of dumble shape, in *figure 14*.

There are two different orientations used Z and Y, in *figure 19*. In Z-direction printer had to travel relatively shorter distances to complete a cycle and a longer distance in Y. The test specimens were cut respectively perpendicular to the printing direction for Z and parallel to the printing direction for Y. These two variations may provide the scope to test the mechanical performance towards the glass fiber's orientational direction and layer by layer bonding strength.

The presence of the weight percentage of glass fiber, printing nozzle temperature, printing speed, extrusion multiplier or material flow rate and heating system has been varied according to *table 2* during the printing process to explore different possibilities and observe mechanical performance. Other than that, specimens were cut from different positions of the printed boxes, *figure 84*. Which may also provide the scope to check the variation of the mechanical performance depending on the position of the specimen relative to the printing bed.

2.3 Specimen Conditioning

Conditioning is essential for polyamide (PA) materials because mechanical performance depends on the moisture content. Moisture content has a direct impact on the glass transition temperature (T_g) and glass transition temperature controls the hardness, brittleness, and even tensile properties of polyamide.

The DIN EN ISO 1110 [20], also known as accelerated conditioning standard was used to condition the boxes. Test samples were placed in a temperature-controlled cabinet capable of maintaining a temperature difference tolerance of ± 0.3ºC and relative humidity of 62% with a tolerance of ± 1%, in *figure 17*.

After conditioning for a period of time t_1 specimens were removed from the cabinet and allowed to cool for *1 hour* in a standard atmosphere of 23ºC, 50% relative humidity and weighed to the nearest 0.1 mg. The same procedure was repeated to get three consecutive weighings. When the three consecutive weighing differences were within 0.1%, the conditioning was assumed to be completed. However, it is recommended to keep the test samples in a standard atmosphere of 23º C and 50% relative humidity at least *one hour* before the testing. For this reason, every time after taking the boxes out of the conditioning zone was cooled down approximately 1 hour.

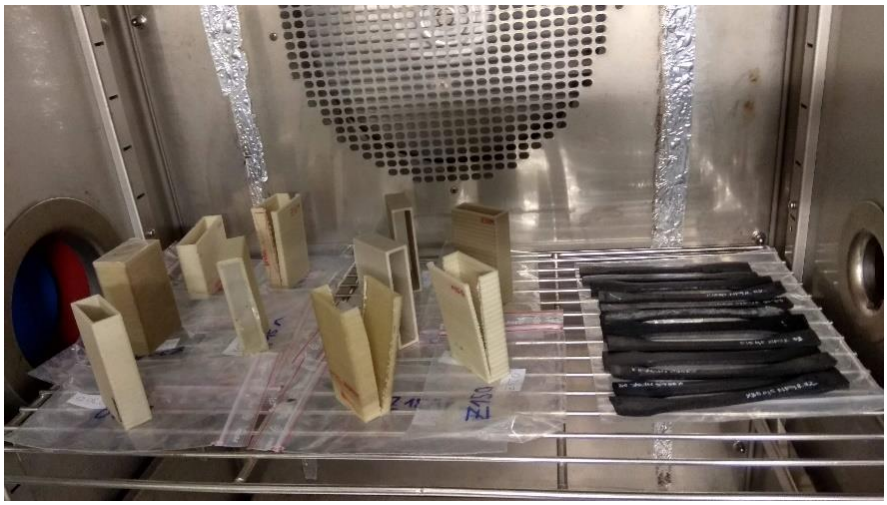

Fig 17. *Conditioning by climate chamber.*

Table 3. *Mass of samples conditioned according to ISO 1110 [28]*

Sample	Mass (g)				Difference (%)	
	Conditioning				After Second Stage $\frac{m(t_1)-m(t_2)}{m(t_1)}\times 100$	After Third Stage $\frac{m(t_2)-m(t_3)}{m(t_2)}\times 100$
	Before	First Stage (t_1=*2 days*)	Second Stage (t_2=*1 day*)	Third Stage (t_3=*1 day*)		
Z30M	26.511	26.850	26.844	26.825	0.022346369	0.070779318
Z30MHT	32.759	33.144	33.129	33.154	0.04525706	0.075462586
Z30O	26.497	26.764	26.732	26.751	0.119563593	0.071075864
Z15M	27.017	27.528	27.542	27.532	0.050857309	0.036308184
Z15MHT	23.547	23.863	23.844	23.849	0.079621171	0.020969636
Z15O	27.320	27.720	27.729	27.710	0.032467532	0.068520322
Y30M	25.449	25.749	25.742	25.755	0.027185522	0.050501127
Y30O	25.318	25.558	25.560	25.559	0.007825338	0.003912363
Y15M	24.508	24.964	24.969	24.983	0.020028842	0.056069526
Y15O	27.161	27.605	27.616	27.631	0.039847854	0.054316338

2.4 Tensile Test

The tensile tests of the specimens were performed using Zwick Roell Z050 universal testing machine to observe mechanical behavior under uniaxial stress. The universal testing machine consists of movable upper and stationary lower fixing clamps and the movable clamp is operated by software. The test specimen is mounted inside the clamps and fixed with a manual tightening screw. The top of the upper clamps load cell is mounted, and the load is decided to depend on the tested materials. The load is applied to the test specimen until the fracture point. Various sensors detect displacement and applied load and the real-time force-strain curve is generated in the TestXpert II software. An illustration of different parts of the universal testing setup is given in *figure 18*.

Prior to mount the test specimens in the clamps it is important to measure the width and thickness. These values were also required to input in the software to calculate stress. The ambient temperature and humidity were also recorded.

The gauge length, clamp to clamp distance and the test speed is defined according to ISO 527-2 [19] type 1BA standard. *Table 4* represents the overall parameters that were used for tensile testing.

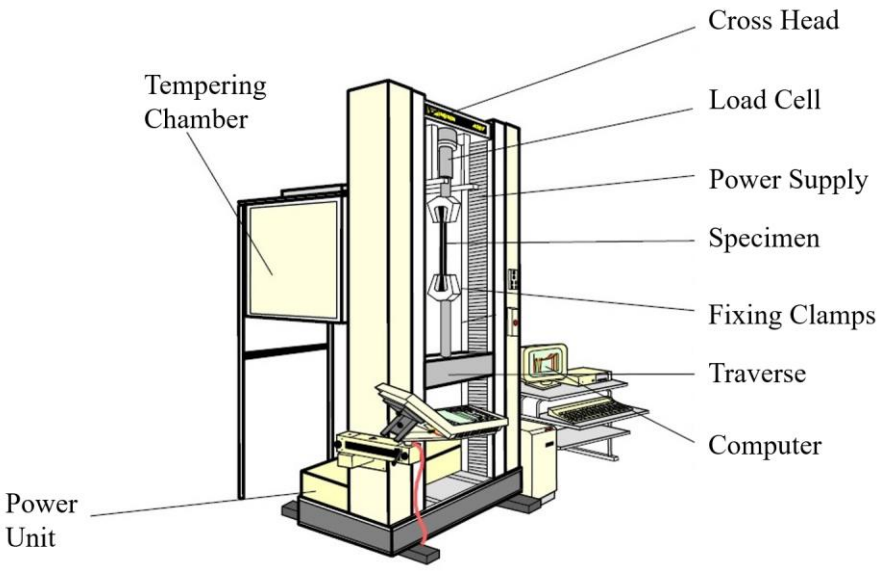

Fig 18. *Illustration of different parts of tensile testing machines.*

Table 4. *Test parameters in Zwick Roell Z050 according to ISO 527-2* [27] *type 1BA standard.*

Test Machine	Zwick Roell Z050
Test standard	ISO 527-2 1BA
Testing speed (elastic modulus)	1 mm/min (strain limit 0.05% - 0.25%)
Testing speed (after elastic modulus)	5 mm/min
Clamps load	10 kN
Traverse	2.5 kN
Pre-load	0.5 N
Grip to grip separation 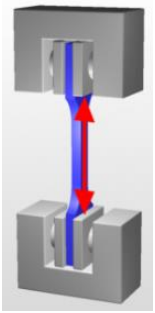	58 mm
Gauge length 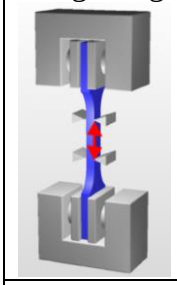	25 mm
Temperature	23.7 ºC (Example temperature recorded during the test)
Relative humidity	55.1 % (Example relative humidity recorded during the test)

2.5 Microstructure by Optical Microscopy

Optical microscopy (OM) is one the primary means to examine the microstructure of materials. To see the characteristic features and surface of manufactured specimen optical microscopy is one of the commonly used methods. Although the range of the OM is limited and possible to reach up to the micrometer (μm) scale. This range is quite enough to observe the microstructure features of composite materials. A schematic of different parts of optical microscopy is shown in *figure 19*.

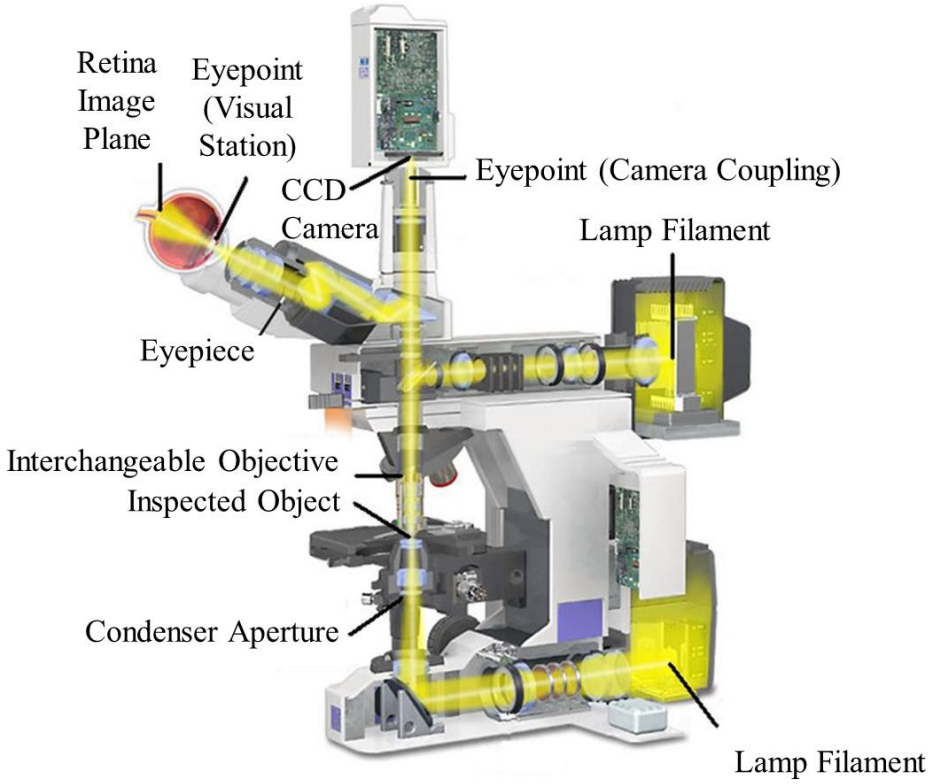

Fig 19. *Different parts of optical microscope* [20].

Bright-field imaging is the most used mode for observing microstructure. It is suitable for seeing the natural colors and the sample appears darker on a bright background [21]. The specimen is evenly illuminated by a light source. Some light is absorbed and reflected by the opaque samples and the rest of the light passes through the objective lens. *Dark-field imaging* requires illuminated by oblique light rays [21]. No light goes into the objective directly and scattered by the sample. Mostly used for organic samples imaging. However, dark field images are prone to degradation, distortion and very thin layered specimen are required, otherwise, may have artifacts throughout the image. *Figure 20* is showing a side by side comparison of brightfield and darkfield imaging. The brightfield sample is easy to differentiate from the background which is useful to observe and measure the microstructural features. In this regard, in this study all of the pictures obtained by bright field technique.

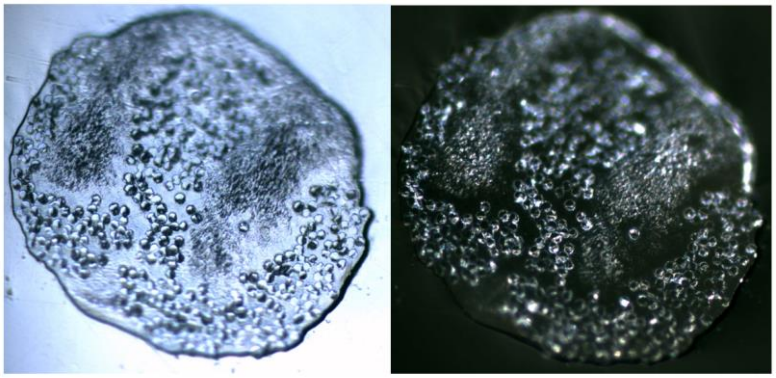

Fig 20. *Brightfield and darkfield optical microscopy image.*

To investigate top and cross-sectional views of printed parts OM (Olympus BX51) was used. The microstructure of a material can only be seen under OM after a specimen was properly prepared.

2.5.1 Sample Preparation

Sectioning, *mounting*, *grinding*, and *polishing* are the main steps of specimen preparation for OPM [21]. *Sectioning* mainly helps to generate a cross-section of the specimen to be investigated and reduce the size of the specimen to be embedded in mounting media. A general cutting blade was used to prepare the specimens. And from each of the boxes, two different specimens were cut out, in *figure 21*.

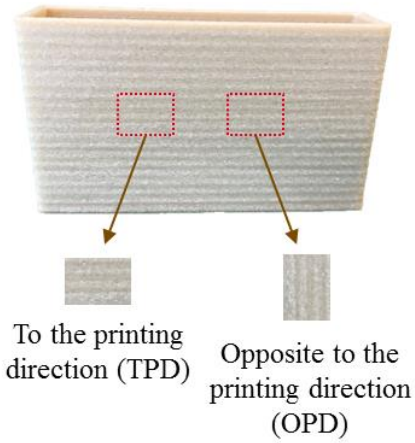

Fig 21. *Types of specimens cut from the printed box.*

Mounting assists to hold the specimen during the embedding process. Hot mounting and cold mounting are the two main types of mounting techniques. In cold mounting a polymer resin, known as SpeciFix-20 were used. It has two parts resin and curing agent (7:1 ratio). The specimen should be as centered on the mold as possible, in *figure 22*. It was important to mix both of the chemicals around 3 minutes before pouring in the specimen's mold. The mixture took approximately 1 hour to become harder and mandatorily kept for 8 hours to be cured properly.

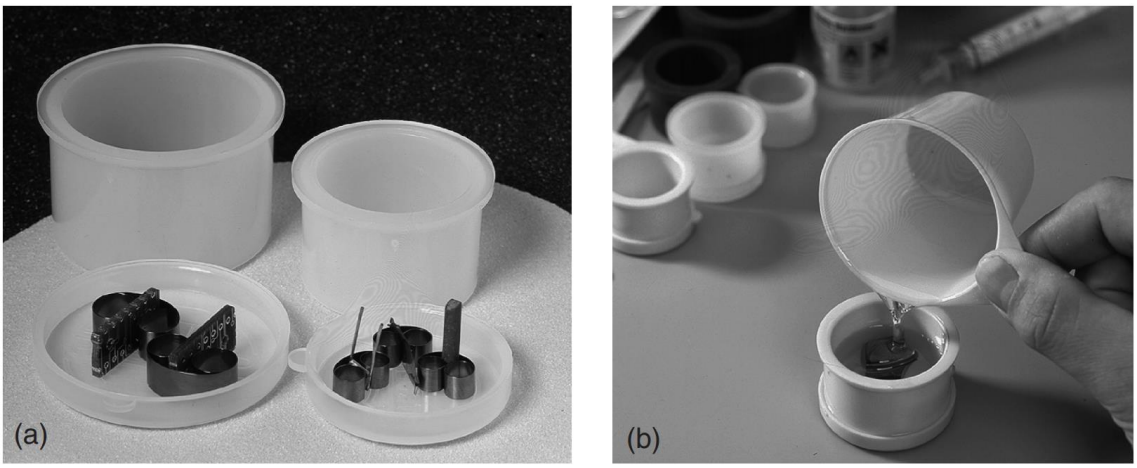

Fig 22. *Specimen mounting and embedding process:* (a) *mounting*, (b) *embedding* [22].

The grinding process helps to flatten the damaged surface caused by sectioning. And polishing refers to generate a mirror-like finish by eliminating unwanted scratches from the surface. Although grinding and polishing can be done by a mechanical process, in this investigation a manual system *Mintech 333 Presi* was used, in *figure 23*(A). Keeping the specimen cool and clean continuous water supply was also applied during the grinding-polishing process.

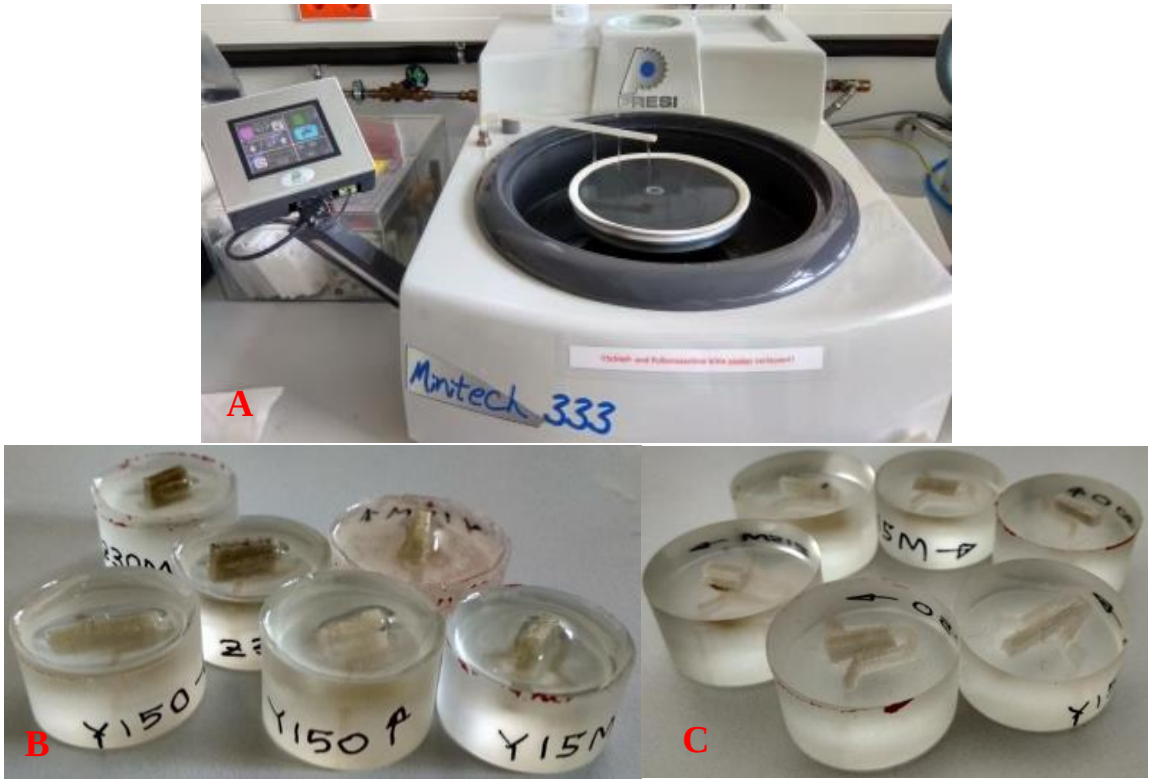

Fig 23. (A) *Grinding and polishing by Mintech 333 Presi,*
(B) *before grinding-polishing,* (C) *middle of grinding-polishing.*

According to the Federation of European Producers of Abrasives (FEPA) there are various particle sizes of abrasive papers. Larger particle paper is usually used for grinding and smaller to finer particle paper for polishing purposes.

Both grinding and polishing were achieved by using a series of abrasive or sandpapers, mainly descending order of the grain size. In the beginning, a bigger grain abrasive paper produced with silicon carbide P120 was used and then P800 according to FEPA [23] standard. The surface of the samples was already smooth but bigger scratches were present. To reduce and eliminate the surface scratches additional two steps were performed, P1200 and P4000.

2.5.2 Optical Microscopy Images

After grinding and polishing the samples were placed under the lens of the microscope and the cross-sectional features were observed in the computer screen with the help of a camera mounted on the top of the microscope. Focus, contrast, zooming were adjustable according to user preferences. An example of surface features with different zooming is shown in *figure 24*.

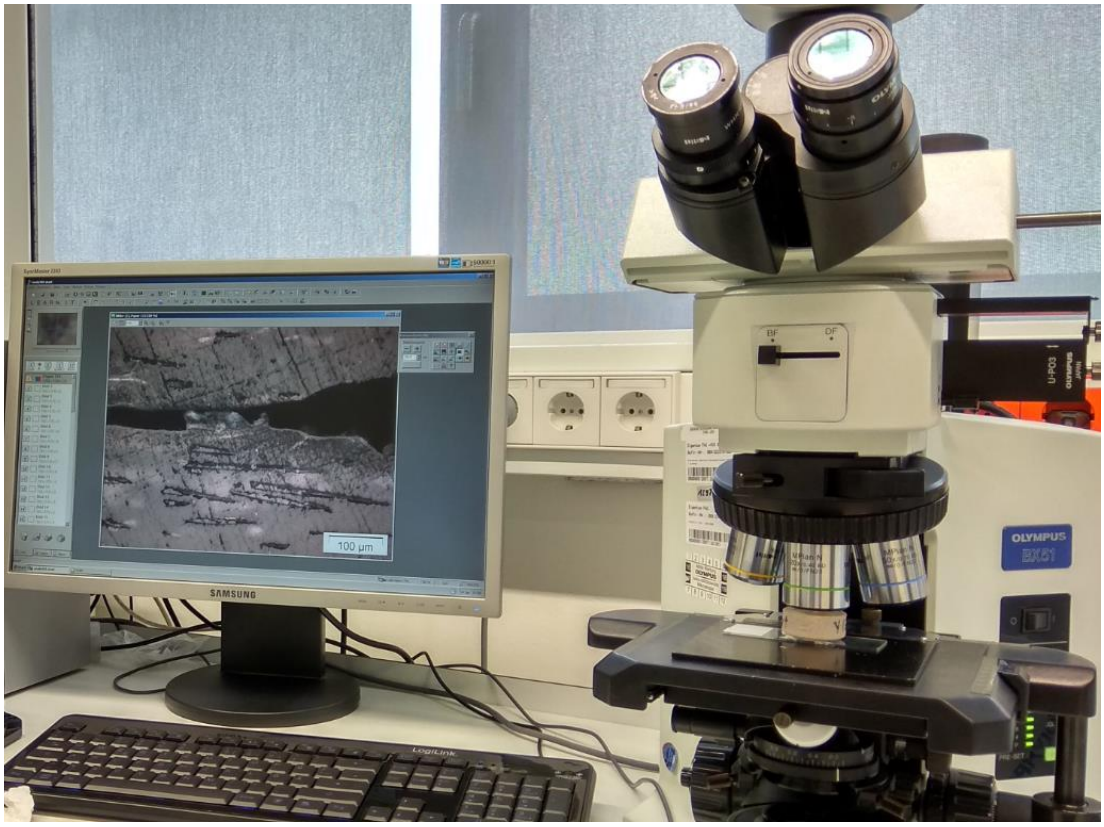

Fig 24. *Optical microscope & sample cross section.*

Zooming helps to find and focus on desired surface features. The experimental samples were produced with polyamide-based short glass fiber. Potentially it is possible to look in a greater surface area with fewer surface details, in *figure 25*. Bonding among the layers, gaps between the printing tracks, and voids present on the surface are also possible to find out. With the increase of the zooming focus area on the sample surface reduced, but surface features are more prominent. At 5x, 10x and 20x zoom surface features likewise voids and glass fiber are more prominent. It is also possible to measure the diameter, fiber length of short glass fiber and fiber weight percentage of filament from the higher zoomed microscopy pictures.

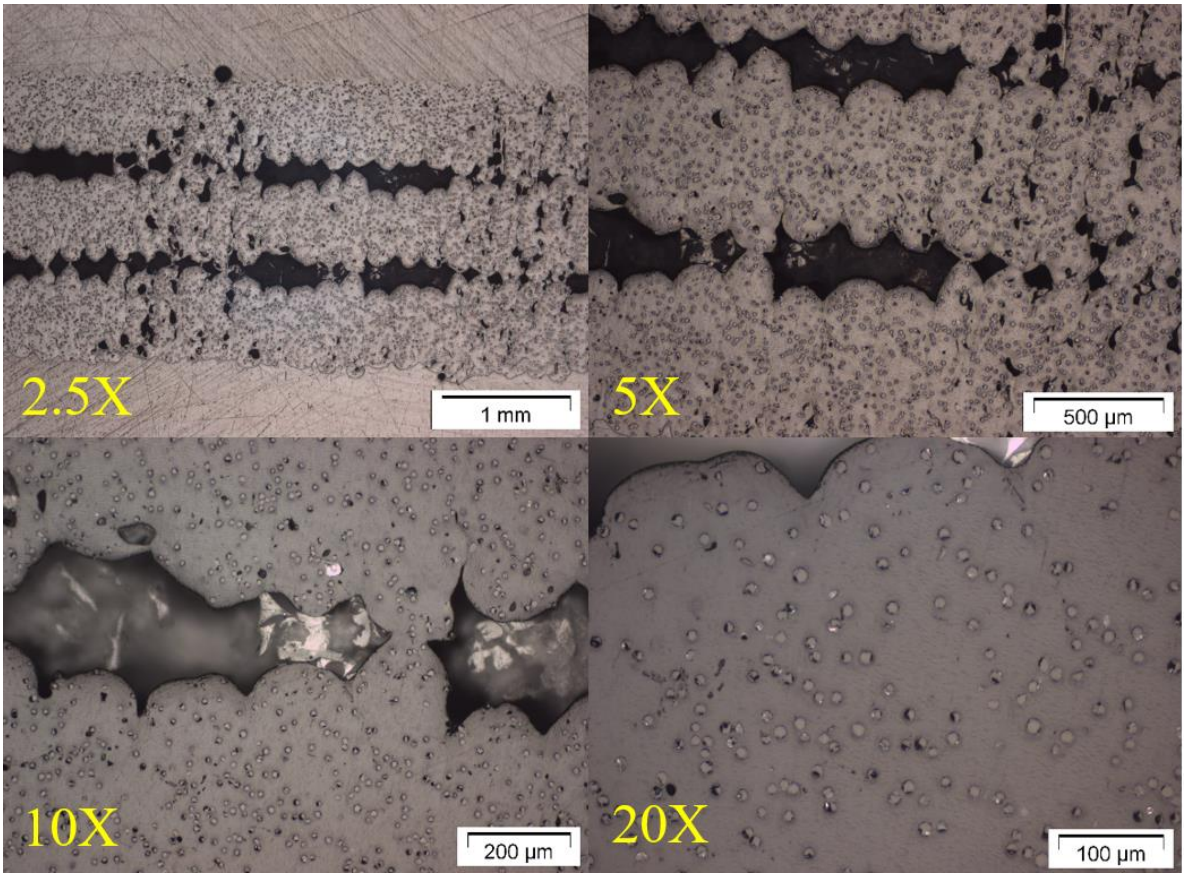

Fig 25. *Surface features under OPM.*

2.6 Computed Tomography (XCT)

Manufacturing defects in inner structure can cause significant degradation of the structural behavior of composites and x-ray computed tomography (XCT) assessment is one of the good ways of investigating these micro defects [24] without destroying the object. The word *'tomography'* derives from the Greek word *'tomos'* means slicing the object and *'graphein'* means recording the image.

2.6.1 Working Principle

The basic idea is to take multiple x-ray images from various angles around the object and compile them together using computer algorithms to construct 3D image of the entire object [25] [26]. The XCT is being used to analyze the microstructure by observing the inner structure and porosity. Additive manufactured parts have a strong dependence on porosity or voids, also have a tendency to de-bond between layers which is also counting as microstructural defects.

Depending on the speed of data collection and image reconstruction there are mainly three different types of XCT that have been developed: pencil beam, fan and cone beam. The *pencil beam* x-ray sends the density along the beam to the detector. The rotatable detector can rotate a full 360^0 arc with the desired increment facility specified by the user. A *fan-beam* geometry can be achieved by using a point x-ray source and assigning a detector on the other side of the object. This method can be either equidistant or equiangular intervals depending on the detector types. The equidistant intervals are possible to obtain by planar detector after placing the detector with an equal distance. The equiangular intervals are possible with circular detector by positioning the detector on the arc of a circle with its central position of the X-ray source. The *cone-beam* geometry uses a cone-shaped beam and a reciprocating solid-state flat panel detector. The detector can rotate around the object able to cover defined volume. Each scan (rotation) captures planned data and reconstruct using computer algorithms. *Figure 26* depicts the working principle of these three types of XCT.

The resolution and contrast of the image is the prime concern for the XCT measurements. As the XCT depends on the penetration, the size of the object is also important. Greater the size of the object reduces the maximum possible magnification as well as the image quality.

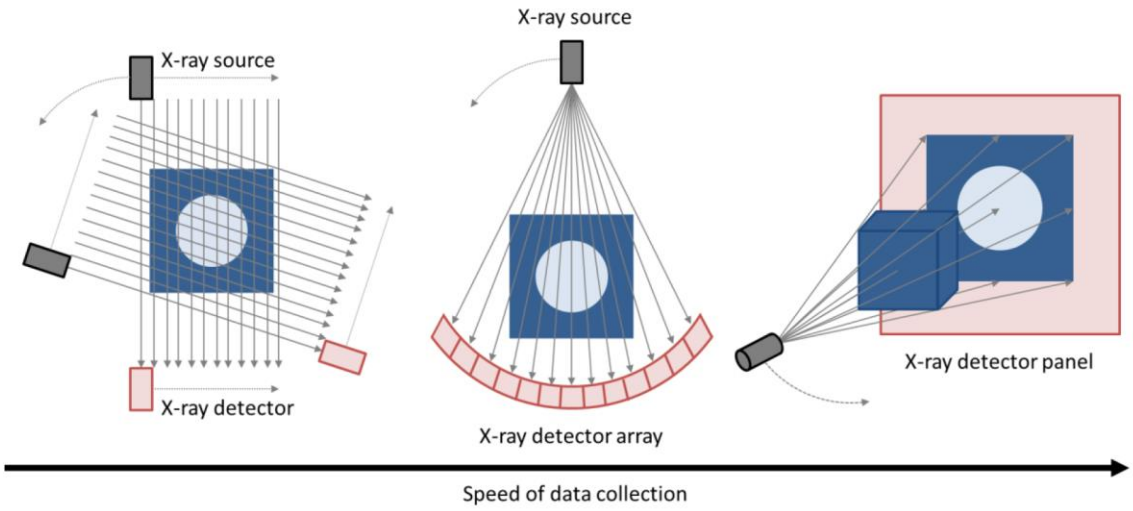

Fig 26. *Principle of pencil, fan and cone beam XCT methods* [27].

2.6.2 Scanning Setup

X-ray scanning of the printed specimen was performed using Rayscan 200E using a resolution with a voxel size of 20 µm. Then these images were used to analyze fiber orientation and porosity percentage by VG studio software.

The Rayscan 200E machine consists of a vertically movable x-ray source, sample base plate with a horizontally movable 360º turntable, vertically movable column of x-ray detector and follows the cone beam construction principle. An illustration of the working principle is shown in *figure 28*. According to the principle, the x-ray source radiates a conical beam and impacts on the sample placed on the turntable then goes through the detector. The sample holder turntable can rotate 360º and ensure 3D scanning of the sample. A series of images were recorded with a small angle of increment around the sample and sent to reconstruct cluster for material properties analysis by Volume Graphics (VG) studio software.

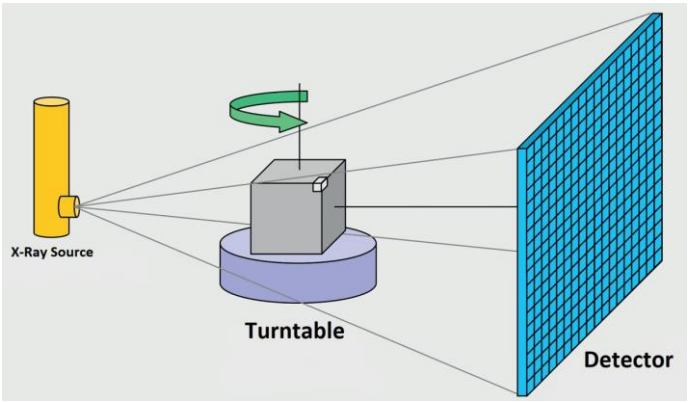

Fig 27. *Illustration of working principle of Rayscan 200E* [28].

2.7 Density measurement

Measurement of density is important to ensure quality, especially the porosity and microvoids of manufactured parts can influence the density performance. For example, an internal air bubble can cause failure under stress [29], improper distribution of the fiber may also change desired density hence the mechanical performance.

There are three different types of density measurement techniques for the printed composite materials [30] such as the Archimedes method, micrograph of a cross-section, and x-ray scanning. Among these methods, Archimedes is the most accurate one [30]. In this investigation the Archimedes method will be used.

2.7.1 Archimedes method

The density of the printed composite samples can be obtained by the Archimedes principle using Mettler balance, in *figure 28*. The weight of the samples is measured in air (A) and then again (B) in the auxiliary liquid. The density of the printed composites samples, ρ can be calculated as follows:

$$\rho = \frac{\mathrm{A}}{\mathrm{A}-\mathrm{B}}(\rho_l - \rho_o) + \rho_o \qquad ----------(5)$$

Here,

ρ = density of the printed composite samples
A = weight of the printed composite samples in air
B = weight of the printed composite samples in the auxiliary liquid
ρ_o = density of the air
ρ_l = density of the auxiliary liquid

The temperature of the auxiliary liquid must be taken into account, because the density of the auxiliary liquid may change to the order of the magnitude 0.001 to 0.1 with the change of temperature per degree centigrade. However, any void or pore that is not open, i.e. no liquid can flow in, reduces the density. At the time of sample preparation open porosity is not measured.

Fig 28. *Density measurement using Mettler balance* [29].

2.7.2 Density Measurement Setup

The way of density measurement by the Archimedes principle as previously discussed in section 2.7.1. The ISO 1183-1 [31] standard was maintained during the density measurement and as the auxiliary liquid ethanol was used.

Prior to the measurement, around one gram of sample was cut out from the three different positions namely top, middle and bottom of the printed boxes, shown in *figure 30*. In other words, top one is 75mm away from the printing bed, middle one is 40mm and bottom one is 5mm away for the Z directional boxes. Top, middle and bottom is respectively 35mm, 20mm and 5mm away from the printing bed for the Y directional boxes. A weighing setup consisting of ethanol containing beaker, a steelhead sample holder, and a thermometer was mounted on a balance that can give at least three digits after the decimal point. Firstly weight of the samples was measured in the air by placing the samples on the top of the steelhead. Then the samples were dipped in the liquid and the weight measured and using the *formula 5* density were calculated. To have the record of the temperature is also important as it has impact on the density of the auxiliary liquid. The overall setup for the density measurement is given in *figure 29*.

Fig 29. *Density measurement by Archimedes principle.*

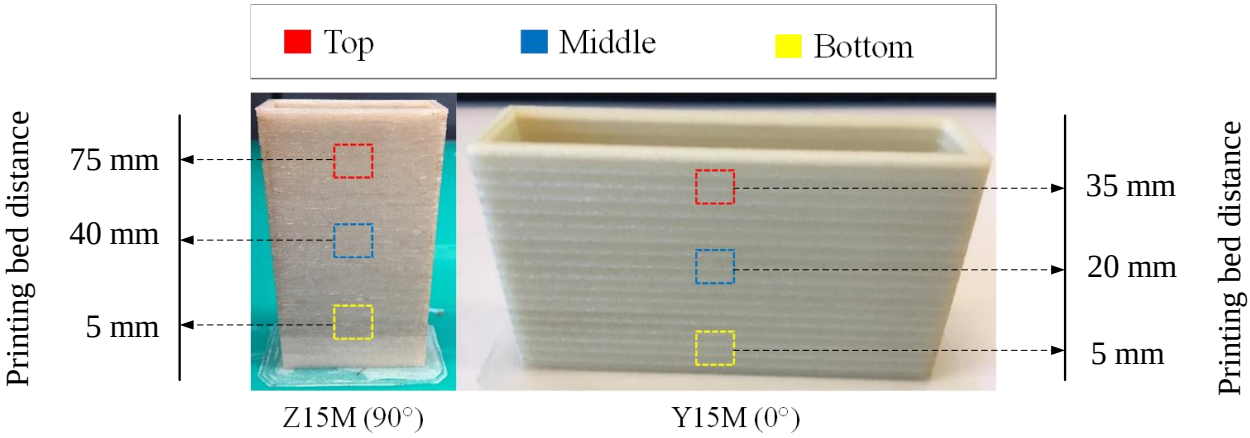

Fig 30. *Position of the samples to the printing bed.*

2.8 Burn Test

The fiber weight fraction of fiber-reinforced composite has an influence on mechanical performance. Apart from fibers the fiber-reinforced composite also contains polymer as a matrix, which has a lower melting temperature than fibers. This is the reason why to determine the fiber weight fraction burn test is one of the most commonly used methods. Measuring the difference between the sample weight before burning and sample weight after burning, it is possible to find out the fiber weight fraction.

To perform the burn test DIN EN ISO 1172:1992 [32] standard was followed. Firstly the specimens were cut out in a shape that allows them to fit into a silica boat or porcelain crucible. The clean, dry crucible was weighed to the nearest 0.1 mg on the balance and placed in the muffle furnace at 105ºC for 10 min. After cooling to ambient temperature in the desiccator it was verified that the mass had not changed. The mass of this crucible was recorded as m_1. A specimen was placed in the crucible and dried in a ventilated drying oven at 105^0C until constant mass obtained. When it reached the constant mass, the specimen with crucible was cooled to ambient temperature in the desiccator and weighed as m_2. Lastly, the crucible containing the test specimen was placed in the muffle furnace, preheated to a temperature of 625ºC and waited until getting constant mass. The crucible with the residue was allowed to cool in the desiccator to ambient temperature and weighed as m_3.

The final calculation was done using the following formula:

$$M_{glass} = \frac{m_3 - m_1}{m_2 - m_1} \times 100\ \% \quad ----------(6)$$

Here,

M_{glass} is the weight fraction of short glass fiber
m_1 is the initial mass of the dry crucible (in grams)
m_2 is the initial mass of the dry crucible plus dried specimen (in grams)
m_3 is the final mass of the crucible plus residue after calcination (in grams)

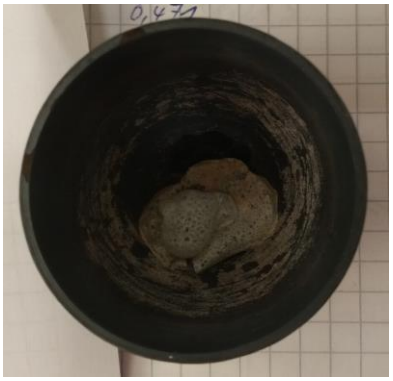

Fig 31. *Crucible with specimen during burn test.*

CHAPTER 3

RESULTS AND DISCUSSION

3.1 Optical Microscopy

The cutting and assessing process of the optical microscopy samples are already discussed under *section 2.5.1* and *section 2.5.2*. The goal was to observe the cross-section from both opposite to the printing direction (OPD) and towards the printing direction (TPD) from each of the samples under the optical microscope.

3.1.1 Analysis of Z30M Samples

The optical microscopy images indicate that the short glass fibers are distributed perpendicular to the OPD images of the sample and lengthwise in the TPD image, shown in *figure 31*. There are mainly two types of gaps are present- the tracks gap between the printing tracks and air gaps due to the presence of the air bubbles inside the material. It also indicates the gaps between the printing tracks are not always even in shape, somewhere the gap is narrow and somewhere it is wider. This uneven gaps may indicate uneven material deposition during printing mentioned in *section 1.2.1*. Besides, all the air gaps present inside the material may not certainly be produced by the air, some of them can be formed by the moisture absorbed by the printed material because of having water absorbency nature of polyamide. On the other hand, OPD images mainly show the bonding between the printing layers- the bigger the gaps, the weaker the bond. This bonding or upward directional gaps especially going to impact directly on the tensile strength performance.

The worse scenario appears from the TPD images. Gaps (sidewise) between the tracks are smaller than the gaps (upwards) of OPD images. Such gaps have usually less impact on tensile strength performance. The number of voids and air gaps is higher, which has an influence on tensile strength performance. Most importantly all the short glass fibers are not distributed along the printing direction or tracks.

There is another thing to be noted from the TPD image of Z30M specimen, *figure 32*, in some places, the short glass fibers are distributed parallel to the printing tracks and some are not. The deviation of the fibers mostly happens near the printing tracks gap, air gaps, and edges of the tracks. These voids and random distribution of short glass fiber, in *figure 33*, may have an impact on mechanical performance. Although for the Z samples all the glass fiber has no influence because of the testing direction, it is clear from the microscopy images that all the glass fiber inside the printed cross-section is not equal in length, some of them are big and some are small. Theoretically, these short glass fiber should have to be equal in length, but this deviation may also indicate the breakage of the short glass fiber during the printing process.

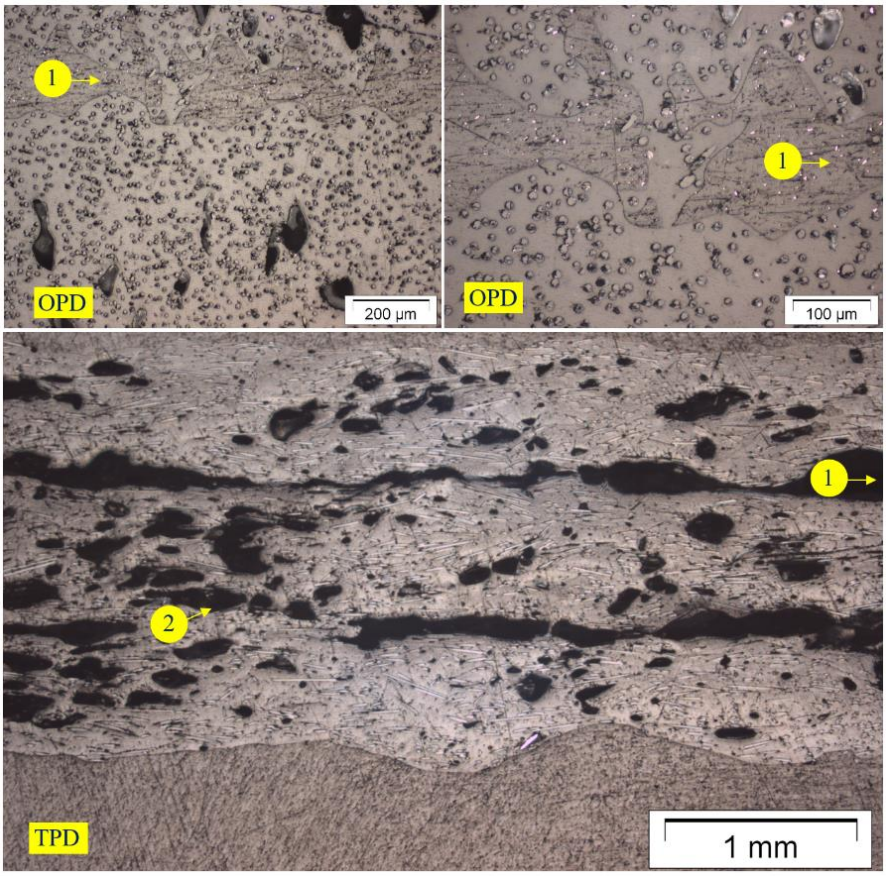

Fig 32. *Optical microscopy images of* Z30M*:* (1) *gap between the tracks,* (2) *air gap.*

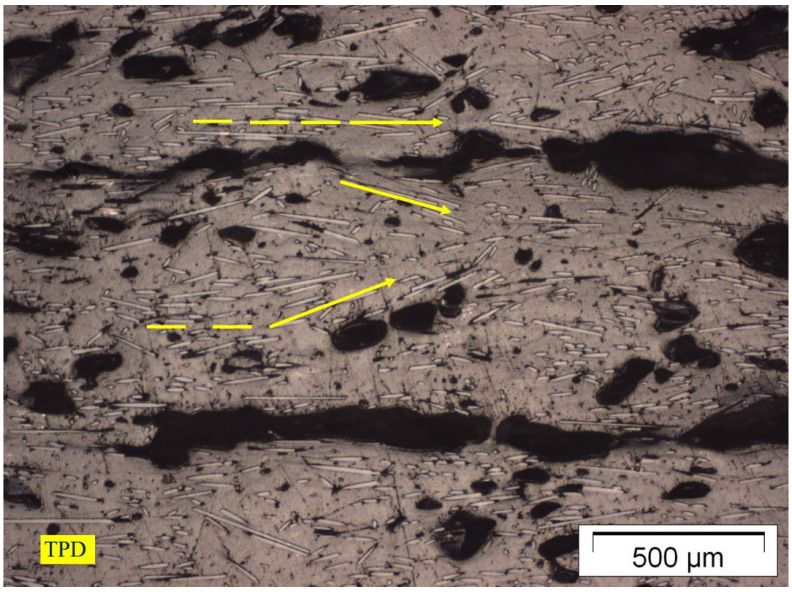

Fig 33. *Distribution of short glass fiber of* Z30M.

3.1.2 Analysis of Z30MHT Samples

Both the OPD and TPD images of Z30MHT, *figure 34*, shows printing tracks or layers are not evenly printed. It has all combinations of under deposition, over deposition and normal deposition of the melted material extruded through the printer nozzle during the printing. The OPD images indicate that there are wider gaps (sidewise) between the printing tracks. These tracks are representing the bonding strength between the layers of this kind of sample, which is going to impact the tensile strength performance. One thing is good here that is the air gaps or bubbles, very few compared to the Z30M.

The gaps (upwards) between the tracks in the TPD images are also very prominent. There is no bonding between the tracks at all, which may have dried out before coming to the contact with each other, which may impact the early de-bonding during tensile testing. All the short glass fibers are not distributed along the printing direction or tracks and randomization happens mainly near the edges of the printing tracks. The length of the short glass fiber is not also equal, some of them are small and some are long, possibly breakage happens during the printing.

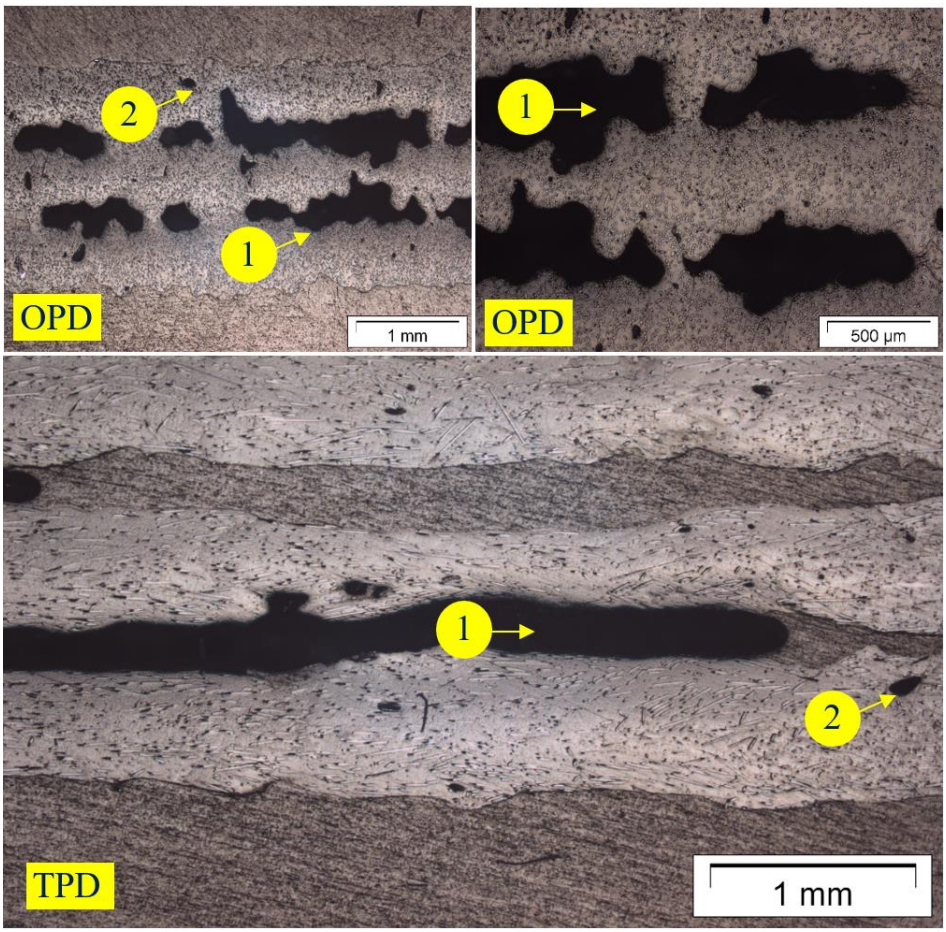

Fig 34. *Optical microscopy images of* Z30MHT*:* (1) *gap between the tracks*, (2) *air gap.*

3.1.3 Analysis of Z30O Samples

The optical microscopy images of Z30O indicate to have a lot of voids, air gaps inside the printed material, *figure 35*. The inter tracks or layers bonding is poor because of voids, visible from the OPD images. This will easily have an impact on the tensile performance of the overall samples.

The gaps (sidewise) between the tracks is severed in the case of TPD images. Printing tracks width is not even for the entire cross-section, somewhere it is over deposited, somewhere under deposit. Inner material bonding is also poor, leaving a lot of air gaps or voids, bubbles. The short glass fibers are not always distributed along the printing tracks and the randomization happens, *figure 36*, near the printing tracks gap, air gaps, and edges of the tracks. The short glass fiber length is also not even in length, may be damaged or broken during the extraction process through the nozzle.

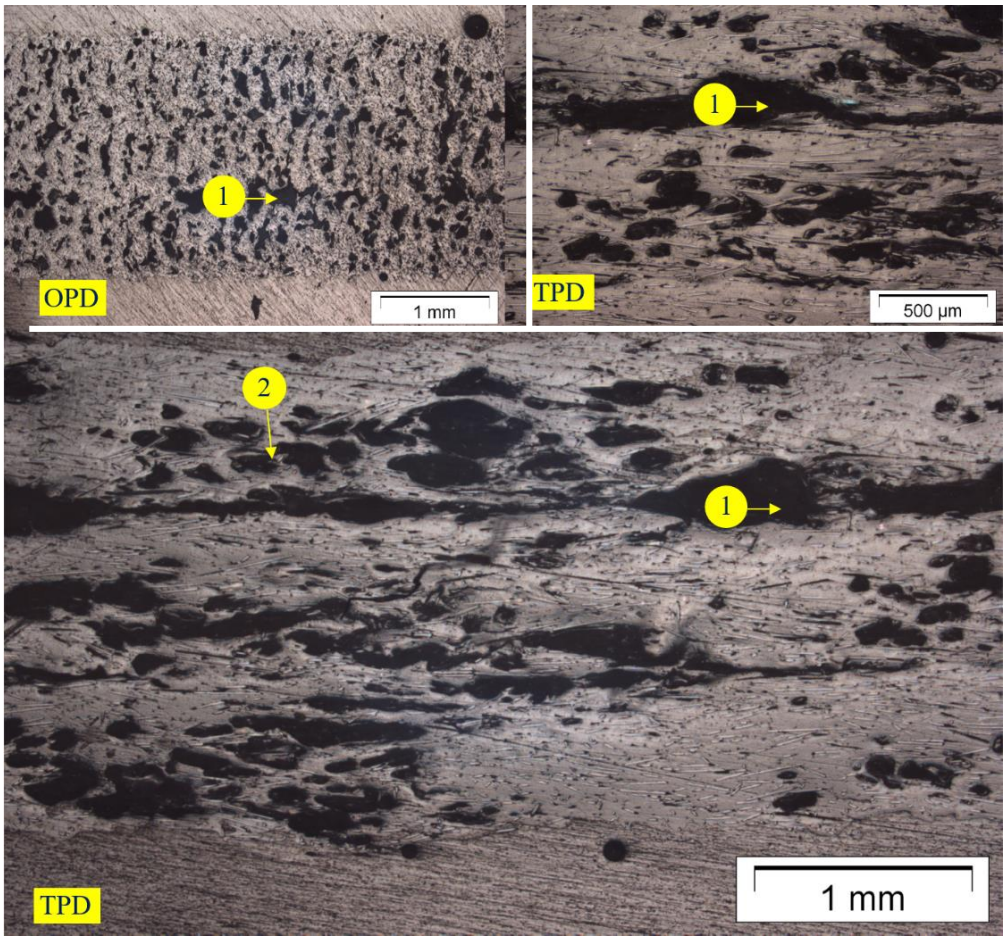

Fig 35. *Optical microscopy images of* Z30O*:* (1) *gap between the tracks,* (2) *air gap.*

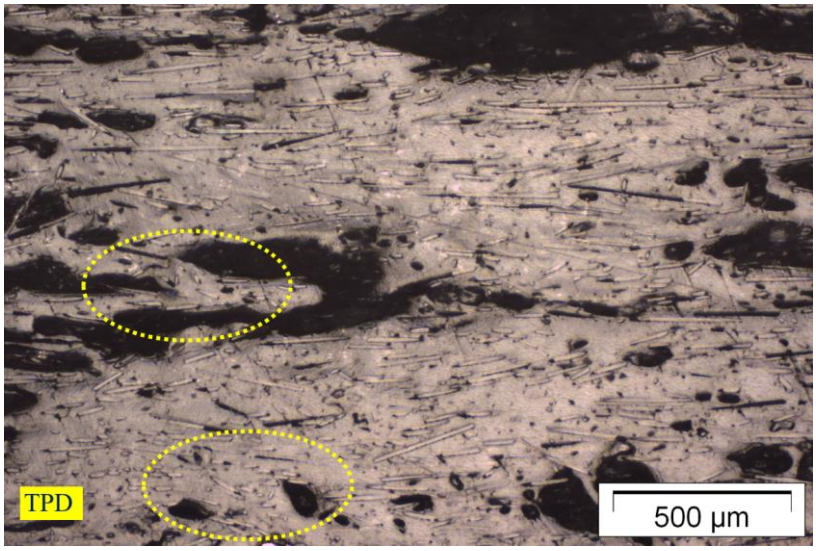

Fig 36. *Distribution of short glass fiber of* Z30O.

3.1.4 Analysis of Z15M Samples

According to the optical microscopy images, *figure 37*, inside the printed materials track gaps, air gaps and voids are present. Printing tracks are not even throughout the entire cross-section. The distribution of the short glass fiber changes near the printing tracks gap, air gaps, and edges of the tracks. The presence of short glass fibers is also less.

The OPD images indicate to have very less bonding between the tracks. This may greatly impact tensile testing. However, the number of voids or air gaps is fewer. In case of Z15M materials both conduction and convection heating strategies are maintained, which may lead to the removal of the voids. The TPD picture provides clear idea about the angle between fibers and the surface variation and parts of the fiber may not be visible but continuing into the polymer inside the entire cross-section, uneven material deposition during printing, and significantly poor bonding between the tracks (upwards). Such poor bonding may have influence on the delamination of the material during the tensile testing. Because of under and over deposition of the material during printing the direction of the glass fibers does not always follow the parallel path towards the printing direction.

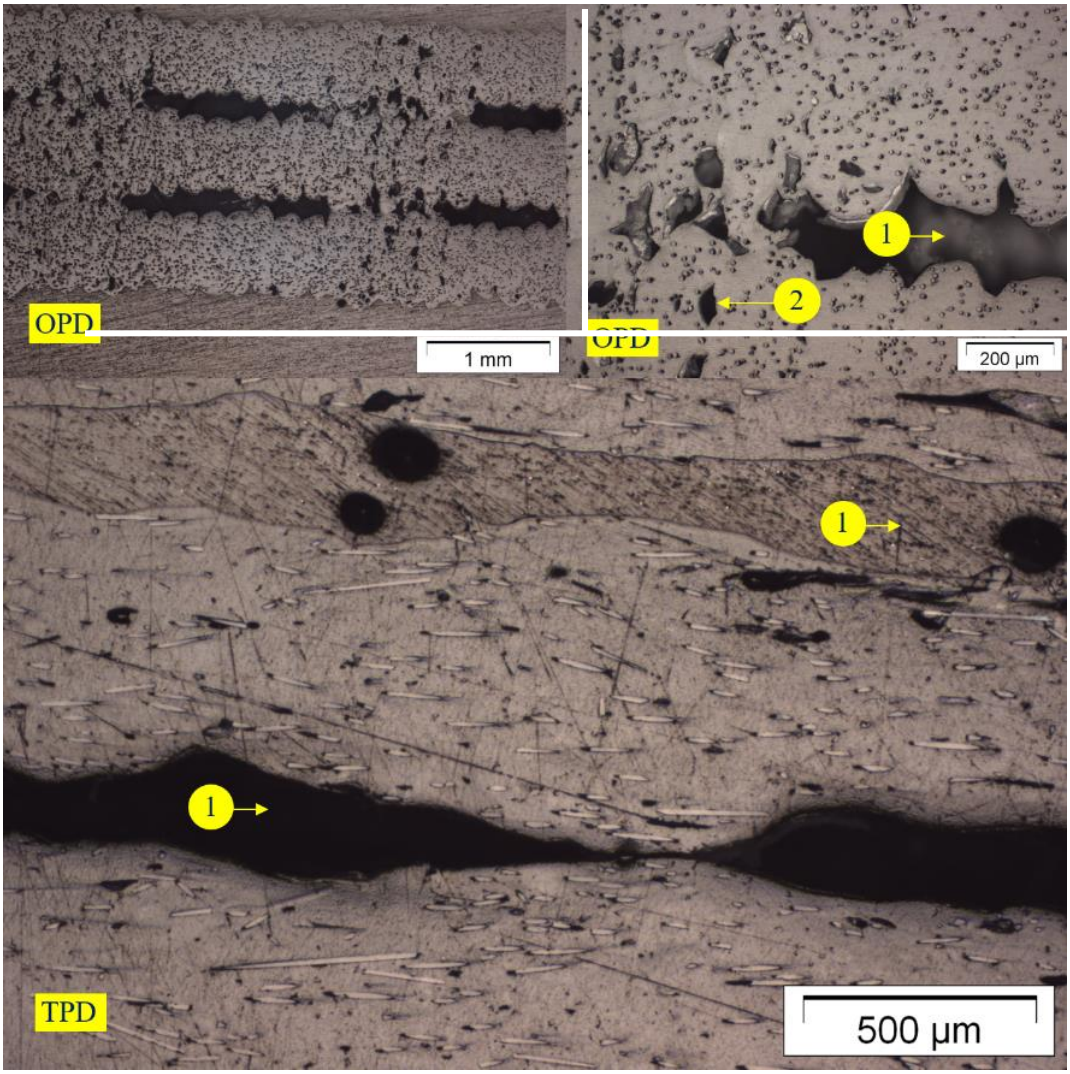

Fig 37. *Optical microscopy images of* Z15M*:* (1) *gap between the tracks,* (2) *air gap.*

3.1.5 Analysis of Z15MHT Samples

The Z15MHT has a combination of slower speed with conduction and convection heating strategies during the printing process. The optical microscopy images of *figure 38* represent that because of slower printing speed tracks have been dried out before forming a bond with the neighboring layers, resulting significant gaps between the tracks. The presence of both conduction and convection heating facilitates to remove the voids or air gaps inside the already deposited material.

The TPD pictures suggest material inside single tracks possess fewer voids, as Z15MHT has different heating techniques, it was according to the expectation. The gaps between the tracks are wider and very prominent, which was also expected because of slow printing speed and feeding rate. Moreover, the presence of short glass fibers is less as it has 15% fiber weight fraction. The distribution of the short glass fiber is not always exactly parallel to the materials deposition direction, the randomization happens to the over, under deposition area and where the voids are present.

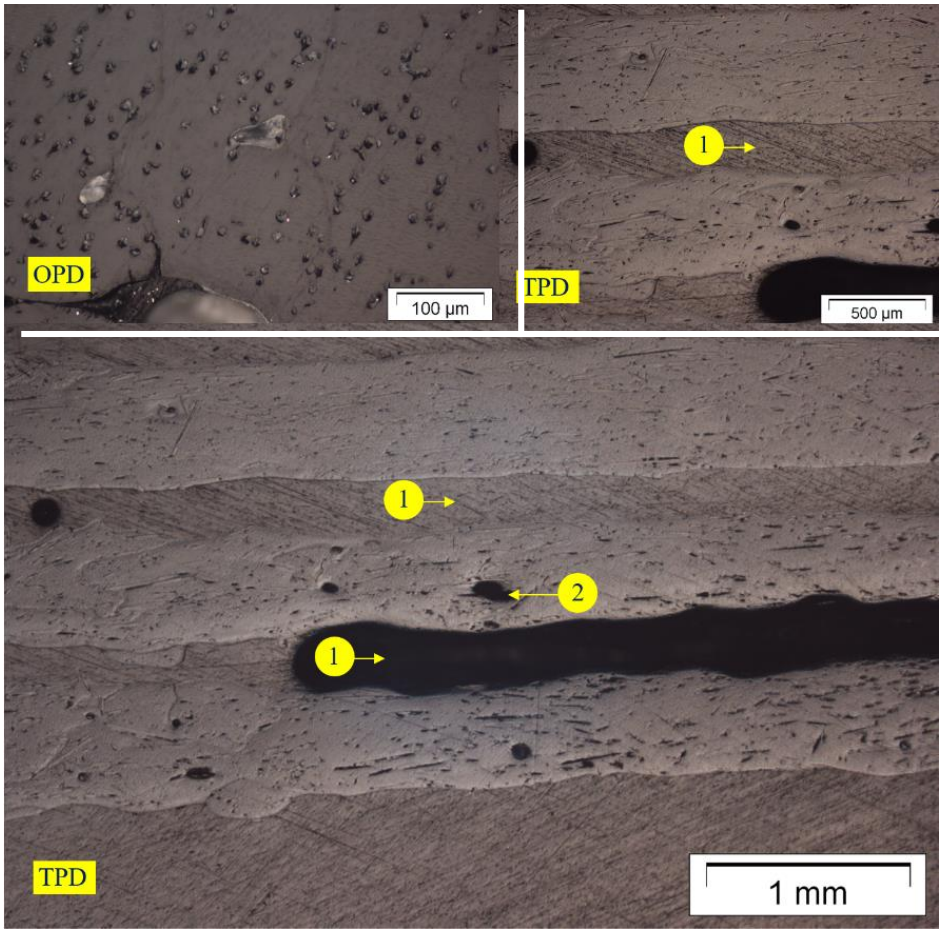

Fig 38. *Optical microscopy images of* Z15MHT*:* (1) *gap between the tracks,* (2) *air gap.*

3.1.6 Analysis of Z15O Samples

The optical microscopy images, *figure 39*, of Z15O samples, are quite different than their counterparts, but look similar to the Z30O. The interlayers bonding is very poor because of weak adhesion between the tracks as well as the presence of voids between the tracks. Since Z15O has no special heating strategies or convection heating system, it was expected to have more voids inside the printed material. The OPD views revel only idea about the interlayers bonding, at the same time TPD shows evidence of the presence of larger voids and weak adhesion inside the material which may definitely impact the mechanical performance. The orientation or distribution of the short glass fibers is interrupted mostly because of the bigger voids. The length of the short glass fibers is also not remained equal always.

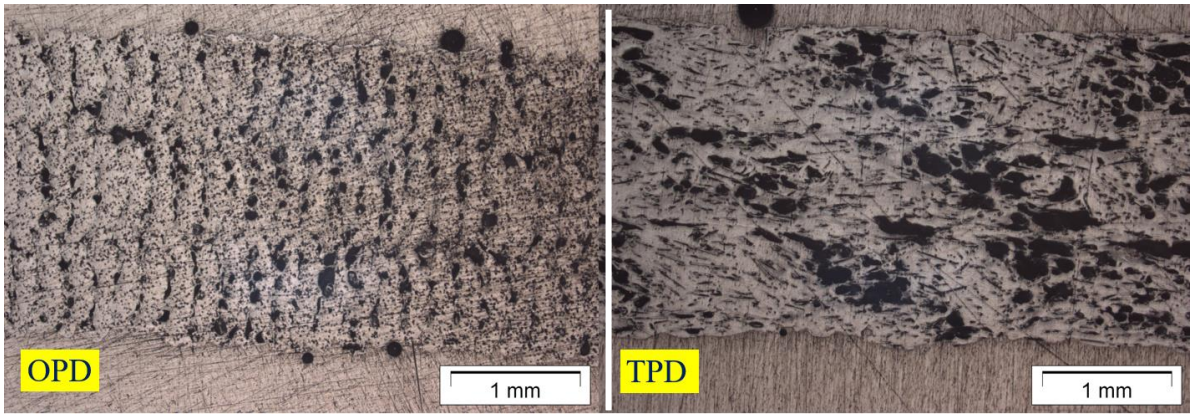

Fig 39. *Optical microscopy images of* Z15O*:* (1) *gap between the tracks,* (2) *air gap.*

3.1.7 Analysis of Y directional (0^o) Samples

To the Y directional samples, *figure 40*, the short glass fibers are distributed along the tensile test direction, the presence of glass fiber would have a direct impact on mechanical performance. This is the reason why TPD pictures are most important for the Y directional or 0^o degree raster oriented samples.

The microscopy pictures of Y30M and Y15M present that the printing tracks width is not even because of under and over deposition of the material during printing. This may lead to uneven high performance throughout the entire cross-section area of the printed parts. Inside the individual tracks, notably bigger voids are present, which may also act as a weak zone during tensile testing. At the same time, glass fibers are not hundred percent parallel oriented towards the printing melt flow or direction of the printing tracks. This may also reduce the possibility of mechanical performance. The gaps between the tracks are also very prominent, which may lead to the delamination of the printed parts under load acting perpendicular to the glass fiber's direction. Theoretically the short glass fibers length should look even throughout the entire cross-section, in reality, the optical microscopy images tell different things- the angle between fibers and the surface are varying and parts of the fiber may not be visible but continuing into the polymer matrix.

On the other hand, the optical microscopy pictures of Y30O and Y15O indicate that inside the cross-section of the material there are lot more voids are present. This would potentially impact on the mechanical performance of the printed parts. The direction of the short glass fibers also hampered not only because of the under or over deposition of the material but also for the presence of larger voids inside the individual printing tracks. This would also influence on mechanical performance.

To compare between Y30M and Y30O or Y15M and Y15O, the individual printing tracks of Y30M are better because of fewer voids. There is only one parameter that is different, the heating strategy- convection heating presents in Y30M and helped to avoid voids. Between Y30M and Y15M or Y30O and Y15O, the weight fraction difference of the short glass fiber is also visible in the optical microscopy images.

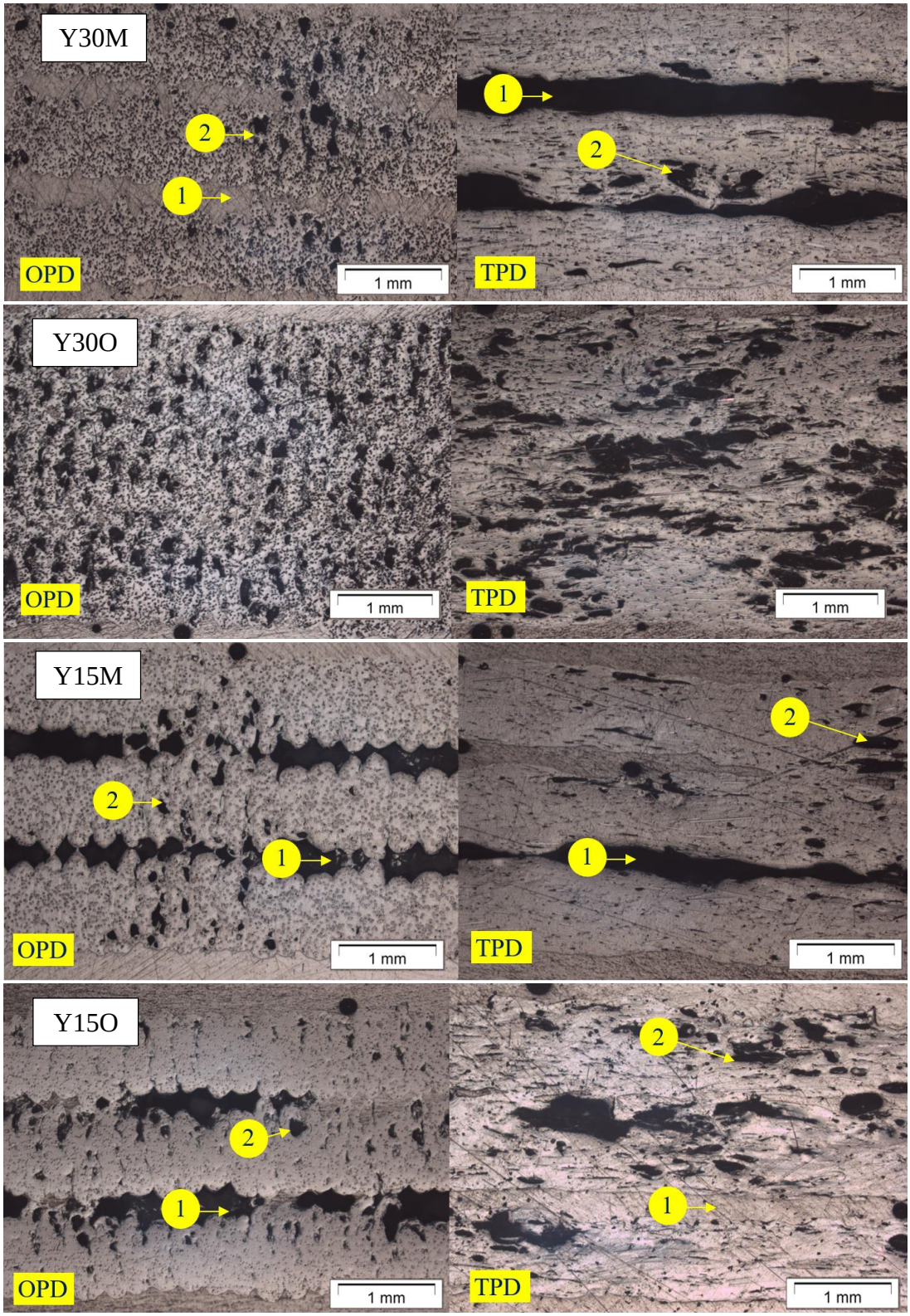

Fig 40. *Optical microscopy images of* Y directional samples*:*
(1) *gap between the tracks,* (2) *air gap.*

3.1.8 Comparison of Z (90^o) and Y (0^o) Samples

The optical microscopy images, *figure 41*, reveal the following information. All the Z oriented (90^o) samples have the short glass fiber not distributed to the lengthwise direction of the specimens. On the other hand, Y oriented (0^o) samples have the short glass fiber towards the length of the specimens. The glass fibers orientation may play a huge role in mechanical performance.

Among Z30M, Z30MHT, and Z30O: Z30MHT has a wider gap between the printing tracks. Z30M has a gap between the tracks too, it also has air gaps and voids inside the material. The amount of voids inside the material of Z30O sample is high. Among Z30M vs Z15M and Z30O vs Z15O: more voids are appearing for the more weight percentage of the short glass fiber. There may have connection with fiber percentage to the voids. The events also observed for Y30M vs Y15M and Y30O vs Y15O.

There is another event noticeable between Z and Y oriented samples. When there was only a conduction heating system, gaps between the tracks are difficult to differentiate from the air gaps and voids for Z oriented. At the same time, there are differentiable gaps between the tracks for Y oriented samples. From the nomenclature, *figure 20*, it is possible to say time of printing one track adjacent to the previous track was less for the Z and time was higher for Y. This could be the possible reason for this track gaps event. Because of this, Z sample was not able to solidify properly and connected with the adjacent tracks and formed voids. The gap between the tracks is the biggest for Z30MHT and Z15MHT. The printing speed was one fourth. As a result, material solidified before coming the next track.

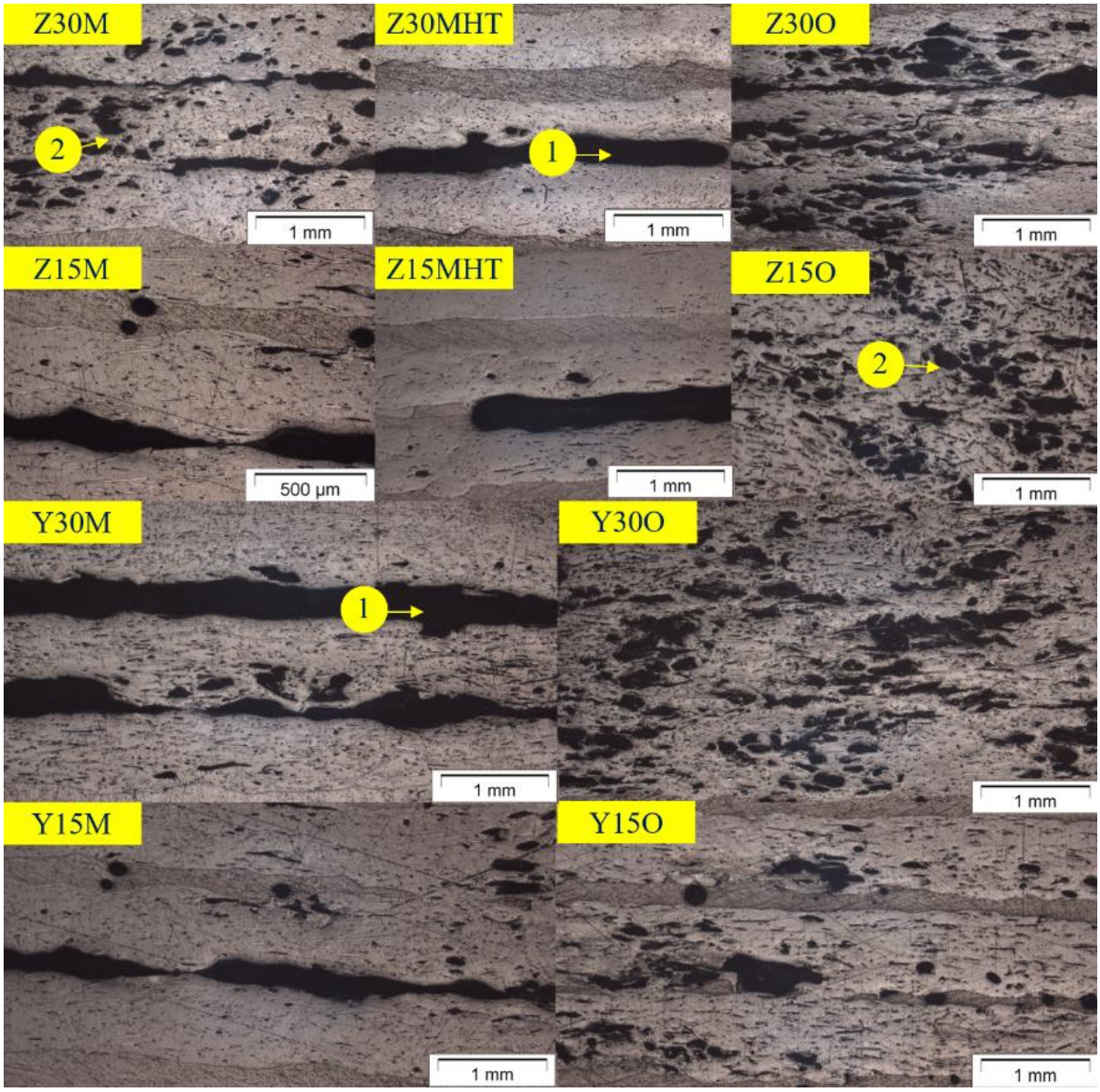

Fig 41. *Optical microscopy images of both Z and* Y directional samples*:*
(1) *gap between the tracks,* (2) *air gap.*

3.2 Density Measurement

The density measurement from the ten printed boxes is shown in *table 5* to *table 14*. The overall comparison among all the boxes is presented in *figure 41*. Regarding the position of the top, middle and bottom samples is already discussed in the *section 2.7.2*. The noticeable point is that the value of ethanol's density is changing with the change of atmospheric temperature.

Table 5. *Density of box* Y15M

Serial Mat.	Mass in Air, A (g)	Mass in Ethanol, B (g)	Density Ethanol, ρ_l (g/cm³)	Density Air, ρ_o (g/cm³)	**Density** $\rho = \frac{A}{A-B}(\rho_l - \rho_o) + \rho_o$ **(g/cm³)**	**Density (kg/m³)**	**Standard Deviation**
Top	0.402	0.125	0.78712	0.0012	**1.14**	**1142**	**1.7%**
Middle	0.366	0.114			**1.14**	**1143**	
Bottom	0.408	0.133			**1.17**	**1167**	

Table 6. *Density of box* Y30M

Serial Mat.	Mass in Air, A (g)	Mass in Ethanol, B (g)	Density Ethanol, ρ_l (g/cm³)	Density Air, ρ_o (g/cm³)	**Density** $\rho = \frac{A}{A-B}(\rho_l - \rho_o) + \rho_o$ **(g/cm³)**	**Density (kg/m³)**	**Standard Deviation**
Top	0.382	0.130	0.78712	0.0012	**1.19**	**1193**	**1.0%**
Middle	0.389	0.134			**1.20**	**1200**	
Bottom	0.283	0.095			**1.18**	**1185**	

Table 7. *Density of box* Y15O

Serial Mat.	Mass in Air, A (g)	Mass in Ethanol, B (g)	Density Ethanol, ρ_l (g/cm³)	Density Air, ρ_o (g/cm³)	**Density** $\rho = \frac{A}{A-B}(\rho_l - \rho_o) + \rho_o$ **(g/cm³)**	**Density (kg/m³)**	**Standard Deviation**
Top	0.790	0.257	0.78609	0.0012	**1.16**	**1165**	**1.2%**
Middle	0.856	0.267			**1.14**	**1142**	
Bottom	0.973	0.312			**1.16**	**1157**	

Table 8. *Density of box* Y30O

Serial Mat.	Mass in Air, A (g)	Mass in Ethanol, B (g)	Density Ethanol, ρ_l (g/cm³)	Density Air, ρ_o (g/cm³)	**Density** $\rho = \frac{A}{A-B}(\rho_l - \rho_o) + \rho_o$ **(g/cm³)**	**Density (kg/m³)**	**Standard Deviation**
Top	0.368	0.106	0.78712	0.0012	**1.11**	**1105**	**0.6%**
Middle	0.362	0.105			**1.11**	**1108**	
Bottom	0.375	0.106			**1.10**	**1097**	

Table 9. *Density of box* Z15M

Serial Mat.	Mass in Air, A (g)	Mass in Ethanol, B (g)	Density Ethanol, ρ_l (g/cm³)	Density Air, ρ_o (g/cm³)	**Density** $\rho = \frac{A}{A-B}(\rho_l - \rho_o) + \rho_o$ **(g/cm³)**	**Density (kg/m³)**	**Standard Deviation**
Top	0.479	0.131	0.78746	0.0012	**1.08**	**1083**	**1.0%**
Middle	0.468	0.133			**1.10**	**1100**	
Bottom	0.491	0.138			**1.09**	**1095**	

Table 10. *Density of box* Z15MHT

Serial Mat.	Mass in Air, A (g)	Mass in Ethanol, B (g)	Density Ethanol, ρ_l (g/cm³)	Density Air, ρ_o (g/cm³)	**Density** $\rho = \frac{A}{A-B}(\rho_l - \rho_o) + \rho_o$ **(g/cm³)**	**Density (kg/m³)**	**Standard Deviation**
Top	0.424	0.154	0.78712	0.0012	**1.24**	**1235**	**5.9%**
Middle	0.388	0.137			**1.22**	**1216**	
Bottom	0.449	0.136			**1.13**	**1129**	

Table 11. *Density of box* Z30M

Serial / Mat.	Mass in Air, A (g)	Mass in Ethanol, B (g)	Density Ethanol, ρ_l (g/cm³)	Density Air, ρ_o (g/cm³)	**Density** $\rho = \frac{A}{A-B}(\rho_l - \rho_o) + \rho_o$ **(g/cm³)**	**Density (kg/m³)**	**Standard Deviation**
Top	0.346	0.113	0.78729	0.0012	**1.17**	**1169**	**0.6%**
Middle	0.310	0.101			**1.17**	**1167**	
Bottom	0.471	0.156			**1.18**	**1177**	

Table 12. *Density of box* Z30MHT

Serial / Mat.	Mass in Air, A (g)	Mass in Ethanol, B (g)	Density Ethanol, ρ_l (g/cm³)	Density Air, ρ_o (g/cm³)	**Density** $\rho = \frac{A}{A-B}(\rho_l - \rho_o) + \rho_o$ **(g/cm³)**	**Density (kg/m³)**	**Standard Deviation**
Top	0.608	0.244	0.78746	0.0012	**1.31**	**1315**	**1.7%**
Middle	0.671	0.278			**1.34**	**1344**	
Bottom	0.574	0.230			**1.31**	**1313**	

Table 13. *Density of box* Z15O

Serial / Mat.	Mass in Air, A (g)	Mass in Ethanol, B (g)	Density Ethanol, ρ_l (g/cm³)	Density Air, ρ_o (g/cm³)	**Density** $\rho = \frac{A}{A-B}(\rho_l - \rho_o) + \rho_o$ **(g/cm³)**	**Density (kg/m³)**	**Standard Deviation**
Top	0.469	0.117	0.78746	0.0012	**1.05**	**1049**	**1.5%**
Middle	0.413	0.107			**1.06**	**1062**	
Bottom	0.441	0.120			**1.08**	**1081**	

Table 14. *Density of box* Z30O

Serial Mat.	Mass in Air, A (g)	Mass in Ethanol, B (g)	Density Ethanol, ρ_l (g/cm³)	Density Air, ρ_o (g/cm³)	**Density** $\rho = \frac{A}{A-B}(\rho_l - \rho_o) + \rho_o$ **(g/cm³)**	**Density (kg/m³)**	**Standard Deviation**
Top	0.545	0.155	0.78729	0.0012	**1.10**	**1100**	**0**
Middle	0.583	0.165			**1.10**	**1098**	
Bottom	0.440	0.125			**1.10**	**1099**	

3.2.1 Density Comparison

The density analysis, *figure 42*, shows the mass of a unit volume inside the matrix of the printed boxes. There are three types of porosity presents inside the printed material, gas bubble, interbead voids and holes are generated by the pulled out fibers, already discussed in the *section 1.2.4*.

The theoretical density of polyamide 6 is 1.31g/cm^3 whereas the printed boxes density is lower than this value. This potentially may indicate to have the presence of gas bubble produced during the fabrication of the feedback filament by extrusion and interbead voids generated by the voids between different layers.

The experiment values reveal the following results. The density of 90^o oriented (all the Z) fiber directional samples is higher than 0^o oriented (all the Y) fiber directional samples. The density alters mainly pressure and the temperature inside the polymer matrix. It also has connection to the fiber deposition amount, porosity, air gap.

Heating techniques also have influence. For example, between Z30M (conduction and convection heating) and Z30O (conduction heating) Z30M possesses higher density. The combined conduction and convection heating with higher temperature, Z30MHT, and Z15MHT, possess the highest density of all the samples. Also, the deviation among top, middle and bottom parts of samples are noticeable here. It may have connection with the homogeneity and amount of fibers inside matrix of the printed samples. In comparison with fiber percentage, between Z30M and Z15M, the Z15M possesses lower density than Z30M. On the other hand Z30O and Z15O have almost equal density measurement. It also suggests the connection of heating strategy.

The Z15M and Z150 have nearly the same density. Also, Y15M and Y15O have the same density. At the same time, Z30M and Z30O have density differences. The same thing also for Y30M and Y30O. Which suggests it may have connection with fiber percentage. Higher the fiber percentage more the density difference.

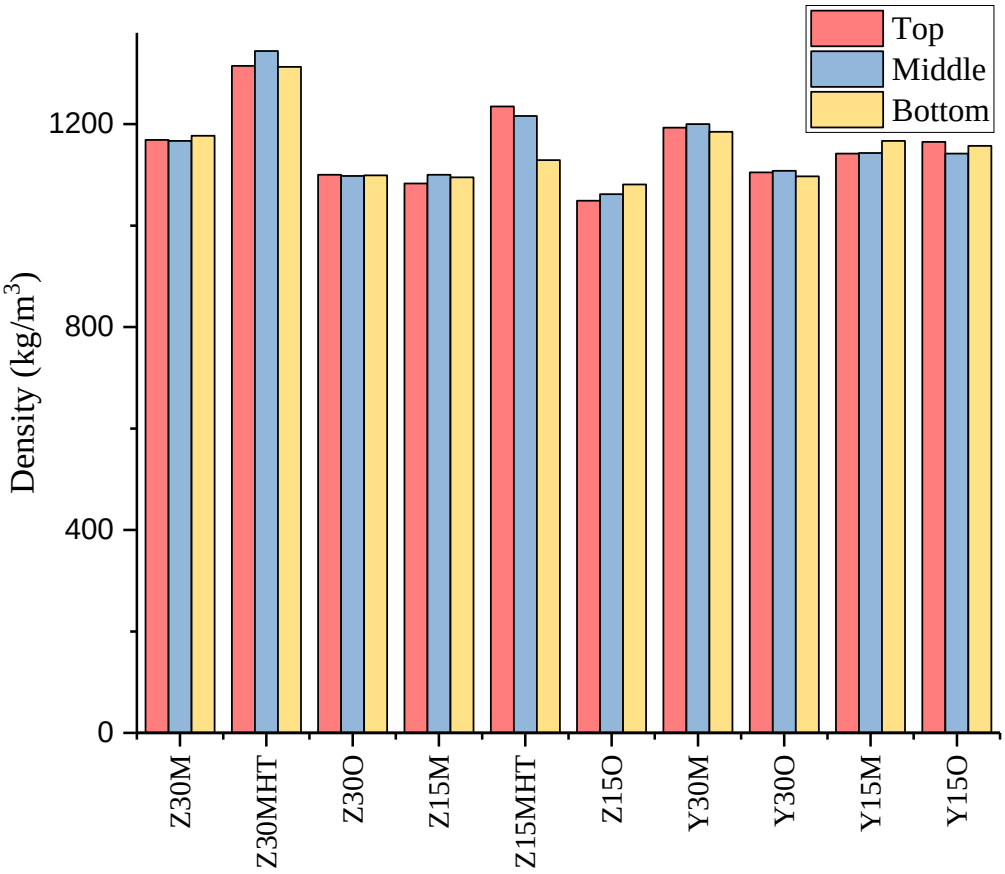

Fig 42. *Density analysis of printed boxes.*

3.3 Analysis of Tensile Test Result

The milled tensile test specimens were subjected to tensile loads until fracture point using a universal testing machine and recorded by different sensors. The stress vs strain curves were plotted in origin using those values. Example diagrams can be seen in *figure 43* to *figure 52*. The detailed analysis is discussed in *section 3.3.1* to *3.3.6*.

One thing is important to mention, overall ten boxes were printed before cutting as test specimens. The target was to cut six test specimens from the six different positions of the individual boxes. There were only three test specimens possible to cut out from the Z15O box. In case of box Z15MHT the test specimen number #2 was broken before mounting in the tensile testing machine and slippage during the testing occurred for test specimen #5 and #6. At the same time, in box Z30MHT the test specimen #6 was broken before tensile testing and slippage occurred for the test specimen #1 and #4. Because of this reason these test specimens were excluded from the detailed analysis of tensile testing results.

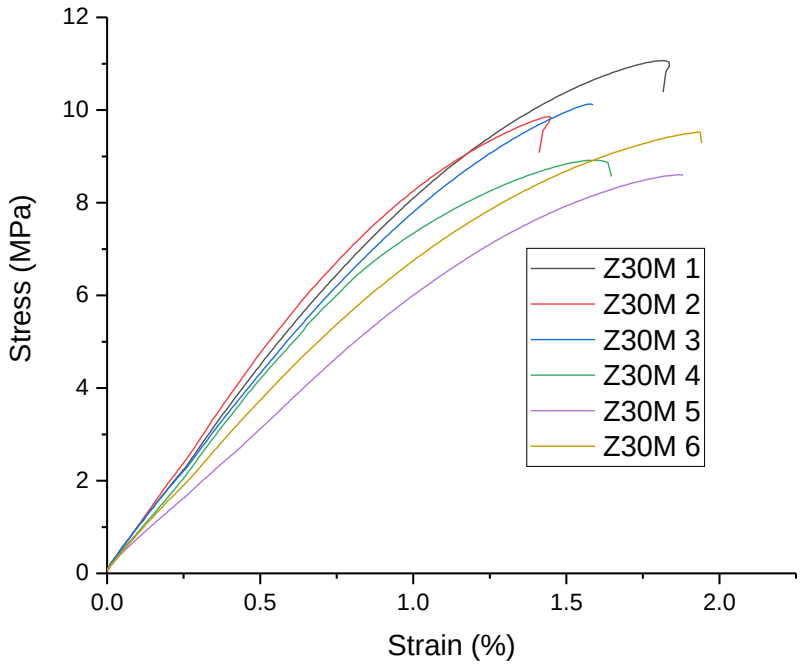

Fig 43. *Stress-strain curve for the* Z30M *specimens.*

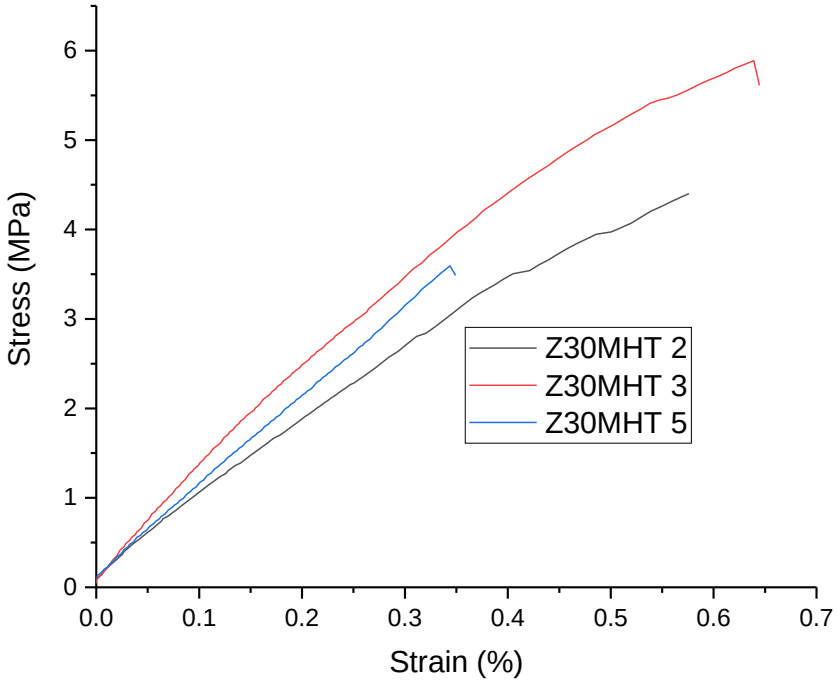

Fig 44. *Stress-strain curve for the* Z30MHT *specimens.*

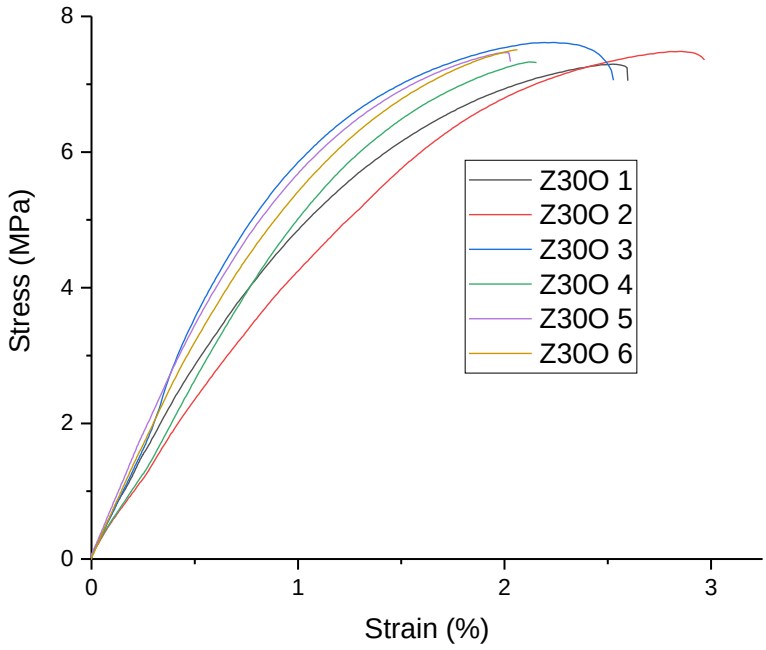

Fig 45. *Stress-strain curve for the* Z30O *specimens.*

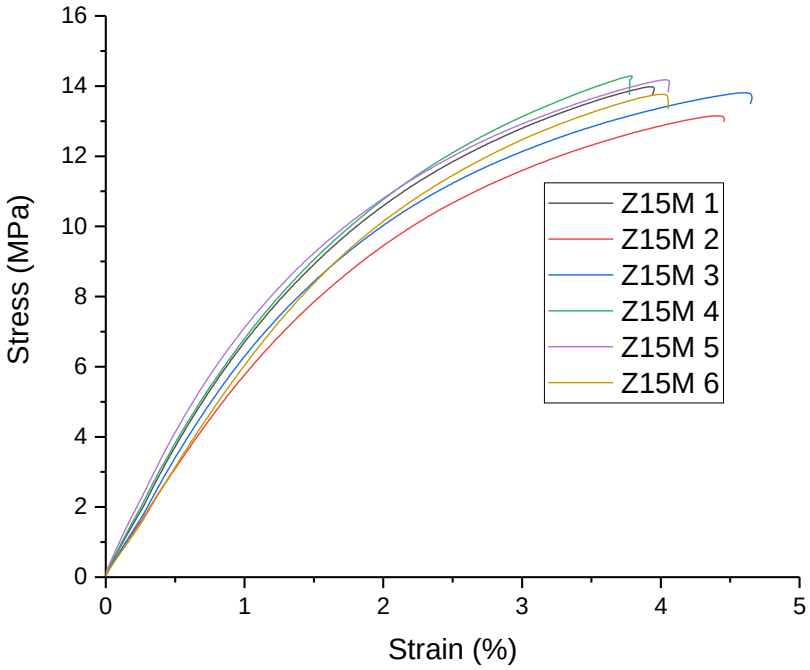

Fig 46. *Stress-strain curve for the* Z15M *specimens.*

The stress-strain curve is bit different for the Z15MHT. All of the three specimens break within the elastic region without showing less tendency to display plastic behavior after the yield point. This is probably because of the poor bonding between the layers inside the printed materials. The stiffness of Z15MHT #4 is nearly two times higher than Z15MHT #1. Both of them should be nearly equal distance from the printing bed. Although glass fiber should have no impact on the mechanical performance of Z directional specimens, somehow some of the glass fiber oriented to the direction of the tensile test. The optical microscopy images from *section 3.1.5* also suggest the same thing, few glass fiber oriented towards the direction of the tensile test. As a result, Z15MHT #4 shows more glassy behavior as well as the stiffness.

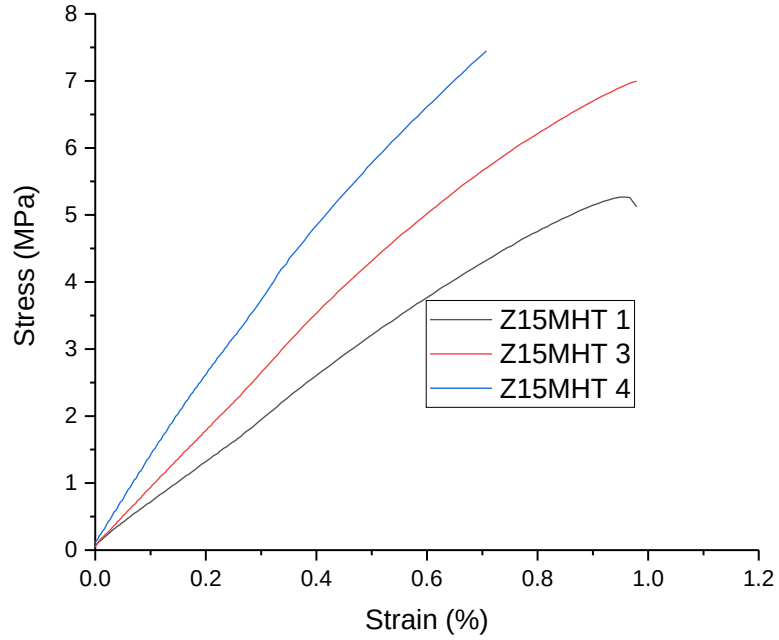

Fig 47. *Stress-strain curve for the* Z15MHT *specimens.*

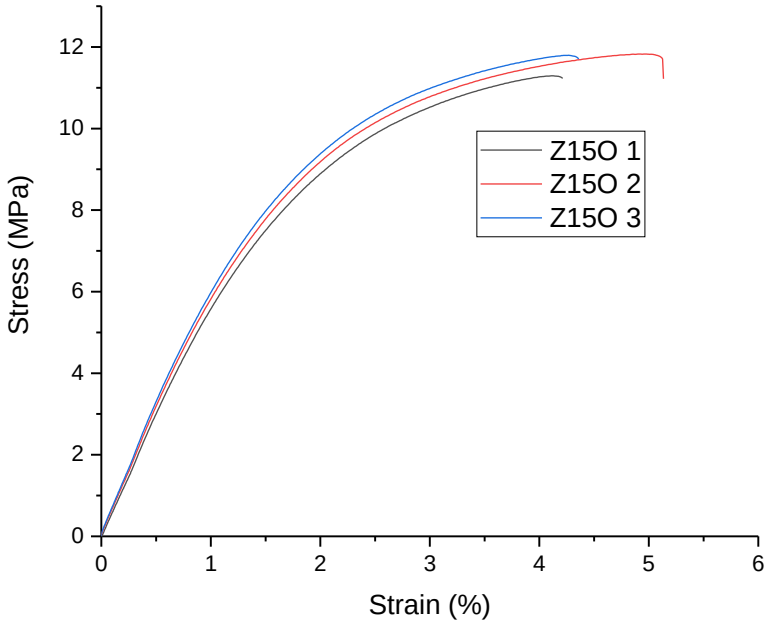

Fig 48. *Stress-strain curve for the* Z15O *specimens.*

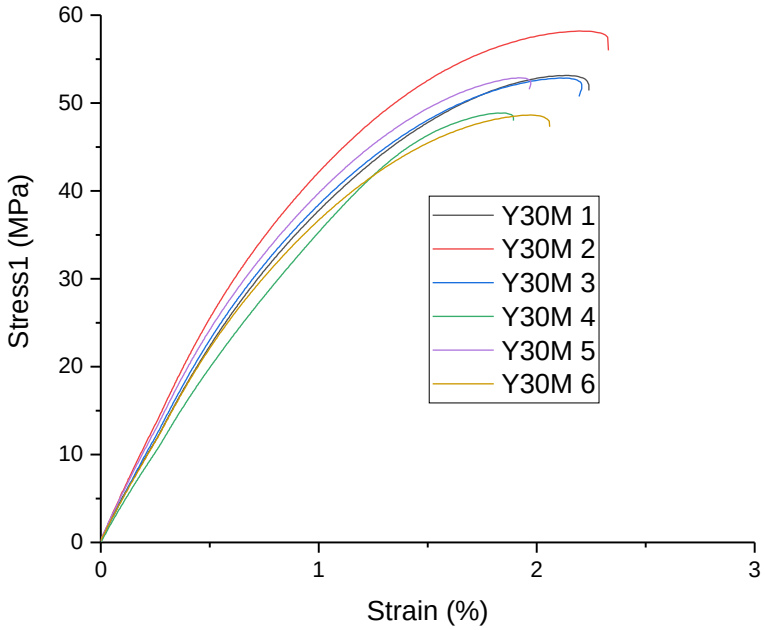

Fig 49. *Stress-strain curve for the* Y30M *specimens.*

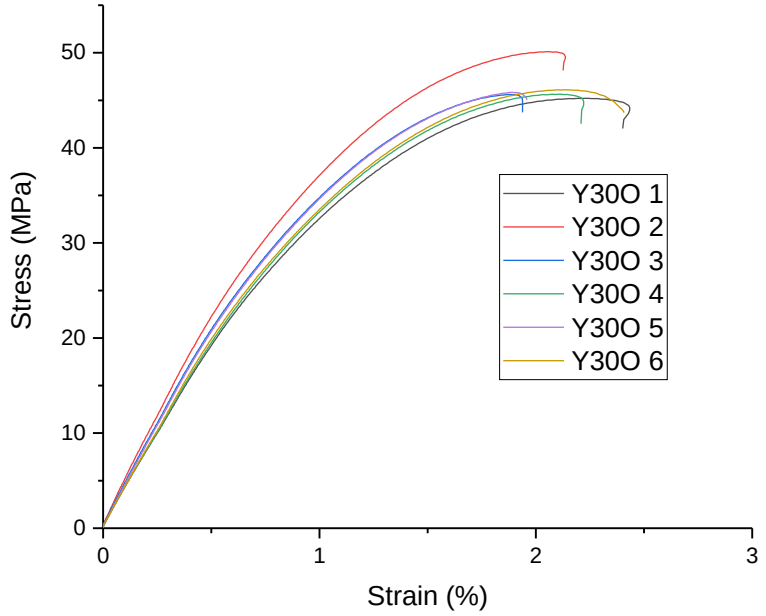

Fig 50. *Stress-strain curve for the* Y30O *specimens.*

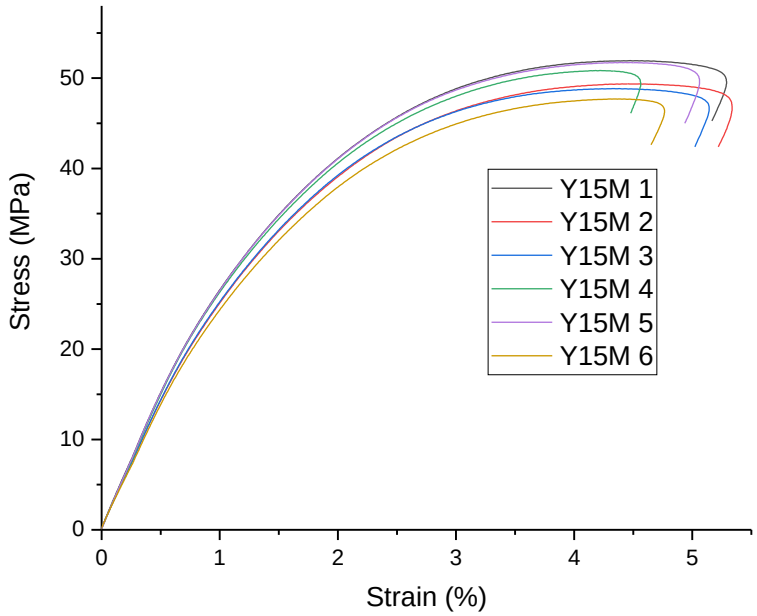

Fig 51. *Stress-strain curve for the* Y15M *specimens.*

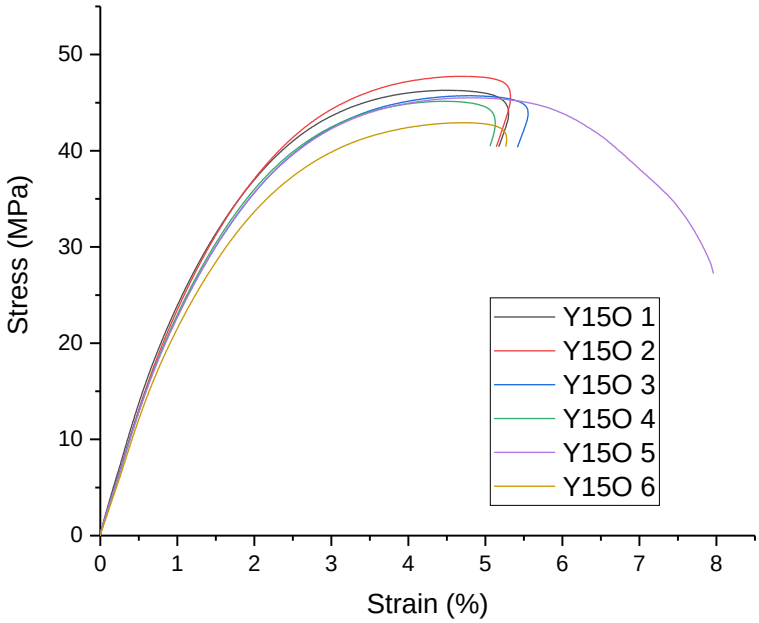

Fig 52. *Stress-strain curve for the* Y15O *specimens.*

3.3.1 Analysis of Z Oriented Specimens

F*igure 53* is representing the tensile strength of all the Z oriented specimens. It is clear from *section 2.2* that the short glass fibers of the Z oriented specimens are not distributed towards the tensile testing direction, hence tensile strength supposed to be lower than the Y. The maximum value is 13.86MPa from Z15M specimens and the lowest is 4.32MPa from Z30MHT specimens.

Among Z30M, Z30MHT and Z30O tensile strength is higher for Z30M and then Z30O. It is possible to relate to the optical microscopy images from *section 3.1.8*. Z30O has more voids than Z30M. Both Z30M and Z30O has the same printing speed, only the heating system is different. In other sense, heating strategy played a role here and heating of Z30M was better than Z30O. And Z30MHT has 1/4th of the printing speed. The previous track had got more time and solidified before the next track arrived. As a result, tracks were not bonded properly. The same trend of tensile strength is also found among Z15M, Z15O, and Z15MHT.

Interestingly with the increase of fiber weight fraction, tensile strength decreases in every case. The optical microscopy images from *section 3.1.7* suggested about voids inside the material and the 30% weight fraction samples have more voids than 15% fiber weight fraction. At the same time it can also be potentially relatable with the density and porosity. The density increases with the increase of fiber weight fraction percentage, *section 3.2.1* and the porosity also decreases with the increase of fiber weight fraction percentage, *section 3.4*.

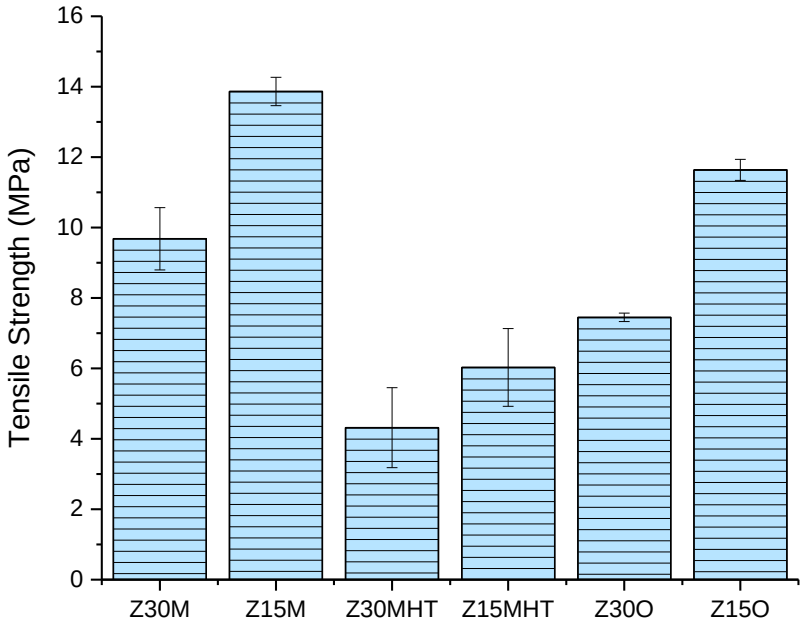

Fig 53. *Comparison of tensile strength* (MPa) *for Z-oriented specimens.*

3.3.2 Analysis of Y Oriented Specimens

F*igure 54* is representing the tensile strength of all the Y oriented specimens. The tensile strength was expecting to be higher since the short glass fiber oriented towards the lengthwise direction of the specimens. The Y30M has the highest tensile which is 52.42MPa and Y15O has the lowest tensile strength which is 45.55MPa.

Expectedly with the increase of fiber weight fraction the tensile strength increases. At the same time, the tensile strength of Y30M and Y30O are supposed to be the same. The optical microscopy images from *section 3.1.8* show Y30O has more voids because of its heating system. The same result is also found between Y15M and Y15O.

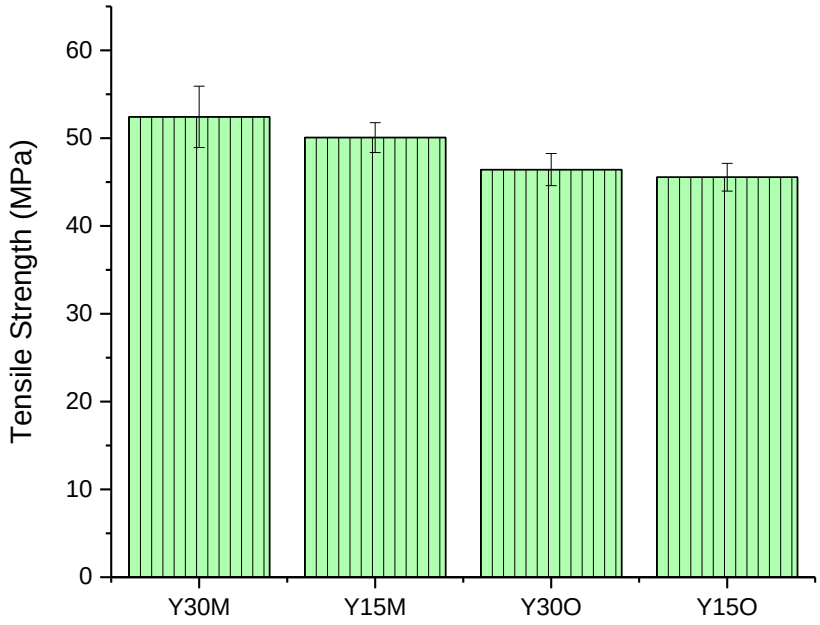

Fig 54. *Comparison of tensile strength* (MPa) *for* Y*-oriented specimens.*

3.3.3 Analysis of Z and Y Oriented Specimens with 30% and 15%

Expectedly tensile strength of Y oriented specimens is higher than Z oriented specimens as shown in *figure 55*. The standard deviation of tensile strength is firstly higher for Y oriented specimens. A closer look between Y30M and Y30O, Y30M has higher deviation. The optical microscopy images in *section 3.1.8* provide evidence of having fewer voids inside Y30M. It can be the reason for this deviation. The same kind of result appears for Y15M and Y15O.

The same explanation goes for *figure 55* also.

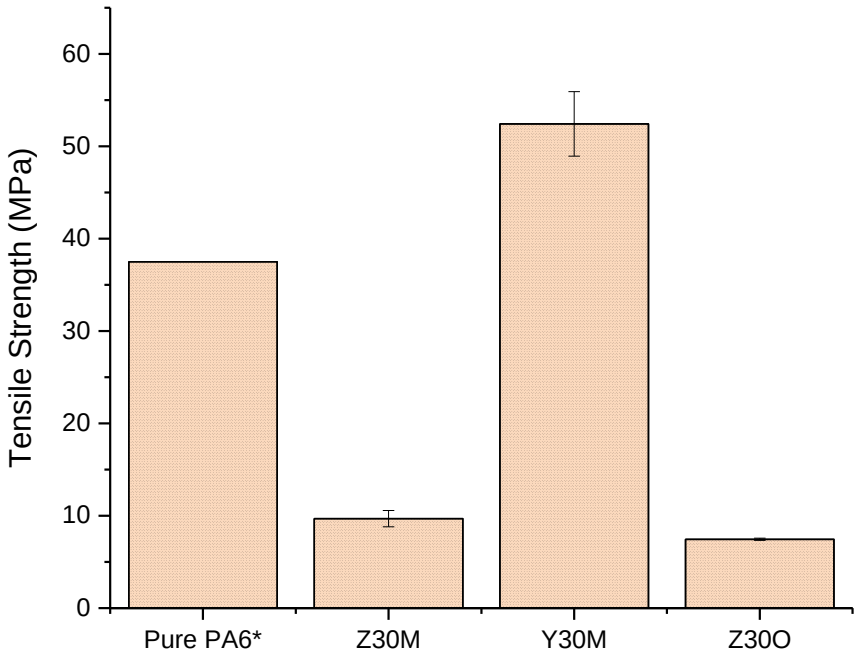

Fig 55. *Comparison between Z-oriented specimens and Y-oriented specimens with 30% fiber weight fraction* * [33].

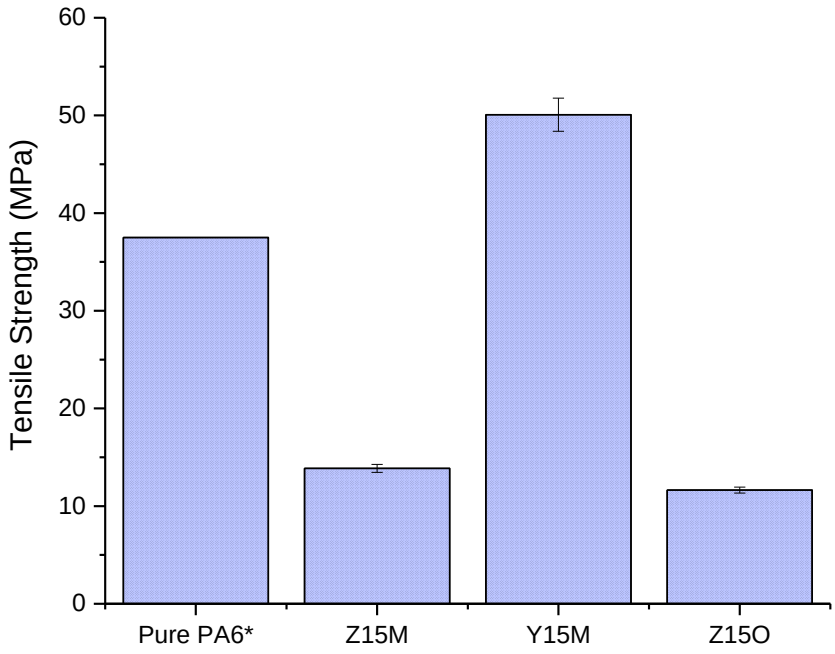

Fig 56. *Comparison between Z-oriented specimens and Y-oriented specimens with 15% fiber weight fraction* * [33].

3.3.4 Analysis of Strain at Break

The strain is also known as elongation at break, it expresses the capability of materials to resist changes of shape without crack formation. The comparison of strain for Y and Z oriented specimens is shown in *figure 57*. The strain decreases with the increase of fiber weight fraction and raster angles. In the Y direction strain reduces to half with the increase of fiber weight fraction from 15% to 30%. In the Z direction same phenomena are also observed, although there is no connection with glass fibers percentage.

In the Y direction the short glass fibers acting towards the direction of tensile test, the strain is supposed to be lower than the Z direction where it has no impact of glass fiber. The specimens with same fiber weight fraction Y15M and Z15M or Y15O and Z15O have almost same strain. According to *section 3.1.8* there can have connection with the printing track gaps and voids. To further extend it can be correlated with the density measurement from *section 3.2.1*. Since the average densities of Y15M, Z15M, Y15O, and Z15O are respectively about 1.15g/m^3, 1.09g/m^3, 1.15g/m^3, and 1.06g/m^3; the strain can be nearly same. With more fiber weight fractional specimens Y30M and Z30M or Y30O and Z30O same trend is also observed.

The deviation of strain for Y15O, Z15O, Z15MHT is higher, which can also be possible to relate with the density. For example, the Y150O has density 1.17g/m^3 at the top, 1.14g/m^3

in the middle and 1.15g/m^3 at the bottom. It reflects on the homogeneity of the material and the so on.

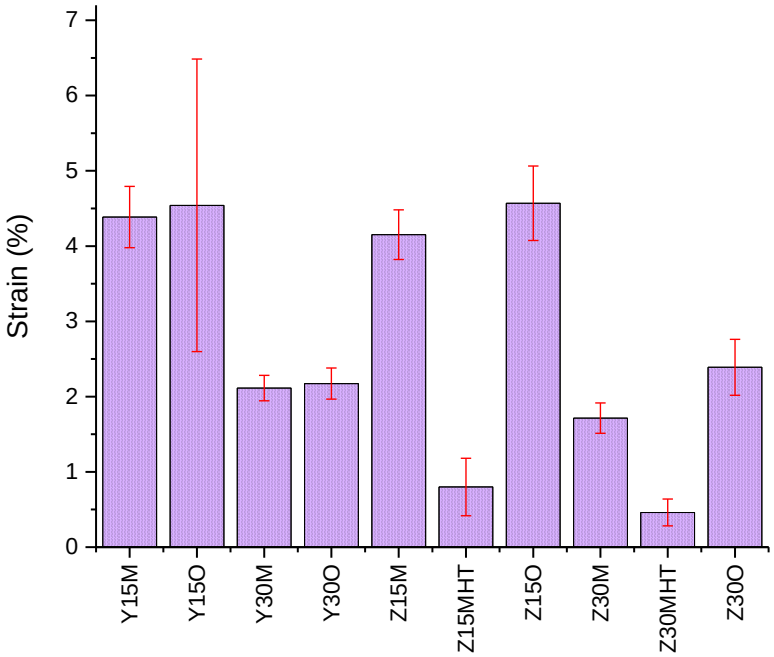

Fig 57. *Comparison of strain (in %) before fracture.*

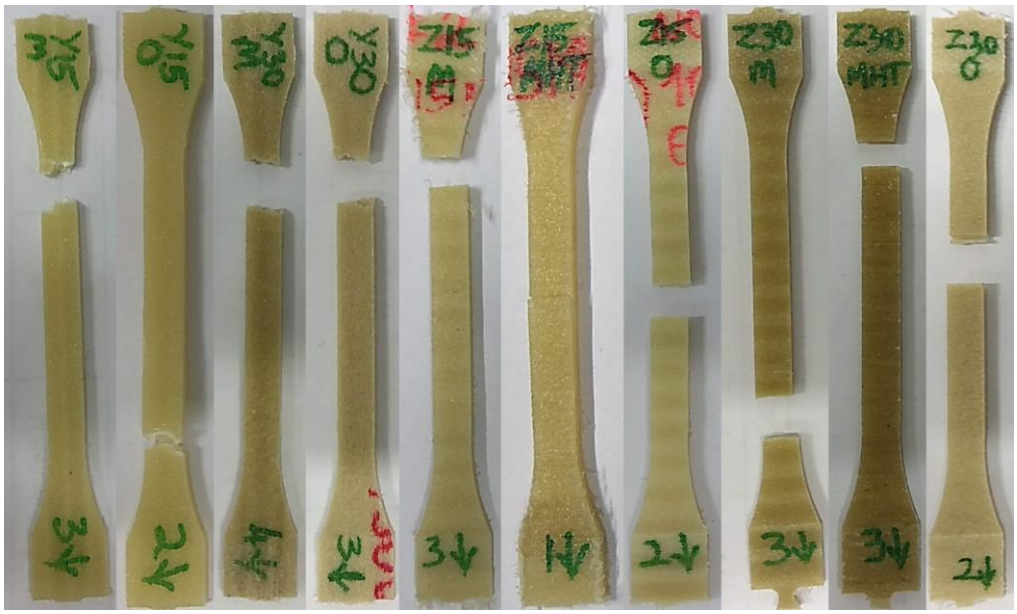

Fig 58. *Comparison of fracture surfaces after the tensile test.*

3.3.5 Analysis of Elastic Modulus

The elastic modulus of the printed specimens is shown in *figure 59*. The Y oriented specimens have higher elastic modulus than its counterparts Z oriented specimens. The Y specimens have the glass fibers predominantly oriented towards the direction of the tensile test direction. That means, it requires higher energy to deform. This is the reason why the increase of fiber weight fraction elastic modulus also increases significantly.

At the same time, Y30M and Y30O have the same printing speed and fiber weight fraction but have different elastic modulus. After comparing with the optical microscopy images from *section 3.1.8* it is possible to say Y30O contains more voids inside the materials. Hence Y30O has a lower elastic modulus than Y30M. The same thing goes with Y15M and Y15O.

The usual tendency of short glass fiber is to deposit towards the direction of the flow – from *section 2.2* – the flow of Z oriented specimens was opposite to the tensile test direction. This is the reason why the Z oriented specimens have no influence on the short glass fibers, fiber weight fraction has no role to the big shifting of the elastic modulus. According to the optical microscopy images from the *section 3.1.8* Z15O and Z30O have the highest voids, then Z30MHT and Z15MHT. Z30M and Z15M have the lowest voids inside the material. The same pattern reflects in the elastic modulus for these specimens.

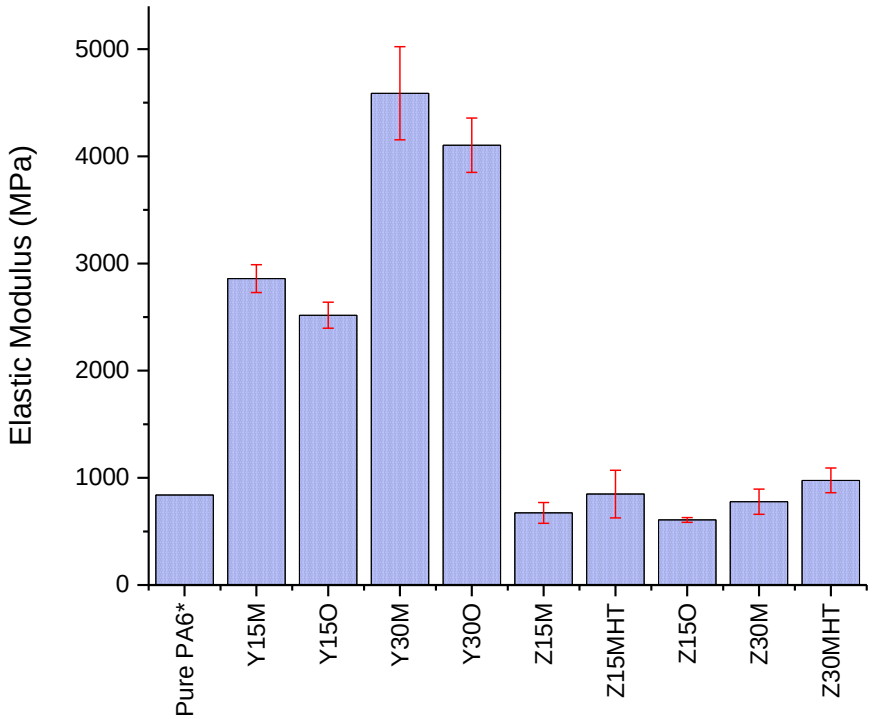

Fig 59. *Comparison of elastic modulus* (MPa) * [33].

3.3.6 Comparison of Printed Parts vs Injection Moulded

The Z directional specimens have an insignificant impact after reinforced with glass fiber in the tensile test, hence these specimens are omitted from the comparison. The tensile strength of injection moulded pure polyamide 6, in *figure 60*, is 37.3Mpa [33] and with the addition of 15% and 30% wt. glass fiber it goes respectively to 57.8MPa [34] and 70MPa [34]. The tensile strength of printed specimens is also increased with the increment of glass fiber weight fraction percentage. However, the tensile strength of printed specimens is still lower than the tensile strength of injection moulded specimens.

When the glass fiber weight fraction is 15%, the tensile strength of Y15O is approx. 25% less than injection moulded specimen, and Y15M is approx. 16% less than injection moluded specimen. It can potentially mean, the tensile strength has improved approx. 11% for the printed specimen after introducing a heating system consisting of both conduction & convection heating.

When the glass fiber weight fraction is 30%, the tensile strength of Y30O is approx. 36% less than injection moulded specimen and Y30O is approx. 26% less. The tensile strength has improved approx. 16% after introducing a heating system combined with both conduction & convection heating.

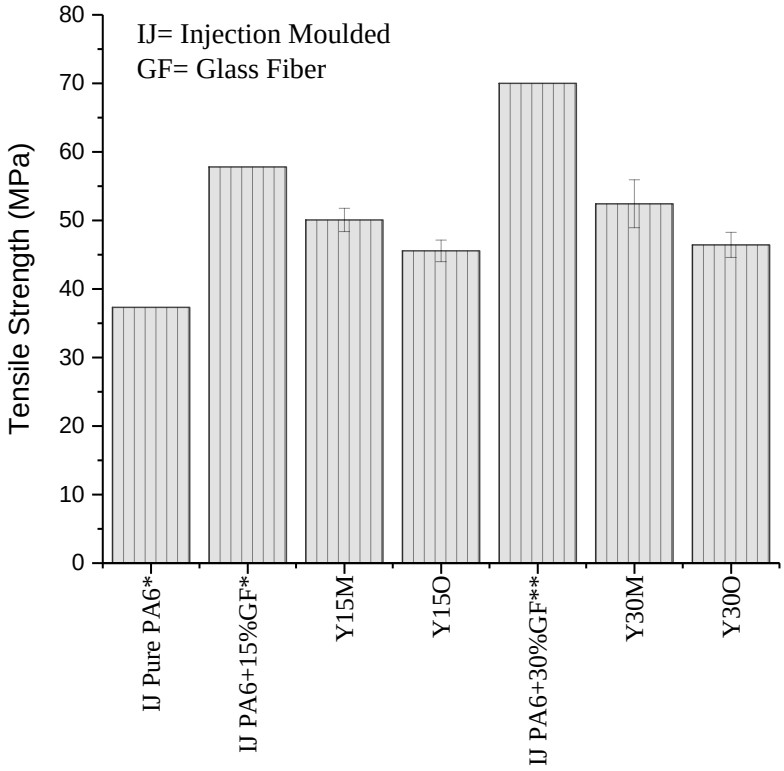

Fig 60. *Tensile strength* (MPa) *comparison between printed parts and injection moulded part* * [33] ** [34].

The elastic modulus of injection moulded pure polyamide 6, with 15% weight fraction of glass fiber, and with 30% weight fraction of glass fiber is respectively 840MPa [33], 2260MPa [34], and 7900MPa [34], which is shown in *figure 61*.

The elastic modulus increased more than double fold after the addition of a 15% weight fraction of glass fiber. The injection molulded specimen and printed specimens, Y15M and Y15O show elastic modulus nearly in the same range. However, printed specimens exhibit a bit higher elastic modulus than the injection moulded specimen.

The injection moulded specimen with 30% weight fraction of glass fiber shows nearly 8 times increased elastic modulus than the pure polyamide 6 specimens and 4 times higher elastic modulus than polyamide 6 with 15% weight fraction of glass fiber. At the same time, printed specimen shows 2 times the elastic modulus increment when the fiber weight fraction shifted to 30% from 15%.

This can gesture that the elastic modulus has a connection with glass fiber weight fraction and production process, i.e. injection moulded, printed specimen. As in both process, elastic modulus increased but not evenly, there may have a connection with glass fiber orientation.

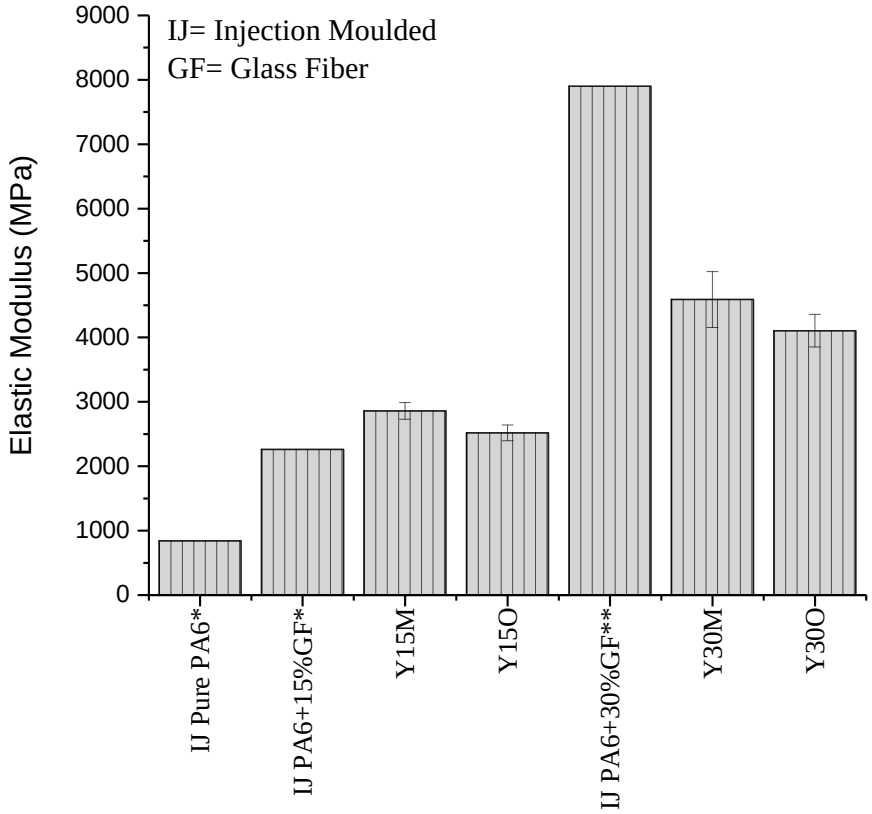

Fig 61. *Elastic modulus* (MPa) *comparison between printed parts and injection moulded part* * [33] ** [34].

3.4 Analysis of Porosity

The CT scanned images obtained from Rayscan 200E, in *figure 62*, were analyzed by VG studio software in *figure 63* and *figure 64*. Graphs of the porosity analysis are constructed using the average values.

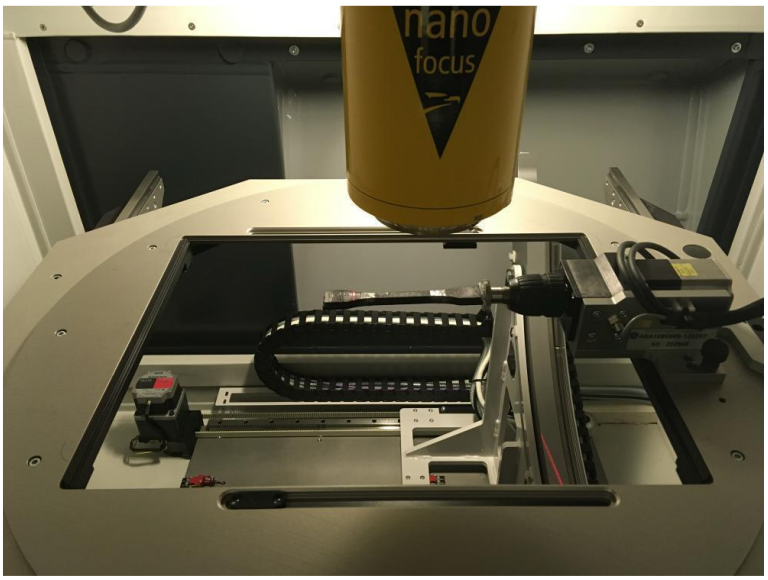

Fig 62. *CT scanning for porosity analysis.*

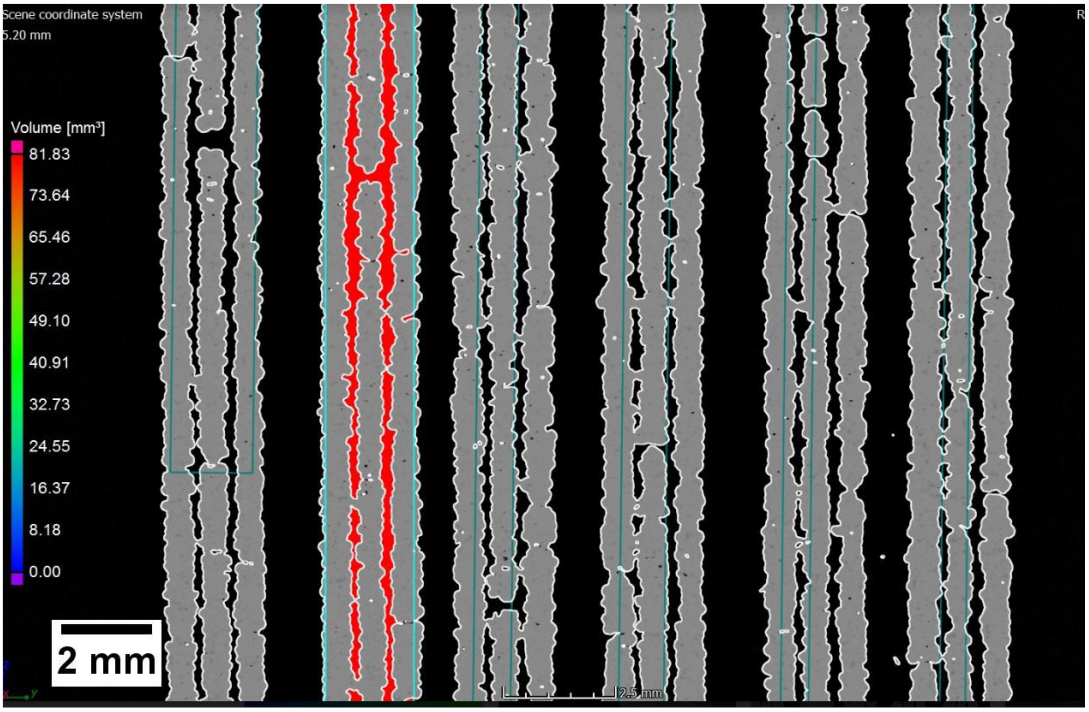

Fig 63. *Porosity analysis of Z15MHT samples, side view.*

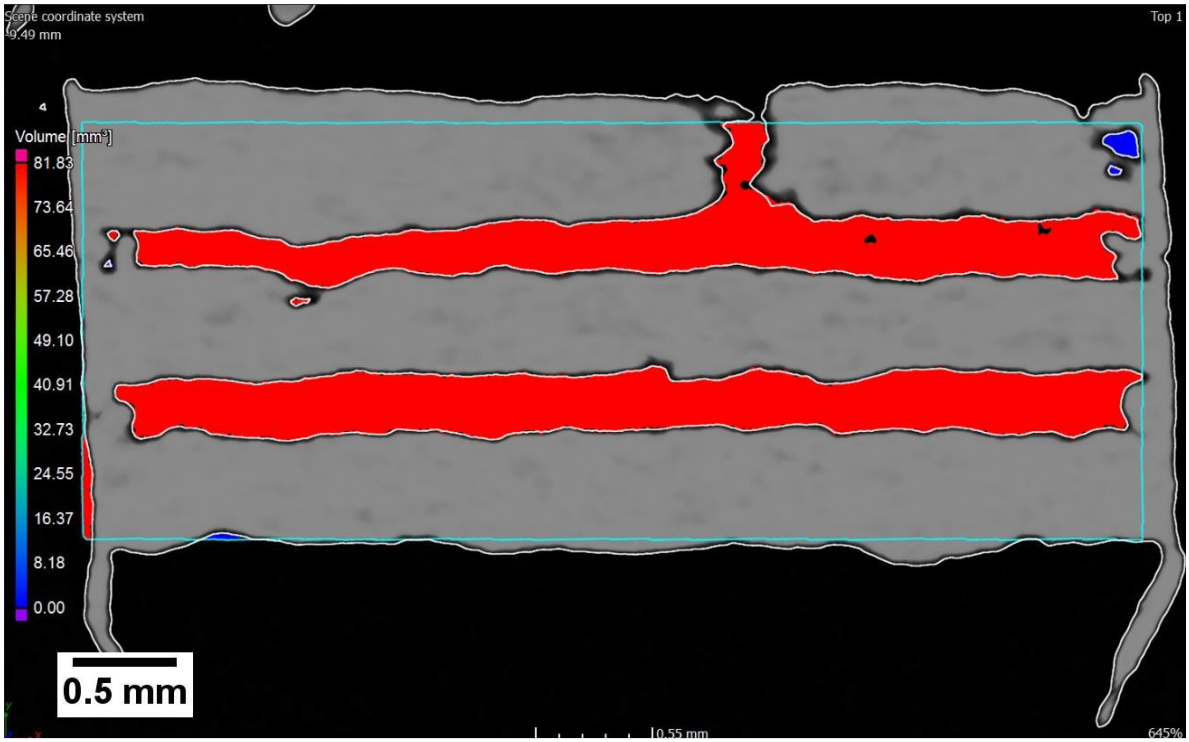

Fig 64. *Porosity analysis of Z15MHT samples, top view.*

The porosity of Z oriented and Y oriented specimens are specified respectively in *figure 65* and *figure 66*.

A relationship presents for Z oriented specimens: increase of fiber weight fraction increase the porosity. Among Z30M, Z30O, Z15M, and Z15O specimen Z30M have the highest porosity. Although Z30M and Z30O supposed to have around same porosity, there is a difference between their heating. It may arise from the heating system. The optical microscopy images from *section 3.1.8* suggest having bigger gaps between the tracks for Z30M. However, the relationship is not working, opposite for Z30MHT and Z15MHT. It may have connection with the printing speed. Because of lower printing speed the tracks solidified before the next one's arrival and formed bigger gaps between the tracks.

The linear relationship of porosity is opposite for Y oriented specimens: increase of fiber weight fraction decreases the porosity.

The cross-comparison with the counterparts with different fiber weight fraction is represented in *figure 67* and *figure 68*. Z30M has the highest porosity among 30% fiber weight fraction specimens and Y30O has the lowest. When the fiber weight fraction is 15%, Z15M has the lowest and Y15O has the highest porosity.

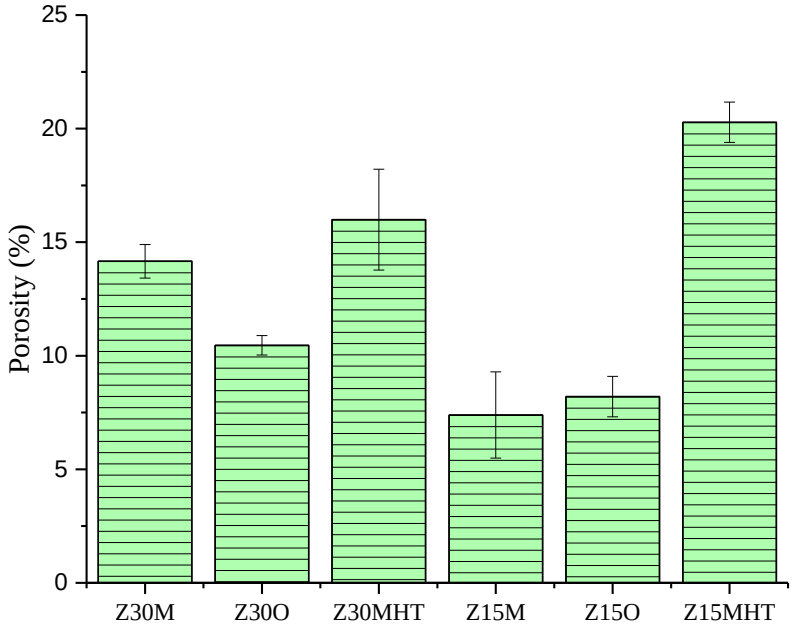

Fig 65. *Comparison of porosity (in %) of Z-oriented specimens.*

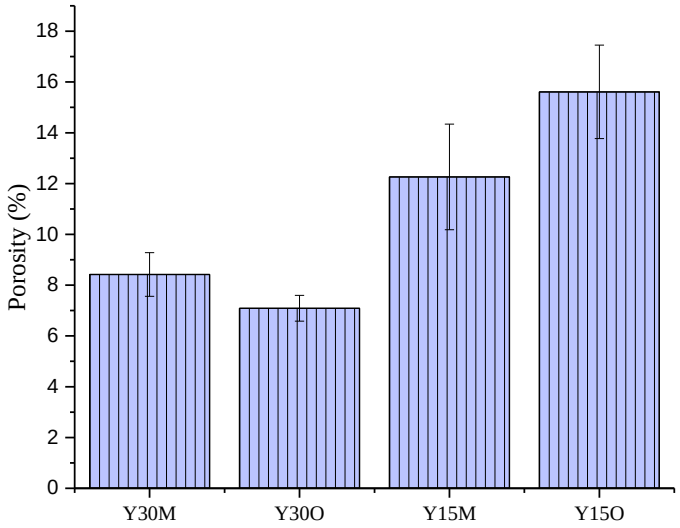

Fig 66. *Comparison of porosity (in %) of Y-oriented specimens.*

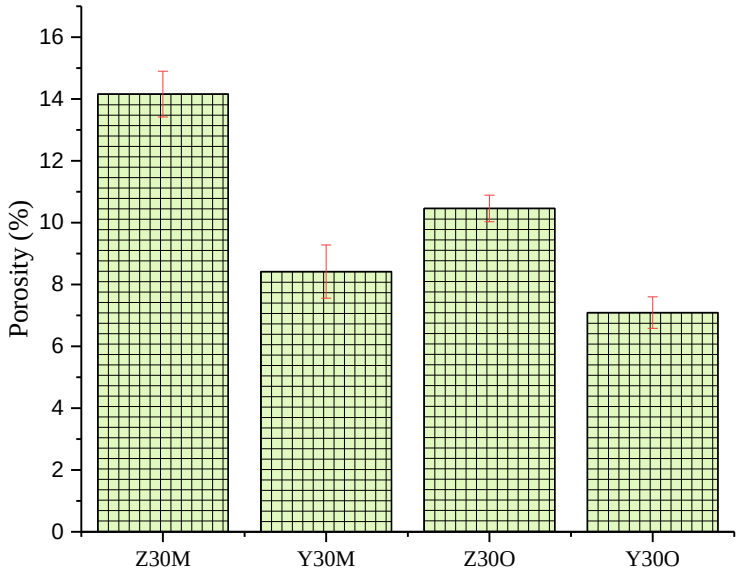

Fig 67. *Comparison between Z-oriented and Y-oriented specimens with 30% fiber weight fraction.*

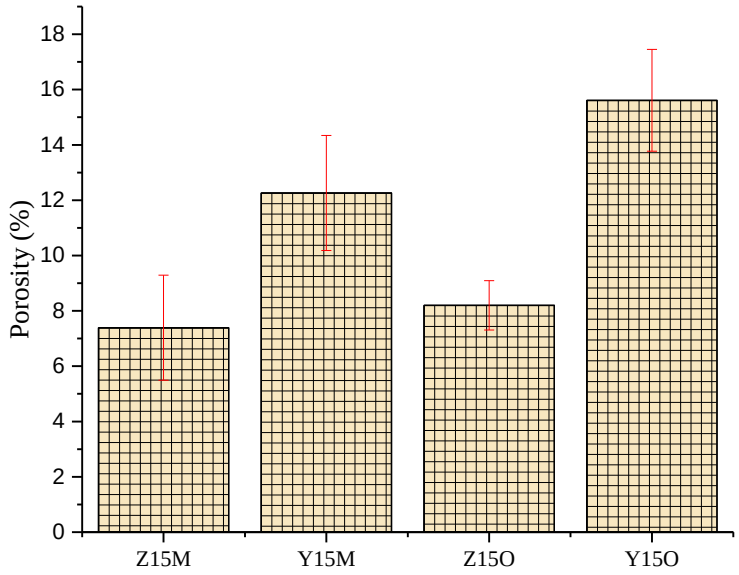

Fig 68. *Comparison between Z-oriented and Y-oriented specimens with 15% fiber weight fraction.*

3.5 Analysis of Fiber Orientation

The fiber orientation analysis was carried out in VG Studio software, in *figure 69*. The results obtained by analysis of the percentage of fibers and their respective angle of deviations with respect to the reference direction. And in this analysis, the direction of printing was selected as the reference direction.

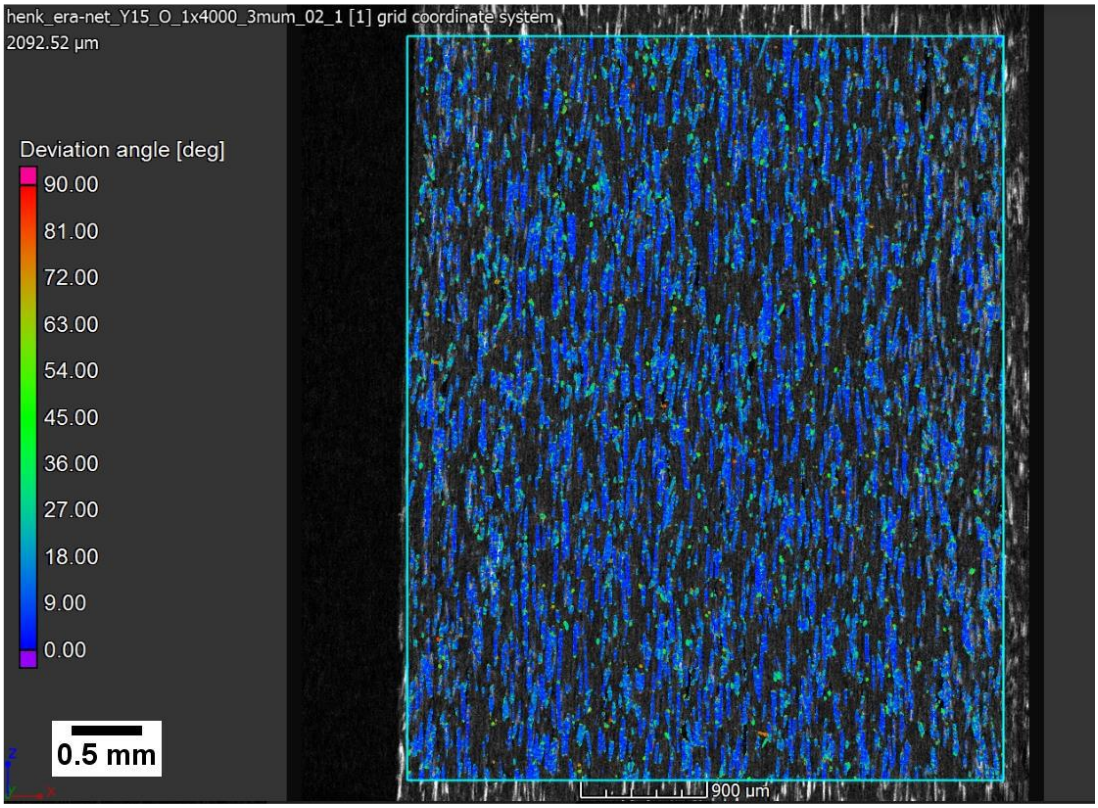

Fig 69. *Fiber orientation analysis of Y15O sample (front view).*

A general trend is observed for Z oriented specimens from the comparison of fiber orientation analysis in *figure 70.* The lower the fiber weight fraction, the lower the fiber orientation towards the printing direction. However, Z30MHT and Z15MHT have the highest amount of oriented fibers and not following the trend.

The general trend is opposite for the Y oriented specimens presented in *figure 71*. In this case, higher the fiber weight fraction, lower the amount of oriented fiber.

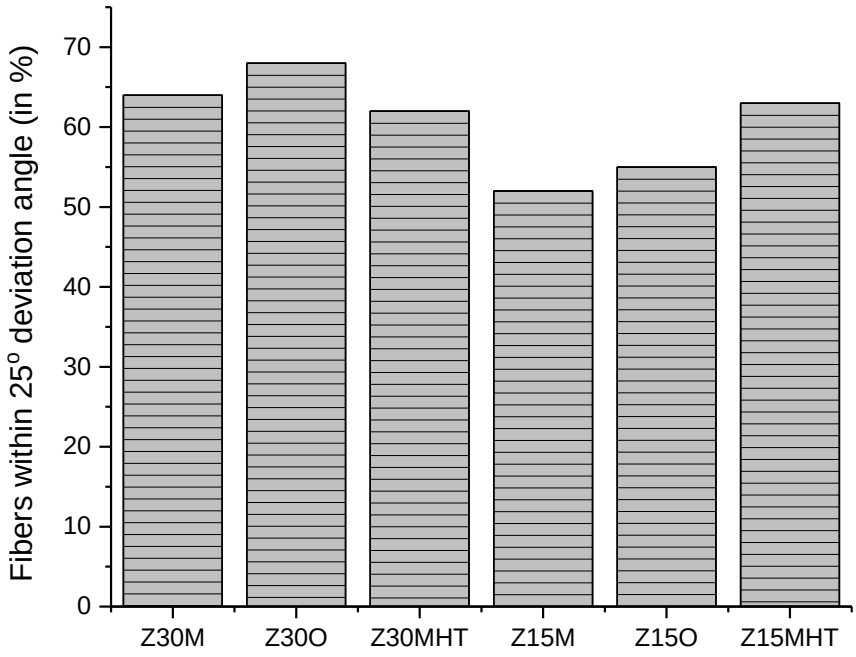

Fig 70. *Comparison of fiber orientation of Z-oriented specimens.*

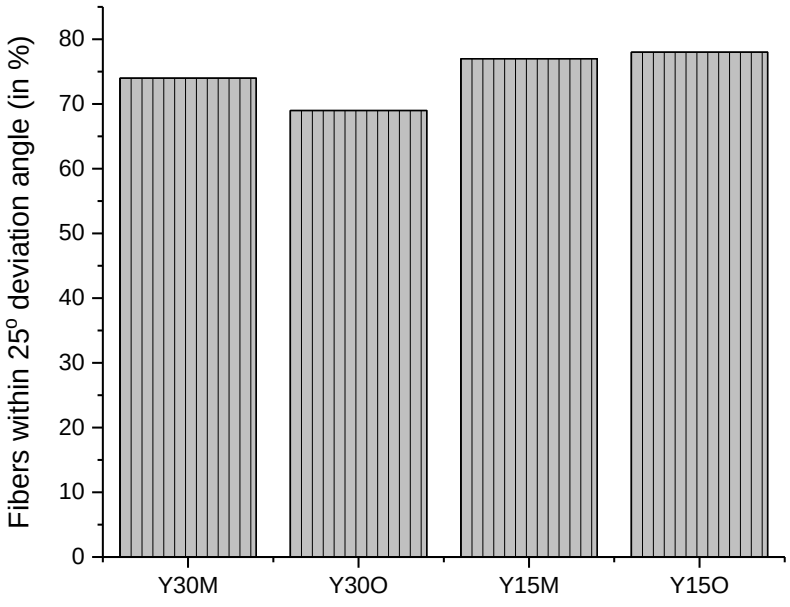

Fig 71. *Comparison of fiber orientation of Y-oriented specimens.*

The Y directional specimens have the highest percentage of oriented fiber towards the printing direction in both 15% fiber weight fraction and 30% fiber weight fraction presented in *figure 72* and *figure 73*.

At 30% fiber weight fraction in aspect with the percentage of fiber distribution the difference between Z and Y is not much as like as 15% fiber weight fraction.

Such difference could potentially come from the distance that the printer had to travel during printing towards Z and Y directions. To print Z directional specimen printer had to travel smaller distance than Y. Hypothetically fibers would be distributed towards the flow direction. Smaller distance means smaller areas with respect to flow direction and chance of fiber orientation is less.

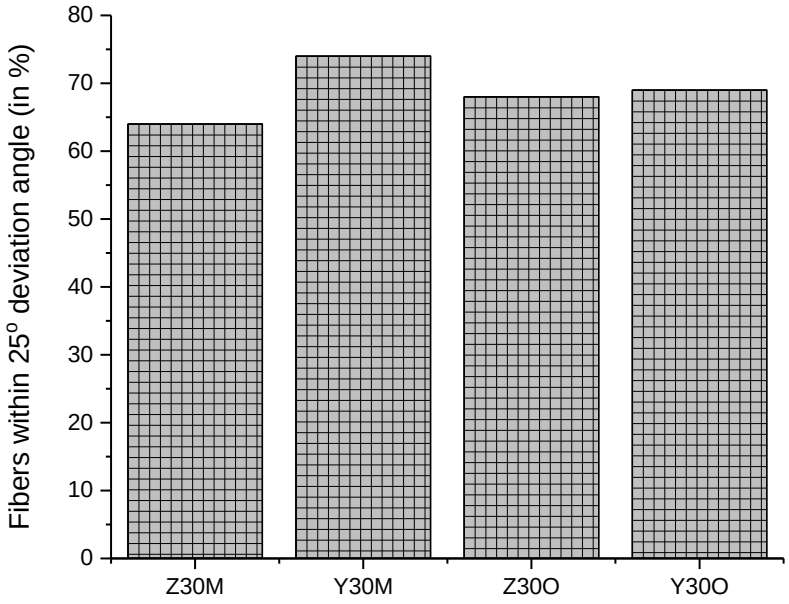

Fig 72. *Comparison of fiber orientation between Z-oriented and Y-oriented specimens with 30% fiber weight fraction.*

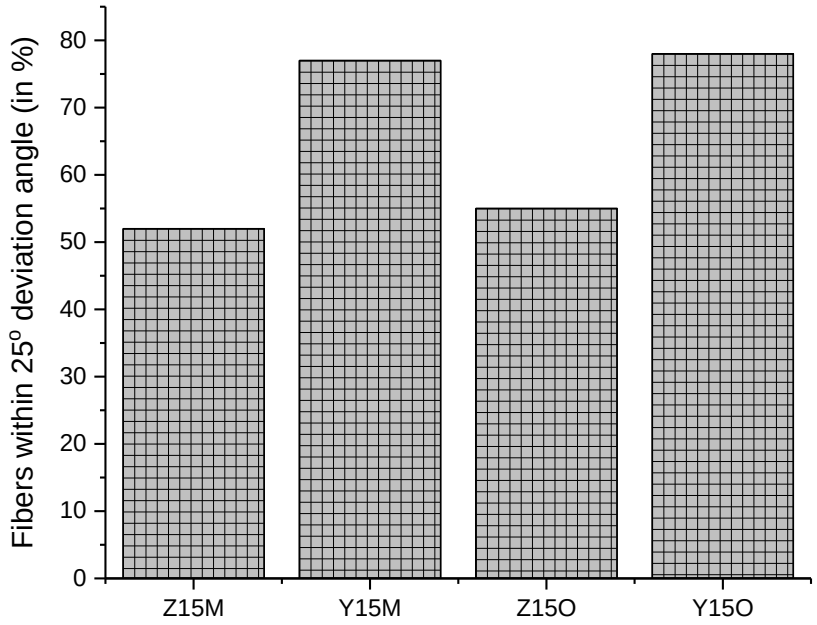

Fig 73. *Comparison of fiber orientation between Z-oriented and Y-oriented specimens with 15% fiber weight fraction.*

3.6 Analysis of Burn Test

The burn test result was obtained by the weight difference between the crucible plus specimen weight before calcination and crucible plus residue weight after calcination. Apart from the weight fraction analysis, fiber length is also analyzed after the burn test.

3.6.1 Fiber Weight Fraction Analysis

The fiber weight fraction analysis is done by burning out the rest of the matrix from the samples. The weight differences then measured and found as the actual fiber weight fraction. The results are presented in *table 15* and the comparison between the specimens is schematically shown in *figure 74*, *figure 75* and *figure 76*.

Table 15. *Fiber weight fraction (%) by burn test.*

Specimen	Fiber Weight Fraction (%)				
	Top	Middle	Bottom	Average	Std. Dev.
Z30M	31.1	35.1	31.4	32.5	2.2
Z30O	31.4	31.0	29.7	30.7	0.9
Z30MHT	30.7	29.2	30.5	30.1	0.8
Z15M	19.9	20.1	19.0	19.7	0.6
Y30M	32.0	30.7	33.7	32.1	1.5
Y15M	21.3	18.7	21.1	20.4	1.4
Y30O	28.0	30.0	29.7	29.2	1.1
Y15O	15.2	15.1	16.2	15.5	0.6

Each and every Z oriented specimens, for example, Z30M, have different fiber weight fraction. At the top part of the box the weight fraction is 31.1%, 35.1% in the middle and 31.4% in the bottom. This could potentially mean the short fibers are not distributed evenly throughout the entire printing process. According to *section 1.2.1* possibly clogging effect may play a role. All the specimens have shown this effect. A similar kind of trend is also observed for the Y oriented specimens.

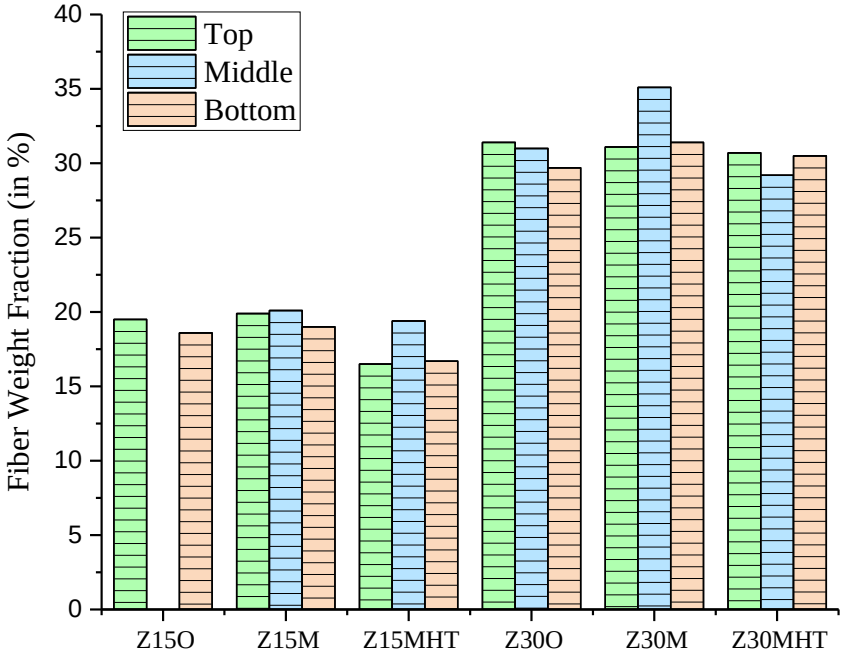

Fig 74. *Comparison of fiber weight fraction of Z-oriented specimens.*

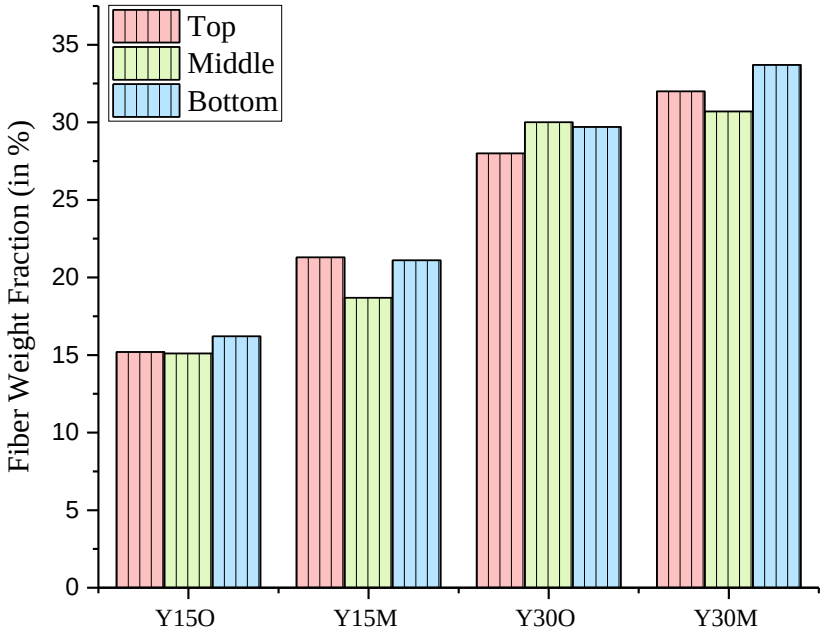

Fig 75. *Comparison of fiber weight fraction of Y-oriented specimens.*

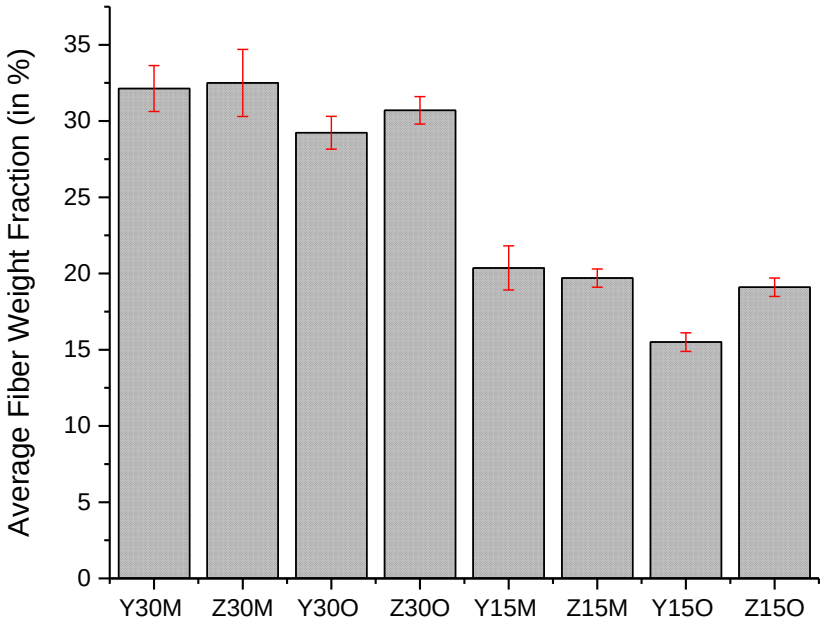

Fig 76. *Comparison of fiber weight fraction of Y-oriented and Z-oriented specimens.*

The average fiber weight fraction comparison, in *figure 76*, shows some interesting trends between the specimens.

The average fiber weight fraction of all the 30% theoretically should be approximately the same but in the analysis it is different. The average weight fraction of Y30M is 32.1%, Y30O is 29.2%, Z30M is 32.5% and Z30O is 30.7%. That means Z30M and Y30M have approximately the same amount of fiber inside. Y30O and Z30O have the lowest amount of glass fiber weight fraction. The optical microscopy analysis from *section 3.1.8* suggests to have the specimens containing O symbol at the end have higher voids than M. Probably there was variation of weight fraction in the filaments even before printing.

The same trend is also found for the 15% fiber weight fraction. All the specimens do not have approximately the same amount of average fiber weight fraction. Another important thing is to notice, in both cases, Y30O and Y15O specimen have the lowest amount of glass fiber. The density analysis of *section 3.2.1* also suggests that between Y30O vs Z30O and Y15O vs Z15O, Z30O and Z15O have lower density. And porosity in *section 3.4* also suggests Z15O and Z30O has higher porosity. It means, these two have more voids inside the material and thus the weight fraction difference with counterparts.

3.6.2 Fiber Length Analysis

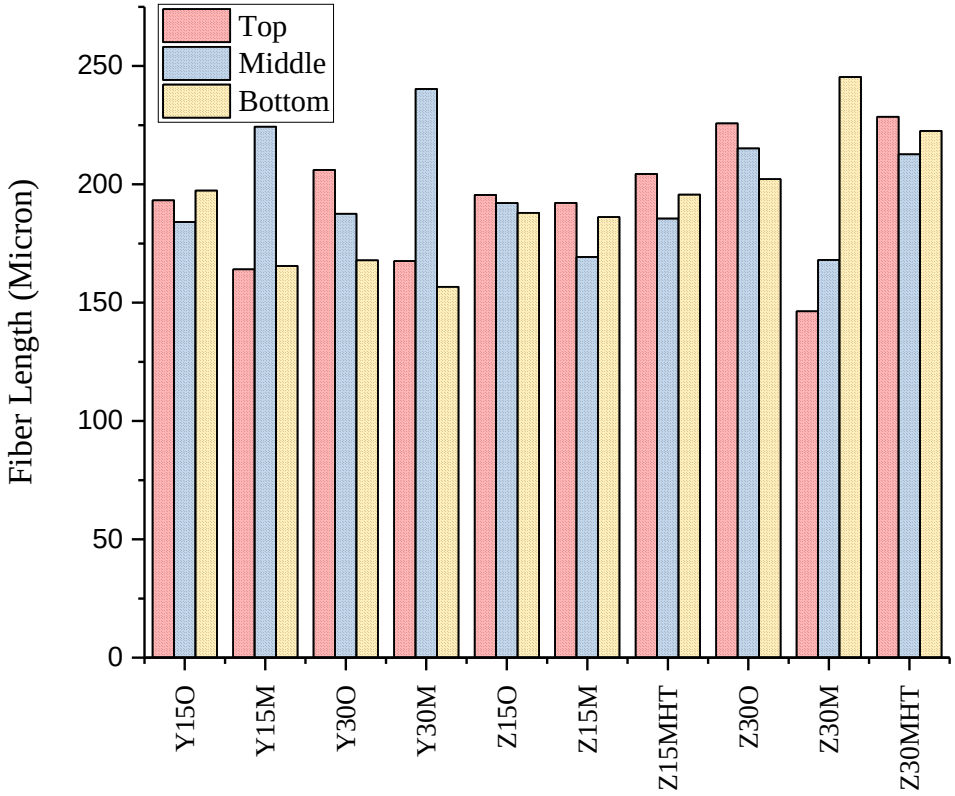

Fig 77. *Comparison of fiber length of Y-oriented and Z-oriented specimens.*

The fiber length analysis from the burn test is presented in *figure 77*. By analysis the graph it is possible to say that there is no common trend for the fiber length and the length is not also constant. The length is changing with respect to the specimens, printing direction. Even the length is not fixed inside the boxes. As for example, Y30M has 167.6 µm at the top side of the box, 240.3 µm in the middle and 156.7 µm at the bottom part of the box.

The comparison of the average fiber length of Y and Z oriented specimens are depicted in *figure 78*. Z30MHT has highest average fiber length and Z15M has the lowest. There is a trend is possible to highlight that Y15M, Y30M, Z30M have higher standard deviation. On the other hand, Y15O, Z15O have smaller standard deviation. This could possibly mean the length variation of top, middle and bottom part of Y15M, Y30M, Z30M is higher than Y15O, Z15O. There may have also connection with the heating strategy to have bigger and smaller variations behind the average fiber length.

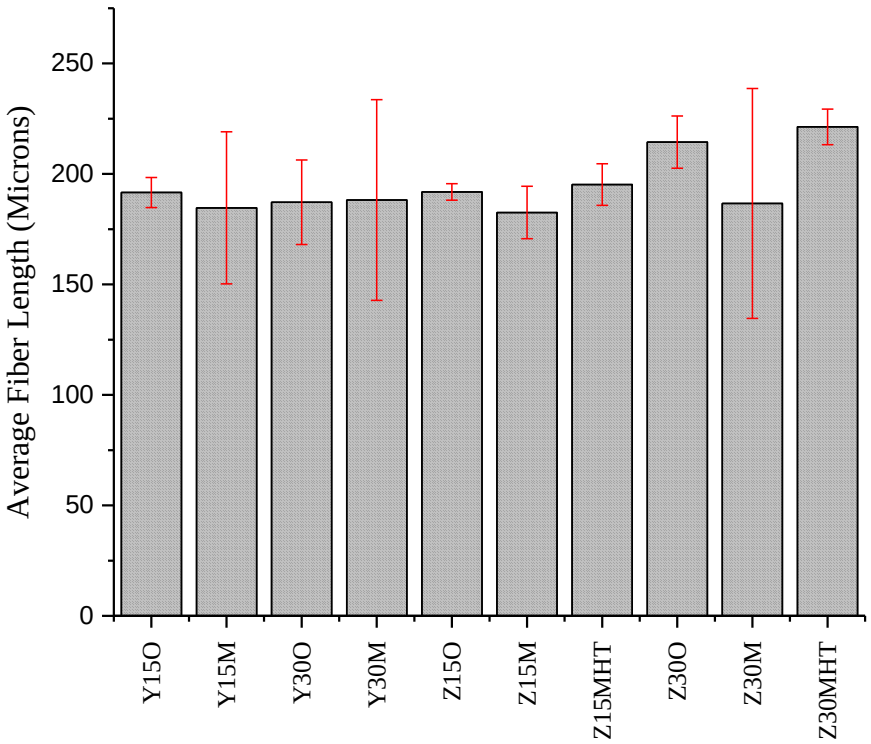

Fig 78. *Comparison of average fiber length of Y-oriented and Z-oriented specimens.*

3.7 Fiber Length vs Tensile Strength

The following *figure 79* to *figure 82* are representing the schematic relation of tensile strength with respect to fiber length. It is known that the tensile strength has a direct relation with the short fiber length, mentioned in *section 1.2.2*.

In comparison between Y30M and Y30O specimens, it is apparent that tensile strength is probably varying with the change of fiber length. To specific, when the fiber length is 45.6µm the tensile strength is 187.6 MPa, 206.1 MPa for 46.1µm and 167.9 MPa for 50.1µm. This could potentially indicate that with the increase of fiber length tensile strength also increased. After the optimal length again the tensile strength declines, and in *figure 74* the possible optimal fiber length is 46.1µm. In *figure 79*, probably the optimal fiber length is 48.6µm because before and after this length tensile strength reduces.

At the same time, Y30M possesses the highest tensile strength, 240.3MPa. The heating strategy and more porous space inside the printing tracks, from *section 3.1.7*, can have influence over the tensile strength's possession.

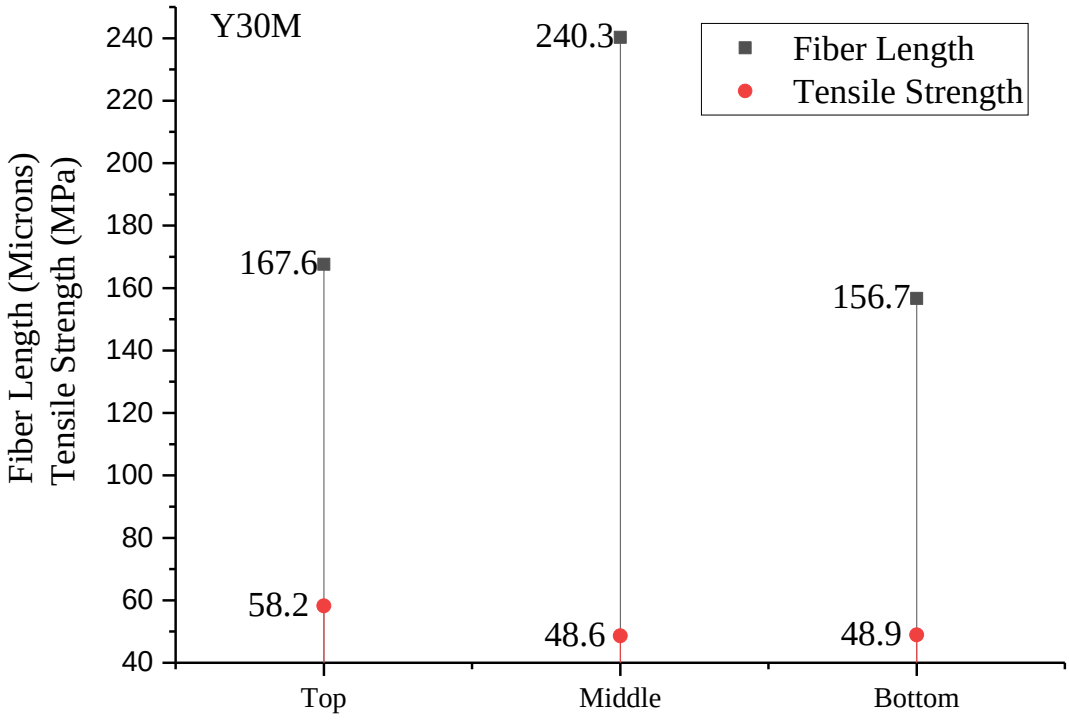

Fig 79. *Comparison of average fiber length vs tensile strength of* Y30M.

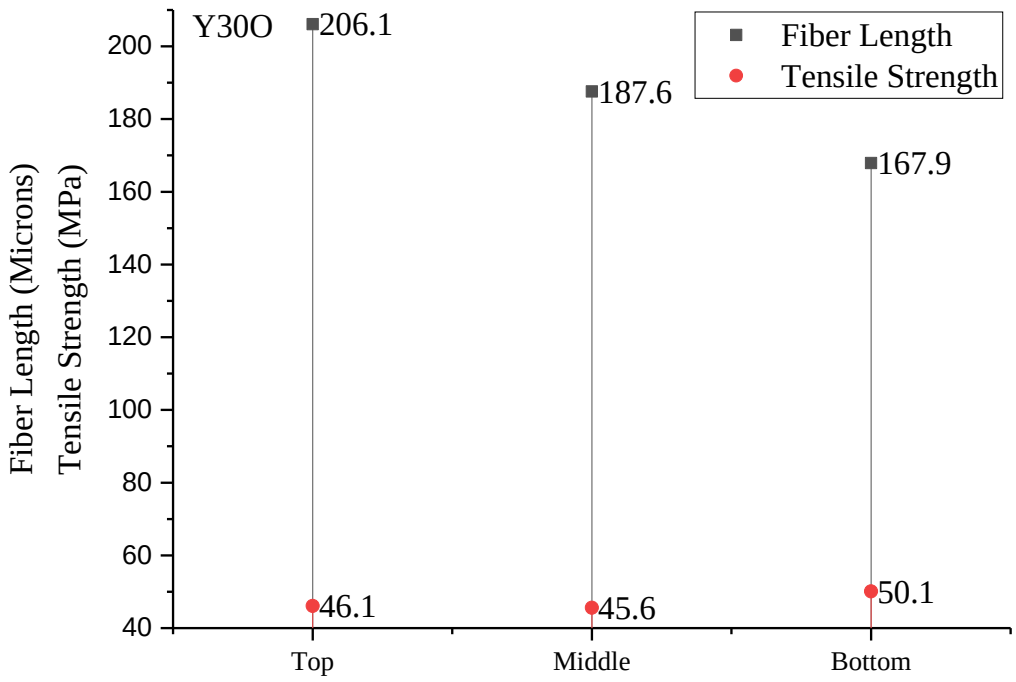

Fig 80. *Comparison of average fiber length vs tensile strength of* Y30O.

In comparison between Y15M and Y15O specimens, the tensile strength increases with the increase of the fiber length and after the optimal length, it reduces. Likewise, in Y15O specimens, the tensile strength is 193.3MPa, 197.4MPa, and 184.1MPa with respect to the fiber length of 45.7µm, 46.3µm, and 47.7µm. The probable optimal fiber length is 46.3µm. In Y15M specimens, the tensile strength is 164.1MPa, 165.5MPa, and 224.4MPa with respect to the fiber length of 47.7µm, 49.4µm, and 50.8µm. But here the optimal fiber length is not distinguishable.

The relation between fiber length and tensile strength is difficult to generalize because some specimens have the probable optimal fiber length and some have no distinguishable optimal fiber length.

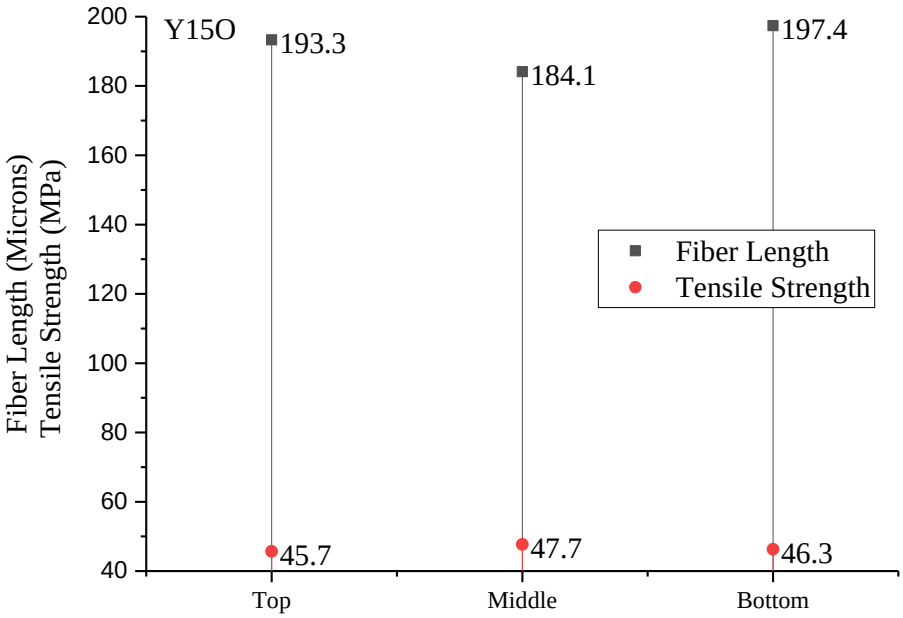

Fig 81. *Comparison of average fiber length vs tensile strength of* Y15O.

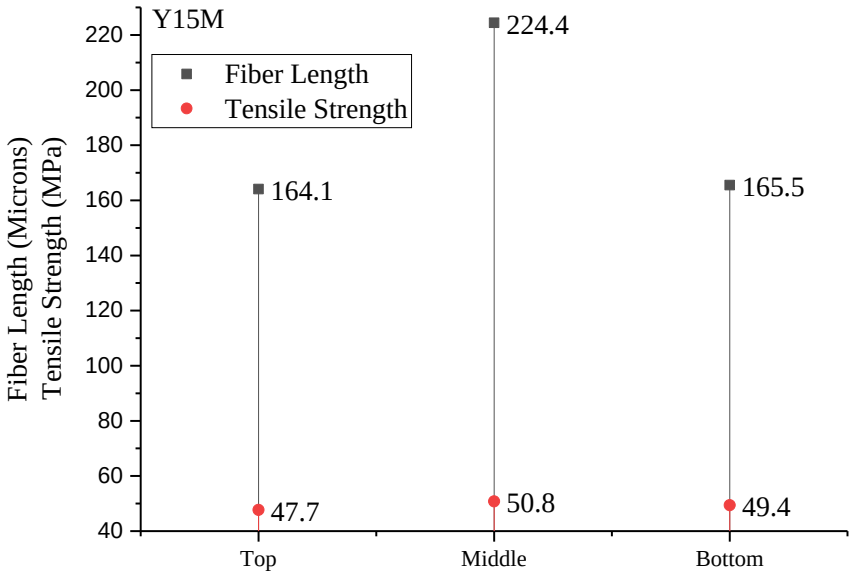

Fig 82. *Comparison of average fiber length vs tensile strength of* Y15M.

3.8 Analysis of Position of Samples

A previous study [35] founds printed samples by fused filament fabrication process have tendency to have higher porosity at the bottom of the printed part and less at the top. Although that study was regarding some specimens directly printed by fused filament fabrication, it was raising question regarding what should be the reasoning for the phenomena.

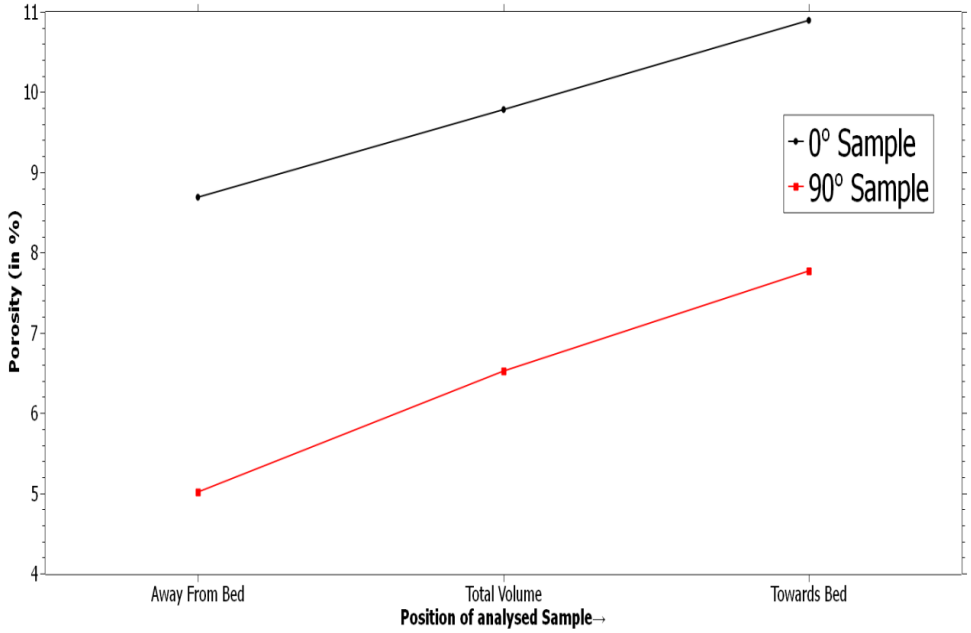

Fig 83. *Comparison of porosity and position of the samples* [35].

To investigate further Y30M was taken as an example printed box and then marked respective to the printing bed distance. In *figure 84*, the nearest specimen to the bed was marked as #1 and the furthest was #3.

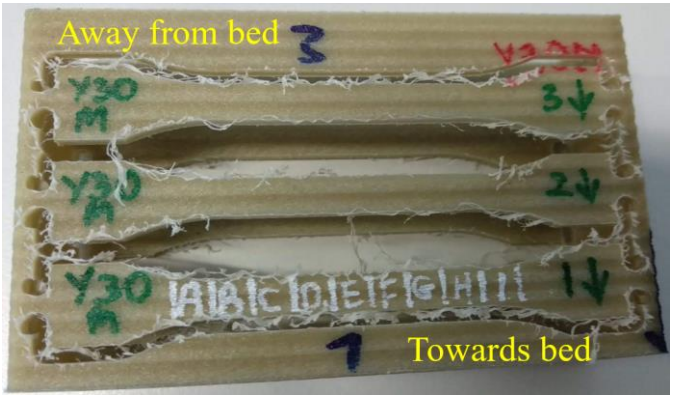

Fig 84. *Milled out printed box* Y30M.

The comparison between porosity, fiber weight fraction, density and tensile strength one of the boxes Y30M is shown in *figure 85*. However, these changes are not so prominent to make concrete decision, the comparison is displayed to show probable correlation.

Porosity analysis indicates it is changing with the distance from the printing bed, although the relation is the opposite. Porosity is high away from the bed and low towards the bed. And fiber weight fraction analysis shows something interesting. Fiber weight fraction is changing with respect to the bed distance, high towards the bed. This means the short fiber is not distributed evenly throughout the entire printing process and it may have connection with the clogging or pressure drop effect mentioned in *section 1.2.1*. At the starting, printer was spreading a certain amount of short fibers inside molten polymer's printing tracks because of a certain pressure force in the material flow inside the nozzle that leads higher fiber weight fraction towards the bed. After that pressure force in the molten material was reduced because of deposition of short fibers inside the nozzle and resulted deposition of less amount of fiber which reflected in the fiber weight fraction analysis.

The density result tells density was higher for the less porous sample, towards the printing bed and should have higher fiber weight fraction. The weight fraction prediction is exactly matched with the comparison. But in this comparison, tensile test result acts opposite to fiber weight fraction. Generally tensile strength should be higher with higher fiber weight fraction, here it is not. This could potentially have connection with the fiber orientation inside the printed samples. Probably the fibers are not properly aligned with the direction of the tensile test.

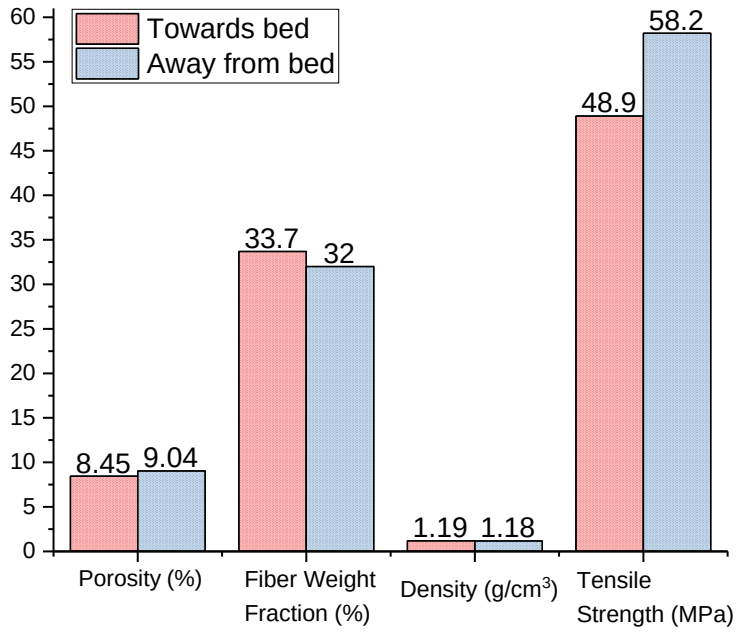

Fig 85. *Comparison of porosity, fiber weight fraction, density and tensile strength of* Y30M.

Conclusions

The aim of this thesis work is to observe and characterize the mechanical performance of fused filament fabrication (FFF) 3D printed samples produced with polyamide 6 and reinforced with short glass fiber. To check the improvement of the mechanical performance with injection moulded parts.

The samples were printed as boxed shapes, to replicate the real-time pressure difference and temperature variation during the printing process. The samples were prepared mainly with two variations: polyamide 6 with 15% weight fraction of glass fiber and polyamide 6 with 30% weight reaction of glass fiber. Two different raster angles: 90^{o}, perpendicular to printing direction to the 0^{o} parallel to the printing direction. Apart from these, nozzle temperature, printing speed and heating methods were varied to observe more possibilities.

To see the microstructure, voids, and air gaps inside the material optical microscopy are used. The Archimedes principle is followed to measure density which helped to check mass per unit volume. The existing porosity and fiber orientation towards the printing direction is measured by the X-ray computed tomography (xCT). The burn test was conducted to measure the fiber length of the short glass fiber presents inside the feeding filament. The most important one is the tensile test, it helped to observe mechanical performance.

The target was to cut six test specimens from the six different positions of the individual boxes. There were only three test specimens possible to cut out from the Z15O box. In the case of box Z15MHT the test specimen number #2 was broken before mounting in the tensile testing machine and slippage during the testing occurred for test specimen #5 and #6. At the same time, in box Z30MHT the test specimen #6 was broken before tensile testing and slippage occurred for the test specimen #1 and #4. Because of this reason these test specimens were excluded from the detailed analysis of tensile testing results.

The fiber length inside the glass fiber filament was not uniform in length, it varied. Which may have an impact on the variation of the mechanical performance of the specimens coming from the same printed box. At the same time, the tensile strength varied according to the glass fiber's length and it increased until the optimum level and decreased again. The fiber length only from three different positions was measured, which is not enough to draw a clear hypothesis with the tensile strength.

To compare printed parts mechanical performance and injection moulded parts mechanical performance, the pure polyamide 6 tensile strength, polyamide 6 with 15% and 30% weight fraction of glass fiber tensile strength are taken from the literature.

The following observations have been found from the 3D printed test samples which were produced in Brightlands, Netherlands and tested in Fraunhofer IMWS, Germany:

1. Heating strategy plays a role in forming bonds between the layers. Better the heating better the bond formation. The printing speed is important to form layer bonding during printing. Lower printing speed causes poor bonding between the layers of the printed parts because it takes a longer time to travel a cycle.
2. Tensile strength is higher towards 0^o raster orientation, poor towards 90^o. Printing speed, heating temperature, and strategy, fiber weight fraction have a significant impact on the tensile strength.
3. Elastic modulus is higher towards 0^o raster orientation and lowers towards 90^o. It is also influenced by the heating strategy and fiber weight fraction.
4. Strain (or elongation) at break is higher towards 0^o raster orientation and lower towards 90^o. It is also influenced by the density and fiber weight fraction.
5. The tensile strength difference between injection modulded parts and printed materials with 15% & 30% fiber weight fraction is respectively approx. 11% and approx. 15%. The heating system played a role for printed materials.
6. At 15% fiber weight fraction, elastic modulus is nearly same. At 30% weight fraction printed material shows less elastic modulus than injection moulded parts.
7. Porosity is comparatively higher towards 90^o raster orientation and lowers towards 0^o. With the increase of fiber weight fraction, porosity follows the opposite relation between 0^o and 90^o raster orientations.
8. Fiber orientation is comparatively higher towards 0^o raster orientation and lowers towards 90^o. With the increase of fiber weight fraction, it follows the opposite relation between 0^o and 90^o raster orientations.

References

[1] J. Carey, "2017," in *Handbook of Advances in Braided Composite Materials*, Woodhead Publishing.

[2] D. Callister, Materials Science and Engineering- An Introduction, USA: John Wiley & Sons Inc, 2007.

[3] "Romeorim," [Online]. Available: https://romeorim.com/what-are-composites/. [Accessed 11 09 2019].

[4] G. Goh, "Characterization of mechanical properties and fracture mode of additively manufactured carbon fiber and glass fiber reinforced thermoplastics," *Materials and Design,* vol. 137, pp. 79-89, 2018.

[5] R. Matsuzuki, "Three dimensional printing of continuous fiber composites by in-nzzle impregnation," *Nature,* vol. Sci. Rep 6, p. 23058, 2016.

[6] L. Blok, "An investigation into 3D printing of fibre reinforced thermoplastic composites," *Additive Manufacturing,* vol. 22, pp. 176-186, 2018.

[7] Agarwala, "Structural quality of parts processed by fused deposition," *Emerald,* vol. 2, pp. 4-19, 1996.

[8] Gibson, Additive Manufacturing Technologies: Rapid Protyping to Direct Digital Manufacturing, New York, NY: Springer, 2010.

[9] B. N. Turner, "A reivew of melt extrusion additive manufacturing process: I. process design and modeling," *Emerald,* vol. 20, no. 3, pp. 192-204, 2014.

[10] Yardimci, "Thermal analysis of fused deposition," in *Solid Freeform Fabrication Proceedings*, University of Texas at Austin, Austin, TX, 1997.

[11] Ramanath, "Melt flow behavior of poly-epsilon-caprolactone in fused deposition modeling," *Journal of Materials Science-Materials in Medicine,* vol. 19, pp. 2541-2550, 2008.

[12] A. Bellini, "Liquifier dynamics in fused deposition," *Journal of Manufacturing Science and Engineering,* vol. 126, no. 2, pp. 237-246, 2004.

[13] W. Michaeli, "Extrusion dies for plastics and rubber: design and engineering computations," in *Hanser Verlag*, Munchen, 2003.

[14] Resenzweig, "Sintering rheology of amorphous polymers," *Polymer Engineering and Science,* vol. 21, pp. 1167-1170, 1981.

[15] C. Bellehumeur, "Modeling of bond formation between polymer filaments in the fused deposition modeling process," *Journal of Manufacturing Processes,* vol. 6, no. 2, 2004.

[16] L. Behalek, "Fused deposition modeling vs injection moulding- influence of fiber orientation and layer thickness on the mechanical properties," *MM Science,* 2018.

[17] C. Capela, "Effect of fiber length on the mechanical properties of high doge carbon reinforced," in *Structural Integrity Procedia*, Maderia, Portugal, 2017.

[18] F. Ning, "Additive manufacturing of carbon fiber reinforced thermoplastic composites using fused deposition modeling," *Composites Part B,* vol. 80, pp. 369-378, 2015.

[19] Y. Leng, Materials Characterization- Introduction to Microscopic and Spectroscopic Methods, Edition 2, John Wiley & Sons, 2013.

[20] R. Schmitt, "Fusion of micro-metrology techniques for the flexible inspection of MEMS assembly," in *The Internation Society for Optical Engineering*, 2008.

[21] Y. Nikishkov, "Measurement of voids in composites by x-ray computer tomography," *Composites Science and Technology,* pp. 89-97, 2013.

[22] J. Kruth, "Computed tomography for dimensional metrology," *CIRP Ann. Manufacturing Technology,* vol. 60, pp. 821-842, 2011.

[23] D. Chiffre, "Industrial applications of computed tomography," *CIRP Ann. Manufacturing Technology,* vol. 63, pp. 655-677, 2014.

[24] J. Hsieh, Computed tomography: principles, design, artifacts, and recent advances, Bellingham, WA, USA: SPIE Press, 2009.

[25] "Mettler Toledo," [Online]. Available: https://www.mt.com/ch/en/home/applications/Laboratory_weighing/density-measurement.html. [Accessed 15 08 2019].

[26] A. Spierings, "Comparison of density measurement techniques for additive manufactured metalic parts," *Rapid Prototyping,* vol. 17, no. 5, pp. 380-386, 2011.

[27] ISO, "Test conditions for moulding and extrusion plastics (ISO 527-2:2012)". 2012.

[28] ISO, "Accelerated conditioning of test specimens (ISO 1110 : 1995)". 1995.

[29] "Federation of European Producers of Abrasives (FEPA)," [Online]. Available: https://www.fepa-abrasives.com/. [Accessed 10 07 2019].

[30] "R. T, GmbH," Operating instructions- Rayscan 200E, 2014. [Online]. Available: http://www.rayscan.eu/Downloads.html. [Accessed 31 10 2019].

[31] ISO, "Plastics- Methods for determinig the density of non-cellular plastics (ISO 1183-1)". 2019.

[32] ISO, "Textile-glass-reinforced plastics-Prepregs, moulding compunds and laminates-Determination of the textile-glass and mineral filler content-Calcination methods". 1992.

[33] D. Nuruzzaman, "Experimental investigation on the mechanical properties of glass fiber reinforced nylon," in *IOP Conf. Series: Materials Science and Engineering*, 2016.

[34] C. Annandarajah, "Hybrid Cellulose-Glass Fiber Composites for Automotive Applications," *Materials*, vol. 12, p. 3189, 2019.

[35] N. Pattanshetty, "Analysis of micrstructure of 3D printed fiber reinforced composites using X-ray computed technology," 2019.

[36] J. Varna, "Effect of voids on failure mechanism in RTM laminates," *Composite Science and Technology*, vol. 53, pp. 241-249, 1995.

[37] W. MR, "Reduction in interlaminar shear strength by discrete and distributed voids," *Composites Science and Technology*, vol. 56, no. 1, pp. 93-101, 1996.